Numerical and Experimental Investigation of a Sharp-Crested Weir Nappe

Zur Erlangung des akademischen Grades eines

DOKTORS DER INGENIEURWISSENSCHAFTEN (Dr.-Ing.)

von der KIT-Fakultät für
Bauingenieur-, Geo- und Umweltwissenschaften
des Karlsruher Instituts für Technologie (KIT)

genehmigte

DISSERTATION

von

Markus Wagner
geb. in Kassel

Tag der mündlichen Prüfung:	28.07.2023
Hauptreferent:	Prof. Dr. Olivier Eiff
Korreferent:	Prof. Dr. Daniel B. Bung

Acknowledgements

This thesis was created during my work as a research assistant at the Institute for Hydromechanics (IfH) of the Karlsruhe Institute of Technology in close co-operation with the Federal Waterways and Research Institute of Germany (BAW). During that time, numerous people supported me and contributed to the success of this work.

First of all, I wish to express my deepest gratitude to Prof. Dr. Olivier Eiff, joint head of IfH and head of the experimental fluid mechanics group at the Karlsruhe Institute of Technology, for supervising this project, for his enormous interest and support. Thank you for creating an environment in which I could grow along with my project.

I am grateful to Prof. Dr. Daniel B. Bung from FH Aachen University of Applied Sciences for taking on the second reviewer role for this thesis, for his interest in my work and for the exchange on void fraction measurement systems.

I extend my thanks to Dr.-Ing. Carsten Thorenz, head of section hydraulics at structures at the BAW, for all the technical discussions we had and for his support during the project.

Many thanks to my office colleagues at BAW for all the support and the great time with a special thanks to Dr.-Ing. Lydia Schulze. Without you, the beginning of this work would have been much more difficult and the end less entertaining.

I would like to thank Yvan Bercovitz from Électricité de France (EDF) for the cooperation on the experimental investigations at the EDF-laboratory at Chatou.

Finally, I take this opportunity to express my gratitude to my family and friends who have accompanied and supported me all the way.

Abstract

This thesis investigates the influence of upstream induced turbulence on the development of a sharp-crested weir nappe by applying 3D numerical and experimental investigations. The numerical investigations were based on the Volume-of-Fluid method with Large Eddy Simulations (LES) and unsteady Reynolds-averaged Navier Stokes (URANS) models. Nappes of 1 m width and a drop depth of 6 m were modeled with volume flow rates of 0.16 $m^3/s \leq Q \leq$ 0.64 m^3/s and turbulence intensities ranging 7.5 % $\leq I \leq$ 19.7 % measured 1 m upstream of the weir. The results reveal that turbulence intensity and in particular the large-scale turbulent structures drive the deformation of the nappe surface. Furthermore, the deformation increases with increasing turbulence intensity, resulting in lateral nappe widening. For higher volume flow rates, lateral nappe widening starts at deeper drop depths, but increases in effect. As a result, lateral nappe widening becomes more and more independent from volume flow rate concerning the initial lateral nappe width with increasing drop depth. The comparison of LES and URANS simulations shows that the nappe surface deformation due to upstream turbulence is highly underestimated by URANS models.

The experimental investigations were carried out on a nappe of 1 m width and a drop depth of 9.5 m with a volume flow rate of 0.1515 m^3/s. The nappe development was measured with conductivity probes at three drop depths Z_d = 0.8 m, 3.3 m and 7 m. The resulting nappe profiles show that the nappe narrows from Z_d = 0.8 m to Z_d = 3.3 m and widens again at a drop depth of Z_d = 7 m. A long-term (10 h) void fraction measurement in combination with a volume flow rate measurement was performed and shows that small fluctuations in the volume flow rate have noticeable effects on the void fraction at the water-air interface. Further investigations explain these void fraction variations with the change in nappe trajectory which accompanies volume flow rate fluctuations.

The comparison of the nappe development of the numerical and the experimental investigations shows a similar trend for drop depths up to 3.3 m. This is also supported by visual comparison of the derived nappe surfaces from numerical investigations with photos taken from the experimental nappe. For deeper drop depths, the experimental lateral nappe widening is significantly stronger compared

to the numerical lateral nappe widening. This suggests that the continuous narrowing of the nappe core in combination with high velocities increases the influence of aerodynamic effects at the water air interface, which are not captured by the numerical model.

Zusammenfassung

Die hydraulische Situation des Fischabstiegs an überströmten Wehren ist mit der Entwicklung des Überfallstrahls während des freien Falls verbunden. Das Ziel dieser Arbeit ist es den Einfluss von oberstromseitig eingetragener Turbulenz auf die Entwicklung des Überfallstrahls eines scharfkantigen Wehres zu untersuchen. Numerische und experimentelle Untersuchungen für unterschiedliche turbulente Intensitäten und Volumenströme wurden durchgeführt. Die numerischen Untersuchungen basieren auf der Volume-of-Fluid Methode mit Large Eddy Simulations (LES) und unsteady Reynolds-averaged Navier Stokes (URANS) Modellen. Überfallstrahlen mit 1 m Breite und einer Falltiefe von 6 m werden für Volumenströme von 0,16 $m^3/s \leq Q \leq$ 0,64 m^3/s und turbulente Intensitäten im Bereich 7,5 % $\leq I \leq$ 19,7 % 1 m oberstrom des Wehres gemessen modelliert. Die Ergebnisse zeigen, dass turbulente Intensität und insbesondere die großskaligen turbulenten Strukturen die Deformation der Strahloberfläche vorantreiben. Außerdem vergrößert sich die Deformation mit steigender turbulenter Intensität, was in der Aufweitung des Überfallstrahls resultiert. Für größere Volumenströme startet die Strahlaufweitung bei tieferen Falltiefen, nimmt jedoch an Wirkung zu. Dadurch wird die Aufweitung des Überfallstrahls bezüglich der anfänglichen Dicke des Überfallstrahls mit zunehmender Falltiefe immer unabhängiger vom Volumenstrom. Der Vergleich von LES und URANS Simulationen zeigt, dass die Deformation der Oberfläche des Überfallstrahls aufgrund oberstromseitiger Turbulenz stark von URANS Modellen unterschätzt wird.

Die experimentellen Untersuchungen wurden an einem Überfallstrahl mit einer Breite von 1 m und einer Falltiefe von 9,5 m mit einem Volumenstrom von Q = 0,1515 m^3/s durchgeführt. Die Entwicklung des Überfallstrahls wird auf drei Falltiefen Z_d = 0,8 m, 3,3 m und 7 m mit Leitfähigkeitssonden gemessen. Die daraus resultierenden Überfallstrahlprofile zeigen, dass sich der Überfallstrahl von Z_d = 0,8 m nach Z_d = 3,3 m einengt und auf einer Falltiefe von Z_d = 7 m wieder aufweitet. Eine Langzeitmessung (10 h) des Hohlraumanteils in Kombination mit einer Volumenstrommessung wurde durchgeführt und zeigt, dass kleine Fluktuationen im Volumenstrom bemerkbare Auswirkungen auf den Hohlraumanteil an der Wasser-Luft Grenzschicht haben. Weitere Un-

tersuchungen erklären die Schwankungen des Hohlraumanteils mit der Veränderung der Trajektorie des Überfallstrahls, welche mit Schwankungen des Volumenstroms einhergeht. Der Vergleich der Entwicklung des Überfallstrahls der numerischen und der experimentellen Untersuchungen zeigt einen ähnlichen Trend für Falltiefen bis 3,3 m. Dies wird auch durch einen visuellen Vergleich der aus den numerischen Modellen abgeleiteten Überfallstrahloberflächen mit Fotos des experimentell untersuchten Überfallstrahls unterstützt. Für tiefere Falltiefen ist die Aufweitung des experimentellen Überfallstrahls deutlich größer im Vergleich zu der Aufweitung des numerischen Überfallstrahls. Dies lässt vermuten, dass die kontinuierliche Einengung des Kernbereichs des Überfallstrahls in Kombination mit hohen Geschwindigkeiten den Einfluss aerodynamischer Effekte an der Wasser-Luft Grenzschicht vergrößert, welche nicht von dem numerischen Modell abgebildet werden.

Eidesstattliche Versicherung

Eidesstattliche Versicherung gemäß § 13 Absatz 2 Satz 1 Ziffer 4 der Promotionsordnung des Karlsruher Instituts für Technologie (KIT) für die KIT-Fakultät für Bauingenieur-, Geo- und Umweltwissenschaften

1. Bei der eingereichten Dissertation zu dem Thema
Numerical and Experimental investigation of a Sharp-Crested Weir Nappe
handelt es sich um meine eigenständig erbrachte Leistung.
2. Ich habe nur die angegebenen Quellen und Hilfsmittel benutzt und mich keiner unzulässigen Hilfe Dritter bedient. Insbesondere habe ich wörtlich oder sinngemäß aus anderen Werken übernommene Inhalte als solche kenntlich gemacht.
3. Die Arbeit oder Teile davon habe ich bislang nicht an einer Hochschule des In- oder Auslands als Bestandteil einer Prüfungs- oder Qualifikationsleistung vorgelegt.
4. Die Richtigkeit der vorstehenden Erklärungen bestätige ich.
5. Die Bedeutung der eidesstattlichen Versicherung und die strafrechtlichen Folgen einer unrichtigen oder unvollständigen eidesstattlichen Versicherung sind mir bekannt.

Ich versichere an Eides statt, dass ich nach bestem Wissen die reine Wahrheit erklärt und nichts verschwiegen habe.

Ort und Datum Unterschrift

Eidesstattliche Versicherung

Belehrung

Die Universitäten in Baden-Württemberg verlangen eine Eidesstattliche Versicherung über die Eigenständigkeit der erbrachten wissenschaftlichen Leistungen, um sich glaubhaft zu versichern, dass der/die Promovend/-in die wissenschaftlichen Leistungen eigenständig erbracht hat.
Weil der Gesetzgeber der Eidesstattlichen Versicherung eine besondere Bedeutung beimisst und sie erhebliche Folgen haben kann, hat der Gesetzgeber die Abgabe einer falschen eidesstattlichen Versicherung unter Strafe gestellt. Bei vorsätzlicher (also wissentlicher) Abgabe einer falschen Erklärung droht eine Freiheitsstrafe bis zu drei Jahren oder eine Geldstrafe.
Eine fahrlässige Abgabe (also Abgabe, obwohl Sie hätten erkennen müssen, dass die Erklärung nicht den Tatsachen entspricht) kann eine Freiheitsstrafe bis zu einem Jahr oder eine Geldstrafe nach sich ziehen.
Die entsprechenden Strafvorschriften sind in § 156 StGB (falsche Versicherung an Eides Statt) und in § 161 StGB (fahrlässiger Falscheid, fahrlässige falsche Versicherung an Eides Statt) wiedergegeben.
§ 156 StGB: Falsche Versicherung an Eides Statt Wer vor einer zur Abnahme einer Versicherung an Eides Statt zuständigen Behörde eine solche Versicherung falsch abgibt oder unter Berufung auf eine solche Versicherung falsch aussagt, wird mit Freiheitsstrafe bis zu drei Jahren oder mit Geldstrafe bestraft.
§ 161 StGB: Fahrlässiger Falscheid, fahrlässige falsche Versicherung an Eides Statt
Abs. 1: Wenn eine der in den § 154 bis 156 bezeichneten Handlungen aus Fahrlässigkeit begangen worden ist, so tritt Freiheitsstrafe bis zu einem Jahr oder Geldstrafe ein.
Abs. 2: Straflosigkeit tritt ein, wenn der Täter die falsche Angabe rechtzeitig berichtigt. Die Vorschriften des § 158 Abs. 2 und 3 gelten entsprechend.

Ort und Datum Unterschrift

Contents

Nomenclature

α	Volume fraction
α_1	Model constant of turbulent specific dissipation transport equation
β^*	Model constant of turbulent kinetic energy transport equation
β_2	Model constant of turbulent specific dissipation transport equation
δ	Boundary layer height
δ^*	Boundary layer displacement
κ	Curvature of the interface
μ	Viscosity
μ_t	Eddy viscosity
ν_t	Kinematic eddy viscosity
ω	Turbulent specific dissipation rate
ϕ_g	Property of the air phase
ϕ_l	Property of the water phase
ϕ_m	Property of the air-water mixture
ρ	Density
σ	Standard deviation of the water distribution

σ_{k}	Model constant of turbulent kinetic energy transport equation
$\sigma_{\omega 2}$	Model constant of turbulent specific dissipation transport equation
σ_{ω}	Model constant of turbulent specific dissipation transport equation
σ_{st}	Surface tension
τ	Viscous stress tensor
τ^{T}	Reynolds stress tensor
c_{α}	Face-flux compression coefficient
$\mathrm{c}_{\mathrm{i}\alpha}$	Isotropic compression contribution
A_i	Cut surface area of cell
C	Void fraction
D_{t}	Turbulent mass diffusion
F_1	Blending function of turbulent specific dissipation transport equation
g	Gravitational vector
H	Headwater level
h_{BC}	Inlet patch height
I	Turbulence intensity
I_{d}	Directly captured turbulence intensity
k_{s}	Subgrid turbulent kinetic energy
l_i	Segment length of interpolated void fraction measurement
L_{i}	Integral length scale
P_k	Production term of turbulent kinetic energy
p_{rgh}	Dynamic pressure

Re	Reynolds number
S	Invariant measure of the strain rate
Sc_t	Turbulent Schmidt number
T	Period length
t	Time
T_i	Integral time scale
U	Velocity vector
U_max	Maximal velocity
U_r	Artificial compression velocity
U_sf	Velocity in surface normal direction
u_z	Vertical velocity
V_g	Voltage level of conductivity probe in air
V_l	Voltage level of conductivity probe in water
V_t	Threshold voltage
We	Weber number
x	Position vector
x_w	Horizontal distance to weir
x_i	x-coordinate of cell center
x_CG	x-coordinate of center of gravity
Z_d	Drop depth
ADV	Acoustic Doppler velocimeter
Amp	Amplitude of inlet boundary condition

BAW The Federal Waterways Engineering and Research Institute

BC Boundary condition

CEL_f Far interface cell-edge length

CEL_n Near interface cell-edge length

CEL_u Upstream cell-edge length

CSF Continuum surface force

EDF Électricité de France

FFT Fast Fourier transform

GDH Gradient-diffusion hypothesis

LES Large Eddy Simulation

SNR Signal-to-noise ratio

TM Turbulence model

URANS Unsteady Reynolds-averaged Navier Stokes equations

VOF Volume-of-Fluid method

WFD Water Framework Directive

WSV The Federal Waterways and Shipping Administration

Chapter 1

Introduction

The regulation of river water levels is facilitated by weir structures, which span across the width of the river, effectively impeding its flow. These structures often pose critical barriers for fish migrating between different sections of water bodies. The Water Framework Directive (WFD) (Directive 2000/60/EC of the European Parliament and of the Council of 23 October 2000) prescribes that surface waters throughout Europe have to achieve good ecological quality till 2027. By implementing the aims of the WFD in the German Water Ressources Act (Wasserhaushaltsgesetz), The Federal Waterways and Shipping Administration (WSV) takes on the task to restore the ecological continuity of surface water bodies. It is therefore necessary to be able to assess hydraulic structures in terms of ecological continuity. The urgency of having such an evaluation possibility becomes particularly clear against the background that several weirs will have to be replaced in the near future. For the evaluation it is important to differentiate between undershot and overflown weirs, since they entail different risks for migrating fish, whereas the hydraulic situation of overflown weirs is discussed in more detail in this work.

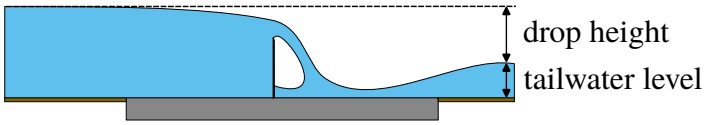

Fig. 1.1. Sketch of the hydraulic situation around a sharp-crested weir.

Fig. 1.1 shows the flow situation of a sharp-crested weir which is of particular importance in this thesis, since current considerations are moving towards re-

placing movable weirs at second-grade rivers with fixed weirs in order to reduce maintenance costs (Belzner et al., 2017). At present, the evaluation of ecological continuity along rivers, which encompasses the migration of fish and other organisms, relies on factors such as the drop height of the free-falling water flow (known as the nappe) and the level of tailwater (DWA, 2005; LUBW, 2016). However, as shown by Thorenz et al. (2018), these two values are not sufficient to evaluate the hydraulic flow situation at the immersion point of the nappe which is particular important for predicting the injury risk posed to descending fish. A shooting discharge condition at the impact point of the nappe will result in a different water level then further downstream. For the actual hydraulic engineering application of a weir, the hydraulic situation is even more complex, since these kind of nappes tend to entrain air into the tailwater, which often in addition contains energy dissipating structures.

Hager (1995) offers a thorough overview of studies on nappe flows at sharp-crested weirs, encompassing their modeling and practical applications. The summary covers previous studies that examined plunge nappe geometry, proposed air vent elements for nappe aeration, investigated optimal spillway crown shapes, and examined nappe boundaries in test channels. Furthermore, extensive research was undertaken on rectangular weirs, particularly in relation to the construction of the Hoover Dam, focusing on factors such as inflow velocity, weir inclination, and overhangs. Another pivotal contribution to understanding nappe flows comes from the research conducted by the Hydraulic Institute of the University of Padua, Italy. Their studies illuminated the complex interaction of forces and the effects of surface tension and viscosity on nappe flows, underscoring their significance, particularly in the context of flow over curved weirs. However, one aspect that was entirely overlooked is the influence of turbulence on the lateral spreading of nappe flows, a phenomenon well-documented for free jets (e.g. Ervine and Falvey, 1987).

A nappe close to prototype scale of a sharp-crested weir with a drop depth of 9.5 m can be seen in Fig. 1.2. For the design process of such nappes, the tailwater side is in the main focus concerning scour, oxygen saturation and air entrainment. However, that the conditioning of the tailwater side is most likely determined by the impact situation of the nappe, is often largely simplified or even neglected.

Fig. 1.2. Model setup of a sharp-crested weir at the laboratory of Électricité de France at Chatou. Specific folume flow rate ~ 0.2 m^2/s. Threadlike deformations in the central area of the nappe surface can be observed. Image taken by Carsten Thorenz (2019) with an exposure time of 2 ms, showing about 7.5 m of the fall. More details on the setup in Bercovitz et al. (2018).

Due to gravitational acceleration, the nappe narrows with drop depth (Z_d), but nappes of prototype scale (like the nappe of Fig. 1.2) tend to widen with Z_d.This behavior is also evident in the nappe shown here. The central region of the nappe, characterized by its darker appearance, displays strand-like structures that extend from the weir crest to the maximum falling depth, seemingly increasing in size. Observations on-site have revealed that these structures vary in their position and size over time. Recent studies, e.g. by Carrillo et al. (2021) who examine the scour behavior of nappes, take into account the expansion of the nappe due to turbulent intensity, following the approach found by Ervine and Falvey (1987). However, this assumption hinges on the notion that turbulence generation in nappes is comparable to free jets which is primarily driven by the nozzle geometry. Since nappes do not originate from a nozzle, the primary source of turbulence in the upstream portion of the nappe is in this thesis suspected to be different.

In this work, the hypothesis is to be tested that upstream induced turbulence is one cause of the observed widening of nappes. This contradicts the state of knowledge on the influence of upstream turbulence on nappes which was gained by unsteady Reynolds-averaged Navier Stokes (URANS) simulations. These previous investigations state that a difference in upstream turbulence intensity has no significant influence on the nappe characteristic (Castillo et al., 2014; Muralha et al., 2020).

Since there are only few investigations on the influence of upstream turbulence on nappes, the literature review of this work also considers the effect of turbulence on hydraulic flow situations that are similar to nappes of sharp-crested weirs. The focus is on the entrainment of air from chute aerator nappes and free-fall water jets. In addition, research areas which are strongly influenced by the nappe impact situation are examined. This includes investigations concerning the formation of scour, oxygen saturation of weirs and air entrainment of drop shafts.

The influence of upstream induced turbulence on nappes is explored in this study, employing both numerical and experimental approaches at prototype scale. In the numerical investigations, the complex dynamics are simulated using a two-phase flow model within the OpenFOAM® v2012 environment. This involves employing a Volume-of-Fluid based solver, incorporating both Large Eddy Simulations (LES) and URANS turbulence models to capture the turbulent flow behavior. Additionally, an experimental model setup is employed to compare the numerical

findings with. This research aims to enhance our knowledge about the hydraulic flow situation of nappes at weirs. By understanding the influence of upstream turbulence on the development of nappes during the free fall, it can be determined whether consideration of upstream turbulence is necessary in predicting nappe flow conditions at weirs.

Chapter 2

Overflow of Weirs and Free-Fall Water Jets

2.1 Fish Downstream Migration at Weirs

The nappe of overflown weirs represents a downstream migration possibility for fish when the spill height is at least twice the fish height (DWA, 2005). As long as fish are fully submerged into the nappe, their velocity is limited to the surrounding water body. However, nappe and fish do not necessarily share the same trajectory, even though densities are comparable. The maximum velocity of fish falling outside the nappe depends on fish length with higher velocities for longer fish. Fish with lengths of 10 cm to 13 cm have a terminal velocity of 12 m/s, whereas fish with 60 cm length reach a terminal velocity of 58 m/s (Bell and DeLacy, 1972). For impact velocities higher than 15 m/s, injuries at gills, eyes and internal organs can be assumed, independent from fish species and fish sizes. However, even fish with a length of 60 cm only reach this velocity after a drop depth of 13 m (Bell and DeLacy, 1972). Therefore, this risk of injury is not in the scope of this work, which deals with weir drop depths of less than 10 m ($v \leq 13$ m/s).

The situation is different with regard to collisions of fish with parts of the weir structure. Albeit investigations show that all fish are killed when hitting structural components after a 56 m deep free-fall (investigated by Richard T. Smith in 1938) (Bell and DeLacy, 1972), it is not possible to generalize the mortality of different

fish species at lower drop depths. In order to ensure that there are no harmful collisions with the river bed, the weir passage (in Germany) is evaluated based on the fall height and the tailwater level (DWA, 2005; LUBW, 2016). These guidelines origin from bypass investigations of Odeh and Orvis (1998). However, as shown by Thorenz et al. (2018), these two values are not enough for evaluating the flow situation at overflow weirs.
Further downstream, turbulence intensity increases the risk of fish being killed by predators (Odeh et al., 2002), showing the importance of knowing the tailwater flow situation.

2.2 Water-Air Interaction at Hydraulic Structures

Hydraulic structures can create strong interactions between the flowing water and the surrounding air. The effect of the interaction can vary in strength and ranges from a roughening of the water surface to the entrainment of air into the flow resulting in water-air mixtures. Due to the appearance of such water-air mixtures, the term 'white water' is often used in this context (e.g. Chanson, 2009). Water and air form two phases which in many areas lead to the formation of water droplets and air bubbles. The sharp transition between water and air is called the water-air interface at which friction leads to an exchange of momentum between the phases. Concerning the hydraulic engineering process, the entrainment of air into the flow can be beneficial or disadvantageous. Referring to spillways, entrained air bubbles reduce the cavitation risk at the structure (Pfister and Hager, 2010), but at the same time decrease the energy dissipation of the spillway and increase the bulk flow height (Chanson, 1993). Advantages can be seen for the environment by the increase of dissolved oxygen concentration due to the strong mixing of water and air (Chanson, 1995). Even brief contact of the flow with a hydraulic structure increases the oxygen content at the tailwater side of the hydraulic structure, which is beneficial for the water quality of polluted waters (Baylar and Bagatur, 2006). A clear disadvantage is the entrainment of air into ship lock filling systems since the ascending air bubbles increase the forces occurring in the ship lock process (Schulze, 2018).
The classification of water-air mixtures is based on their type of generation (Lak-

shmana Rao et al., 1975). Accordingly, a distinction is made between local surface aeration and ambient surface aeration which both can often be observed at hydraulic structures. Local surface aeration is associated with the collision of water bodies or the impingement of a water body on a solid surface. Ambient surface aeration has no discrete location and occurs continuously along a water-air interface and is observed for wall-adhering flows in spillways (e.g. Chanson, 1996) and free-fall water jets (e.g. Hoyt and Taylor, 1975), whereby often no distinction is made between nappes and water jets in the literature (e.g. Chanson, 1994). Therefore, a definition for nappes is introduced in the following.

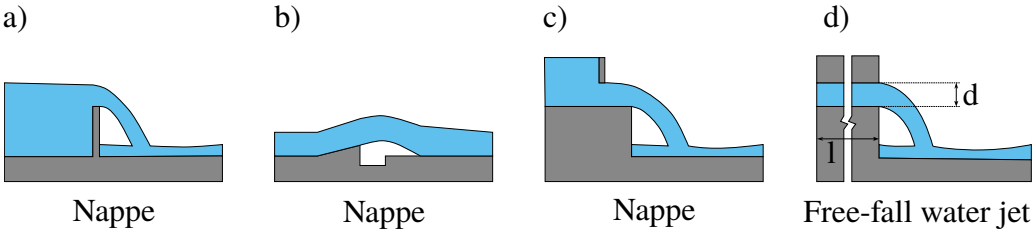

Fig. 2.1. Typical hydraulic flow situations to distinguish between nappes and free-fall water jets. Sharp-crested weir (a), chute aerator (b), undershot weir with back facing step (c), long channel with $l/d \geq 10$ (d).

Fig. 2.1 shows typical hydraulic flow situations. By the author's definition, nappes originate from flows over crests with an unrestricted top side of the water body and go through a free-fall phase in which there is no longer any contact with the hydraulic structure wall (see Fig. 2.1a,b,c). In this way, ambient pressure already prevails in the upper part of the water body before entering the free-fall area. In addition, the upper water body has no contact with the hydraulic structure wall which leads to a low diffusion of the boundary layer flow. Free-fall water jets (see Fig. 2.1d) originate from a long channel with $l/d \geq 10$ which enclose the water body until the transition into the free-fall area. The length of the channel exceeds the entrance length, resulting in a fully developed flow profile before the water jet discharges into the air. Water jets demonstrate self-similarity in flow velocity profiles across their longitudinal axis (Pope, 2000). This shows a clear demarcation between nappes and jets as they do not follow the self-similarity (Hager, 1995).

2.3 Applicability of Potential Flow Theory in Weir Flow Analysis

The potential flow approach is commonly used to analyze the flow patterns, such as velocity potential and stream functions, around weirs. However, this method is subject to strict limitations: the flow must be two-dimensional, steady, irrotational, incompressible, and inviscid. These conditions are rarely fully met in real-world flow scenarios, which affects the accuracy of the results, depending on how well the flow situation can be approximated.

Studies by Shirinzad et al. (2023) demonstrate, that vortex structures and recirculation zones occur in the vicinity of the weir, indicating that this area exhibits significantly higher complexity than the limitations imposed by strict mathematical aspects of potential flow theory. Furthermore, recent studies have highlighted the presence of very large-scale motions in rough-bed open-channel flows with streamwise lengths spanning 10-40 channel depths (Cameron et al., 2017). Thus, there is a possibility that these structures could influence the flow conditions near weir structures to such an extent that the validity of a potential flow approach diminishes.

Nevertheless, for flows around weirs, the applicability of potential flow is widely considered feasible and is extensively utilized. For instance, Afzalimehr and Bagheri (2009) who estimated the discharge coefficient of rectangular sharp-crested weirs and Heidarpour et al. (2008) who investigated velocity and pressure distributions at circular weirs. Both papers have successfully applied the potential flow approach in their studies on weir flows and report a good agreement with experimental data. It appears that the flow situation at weirs and the associated characteristics, such as flow velocity, overflow height, pressure distribution and discharge coefficient, are only slightly affected by the complex flow processes in the upstream regions of the weir. This implies that potential flow theory can provide valuable insights and reasonably accurate predictions for weir structures. However, it is important to acknowledge the limitations regarding the development of the nappe, particularly the impact of upstream turbulent structures. Especially in the context of this study, as these structures are suspected to significantly influence the development of the nappe in free fall.

Therefore, potential flow theory is not utilized in subsequent simulations that predominantly investigate nonlinear effects and the influence of upstream turbulence on nappe development.

2.4 Non-Stratified Flows of Nappes and Water Jets

A substantial number of theoretical and experimental studies have been conducted to determine the flow at weirs. Common weir types include sharp-crested, ogee crest, and circular-crested weirs, with the latter favored for flow measurement and water level control. The effects of various parameters on the discharge characteristics of circular-crested weirs have been studied by numerous researchers. Hager (1985) and Ramamurthy and Vo (1993) examined the discharge characteristics for different head water levels. Chanson and Montes (1997) analyzed the discharge characteristics under different inflow conditions, showing substantial effects on the discharge characteristics. For a given ratio of head on crest to curvature radius of the weir, the largest discharge coefficient is observed for inflow conditions with an upstream undular hydraulic jump, while the smallest discharge coefficient is found for inflow conditions with an upstream (normal) hydraulic jump. Castro-Orgaz et al. (2008); Castro-Orgaz (2008) studied the effect of streamline curvature on discharge characteristics, developed a potential flow equation and compared computed and measured discharge coefficients and the velocity and pressure distributions, finding good agreement. Heidarpour and Chamani (2006) developed a method to predict velocity and pressure distributions and compared with measured velocity distributions for different weir geometries, finding good agreement. Bagheri and Heidarpour (2010) used a vortex method to determine the weir discharge coefficient and the velocity values over the crest they compared their results with physical models of circular-crested weirs with various radii, heights and slopes and found good agreement.

Blazin (1890) was one of the first researchers to systematically investigate the velocity and pressure distribution at sharp-crested weirs. His work highlighted that as fluids approach a weir, there is a transition from a static hydrostatic pressure profile with a dynamic pressure component far from the weir to a pressure close to ambient pressure within the free-falling flow. At the weir crest, the pressure

already differs from hydrostatic pressure as it increases from the nappe surface, where ambient pressure prevails, to a maximum at $z/H = 0.34$ (H is the head of the overflow). A similar behavior was observed for velocity, which increases hyperbolically from the nappe top towards the nappe bottom. This type of pressure distribution over the weir crest is also confirmed by Rajaratnam and Muralidhar (1971), who experimentally determined the detailed distributions of velocity and pressure in the region of the weir crest. Ghobadian et al. (2013), who performed velocity measurements on circular-crested weirs with different surface roughness, also observed a hyperbolic velocity profile over the weir. Chanson (2021) also notes that the pressure distribution at the weir crest differs from hydrostatic, with the pressure being atmospheric at both the free surface and the lower nappe.

The initial pressure and velocity differences inside the nappe equalize due to internal friction as it descends. Furthermore, the nappe accelerates continuously, causing the angle of descent to approach the vertical, so that nearly the same atmospheric pressure prevails in the direction normal to the flow far away from the weir. Consequently, the pressure gradient in the normal direction becomes negligible. It should be noted, however, this zero-gradient assumption is only valid if the nappe is sufficiently ventilated, allowing atmospheric pressure to prevail on the side facing the weir.

Following a streamline from the top to the bottom of the nappe, the pressure is not constant. The hydrostatic pressure distribution of the ambient atmosphere changes with drop depth according to

$$P = P_0 e^{\frac{-gM(h-h_0)}{RT}} \tag{2.1}$$

with P the air pressure at altitude h, P_0 the pressure at the reference level h_0, T the temperature at altitude h, g the acceleration due to gravitation, M the molar mass of air and R the universal gas constant. The sloped and inclined streamlines in the narrowing nappe indicate the pressure changes within the water body (Hager, 1985), which, according to Bernoulli's principle, accompany the gravity-driven acceleration of the water body in free fall. Here, the question arises whether the water body itself contributes to the hydrostatic pressure, as in a stratified flow situation, or if it is only the ambient pressure profile. This phenomenon, crucial

to understanding the behavior of such flows, is elucidated in this section, building upon the concept of free-fall flow detailed in Section 2.2. A depiction of a nappe in this free-falling flow configuration is presented in Figure 2.2.

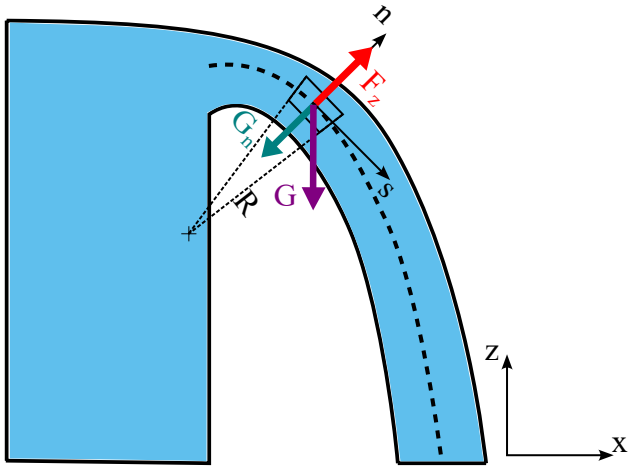

Fig. 2.2. Nappe falling from a sharp-crested weir. Streamline coordinates s in the streamline direction, n normal to s.

The relaxation of the hydrostatic pressure induces an acceleration within the flow, with the strongest effects observed at the bottom side. In the context of non-viscous, two-dimensional, steady-state flow, with ρ being constant within the water body, the motion of free-falling water jets and nappes is governed by the Euler equations, formulated here in streamline coordinates (refer to Fig. 2.2 for notation):
In the s-direction:

$$U\frac{\partial U}{\partial s} = -g\frac{\partial z}{\partial s} \tag{2.2}$$

And in the n-direction:

$$\frac{U^2}{R} = -g\frac{\partial z}{\partial n} \tag{2.3}$$

Here, U represents the velocity magnitude, and R stands for the radius of the streamline curvature. In classical mechanics, it is shown that all bodies in free fall experience the same acceleration, regardless of their mass and shape, if air resistance is neglected (Goldstein et al., 2002). As a consequence, the falling water particles cannot exert any gravitational-driven force on each other (apart from their

mutual gravitational attraction, which is negligibly small). Therefore, in a freely falling nappe, no hydrostatic pressure is generated by the water body itself, and only the hydrostatic pressure profile of the ambient pressure acts on the nappe.

In the following, an estimate is made to determine whether the hydrostatic pressure gradient of the surrounding air can have a significant influence on the nappe. For this purpose, the Bernoulli equation along a streamline is used:

$$\frac{1}{2}\rho v^2 + \rho g h + p = \text{const.} \tag{2.4}$$

The equation states that the kinetic energy is equal to the change in geodetic height and the ambient pressure.

For two points, Point 1 (top) and Point 2 (bottom) and assuming $v_1 = 0$ (nappe starts from rest), we get:

$$\rho g h + \Delta p_{\text{amb}} = \frac{1}{2}\rho v_2^2 \tag{2.5}$$

with $\Delta p_{\text{amb}} = p_1 - p_2$. The pressure difference due to the change in height for a nappe falling in air is determined by the surrounding air pressure. For 10 m drop depths, this results in $\Delta p_{\text{amb}} \approx 115$ J/m^3 (see Equation 2.1 for the ambient air pressure calculation).

If during the free fall all potential energy was converted into kinetic energy, the nappe would reach a velocity of about 14 m/s after a fall length of 10 meters, which corresponds to a kinetic energy of $E_{\text{kin}} \approx 98000$ J/m^3.

In this example, we observe that the kinetic energy of the nappe at the end of the fall is significantly higher than the pressure difference due to the surrounding air. This implies that the ambient pressure difference compared to the kinetic energy is small, indicating that the influence of the pressure gradient within the nappe is minimal.

Castillo et al. (2014) performed velocity measurements in a nappe using optical fiber probes for specific discharges of 0.037 m^{3}s^{-1}m^{-1} and 0.058 m^{3}s^{-1}m^{-1}. Drop depths of up to 2.2 meters were examined. Within the stated measurement accuracy, velocities comparable to those expected due to gravity were observed. This shows that for the investigated drop depth, the majority of the potential energy is converted into kinetic energy. Investigations by Bercovitz et al. (2016) con-

ducted studies on nappe with specific discharges ranging from 0.0255 $m^3s^{-1}m^{-1}$ to 0.1005 $m^3s^{-1}m^{-1}$, demonstrating that the theoretical velocity of the nappe due to gravity matches the measured velocity up to a drop depth of about 3 meters. For deeper drop depths, they observed a decrease in velocity, concluding that beyond this depth, energy dissipation becomes crucial. The data presented suggest that for larger specific discharges, the decrease in velocity occurs later.

For deeper drop depths, the conversion of potential energy no longer seems to lead to an increase in fall velocity. However, after a fall length of 3 meters, the nappe has a fall velocity of about 7.5 m/s, which corresponds to a kinetic energy of $E_{kin} = 28125$ J/m^3, which is still 2 orders of magnitude higher than the energy from the pressure difference of the ambient pressure. The fact that the nappe from the investigations of Bercovitz et al. (2016) does not increase in velocity after a fall length of 3 meters and even reduces its speed for deeper drop depths will be treated in a separate chapter (see chapter 2.9).

For a constant pressure within the nappe (normal to the flow direction) ($\partial P/\partial n = 0$), Equation 2.3 illustrates that the centripetal force ($F_z = U^2/R$) opposes the gravitational acceleration component in the n-direction, thereby determining the trajectory of the nappe. This means that a deformation on the surface of the nappe will move along with the trajectory of the nappe, and a displacement of the water body does not induce a restoring force, as would be the case in a stratified flow scenario. Thus, the density difference at the phase boundary exerts no stabilizing effect on the water-air interface.

2.5 Air Entrainment in Chute Aerator Nappes

Flows in chutes are wall-bounded and characterised by supercitical flows with $\geq$ 40 m/s resulting in a rough water surface, entrained air bubbles and water droplets in the air (Pfister, 2007). The transported air can be divided into entrained air bubbles and entrapped air which moves inside the unenclosed cavities of the rough water surface (Wilhelms, 1997). The entrainment of air bubbles is explained by breaking surface waves which enclosure air (Killen and Anderson, 1969) and by the ejection of droplets from the water body, which entrain air bubbles when they re-enter the water body (Volkart, 1980). It is recognized that the growth of

turbulence boundary layer on the hydraulic structure surface is the main cause of air entrainment (Chanson, 1993; Pfister and Hager, 2010; Bung, 2011). For wall-bounded flows, the turbulent boundary layer grows from the structure towards the water surface.

The growth rate of turbulence boundary layers on chutes is described by e.g. Annemüller (1958) by

$$\frac{\delta}{x} = 0.01 \tag{2.6}$$

with δ the boundary layer thickness and x the flow length from the start of boundary layer growth on the chute. The beginning of air entrainment is expected as soon as the turbulence boundary layer reaches the water-air interface and provides enough turbulent kinetic energy to overcome the restoring forces of surface tension, viscosity and gravitation. This point is called the inception point. From this point on, air is continuously entrained into the further developing flow. The air entrainment process of chutes can be classified as ambient surface aeration (Lakshmana Rao et al., 1975).

The starting point of air entrainment can be influenced by applying chute aerators (see Fig. 2.1b) which detach the boundary layer flow from the hydraulic structure wall (Kramer, 2004). The turbulence-rich boundary layer flow is then exposed to the air phase and the chute aerator nappe entrains air at its lower free surface (Kramer, 2004; Chanson, 1989). This allows the entrainment of air into the water body even before the boundary layer has diffused through the entire water level. Concerning the influence of upstream turbulence on the aeration process, Falvey and Ervine (1988) refer to unpublished work of the Bureau of Reclamation which shows an increase in entrained air when adding turbulence by tacking a screen to the ramp of an chute aerator. However, the aeration process of chute aerator nappes differs from the aeration process of sharp-crested weir nappes. The former nappes show the entrainment of air bubbles (Chanson, 1989) while the latter do not entrain air bubbles (Bercovitz et al., 2016).

2.6 Widening of Free-Fall Water Jets in Air

Round high speed water jets with velocities between 80 m/s and 200 m/s find their application in industrial cutting and cleaning processes (Guha et al., 2010). The water jets are divided into three regions in the streamwise direction (Leu et al., 1998). Starting from the nozzle, there is the potential core region which has a wedged-shaped inner water core. The surrounding water-air mixture has similar velocity as the core of the jet. In the next region, the inner core of the jet no longer exists. The jet is therefore considered to be fully aerated. Furthermore, this area is characterized by a high air entrainment rate due to which the water jet velocity decreases and the water jet widens. The last region is the diffused droplet region. In this region, the water jet is fully disintegrated into small droplets.

Round water jets with velocities of about 25 m/s were investigated for a strong accelerating nozzle geometry, resulting in laminar flow conditions of the exiting water jet. This results in a different flow pattern in the far field of the water jet. The water jet does not develop in an axisymmetric way, as previously discussed. Instead, the water jet shows helical deformations in the far field (Hoyt and Taylor, 1977a). Since the intensity of the deformation can be controlled by the outer air velocity, the momentum exchange with the surrounding air is still decisive for the widening of medium-velocity water jets.

Investigations on round water jets with velocities of 3 m/s to 30 m/s and diameters of 50 mm to 100 mm show huge differences in the jet surface shape depending on Reynolds number (Ervine and Falvey, 1987). The jet surface at 5 m/s and turbulence intensity of 5 % at the orifice shows a smoother surface with well rounded surface undulations compared to the jet at 25 m/s with comparable turbulence intensity. Sene (1988) also assumes that rough surfaces on water jets result from internal turbulence. The undulations on the water jet surface grow with time and finally lead to breakup into individual water packages. Higher turbulence levels at the orifice further reduce the breakup length (Ervine and Falvey, 1987).

2.7 Nappes at Weirs

Nappes at weirs can be divided into nappes with smooth surfaces, rough surfaces, oscillating nappes and nappes disintegrated into individual water packages (Tsang, 1987). These characteristics were recognized to be essential for the potential to form scour (Bollaert, 2004; Xavier Meriade Duarte, 2014) by determing the immersion depth of the nappe and the amount of entrained air (Baylar and Bagatur, 2006). Breakup lengths (l_b) of nappes are estimated with empirical formula of rectangular water jets given by Horeni (1956):

$$l_b = 6q^{0.32} \tag{2.7}$$

with q the specific volume flow. However, the estimated breakup lengths do not fit the observations of a sharp-crested weir nappes which show coherent water streaks over the entire length of the nappe (5 m) for the investigated specific volume flow rates of $q = 0.05$ to $0.1005\ m^2/s$ (Bercovitz et al., 2016). The slower development of nappes towards break-up compared to water jets is explained by an increase in interface turbulence production with increasing velocities (Kobus, 1985).
Modeling approaches have been developed to estimate the scour potential of nappes (e.g. Bollaert and Schleiss, 2005), building upon the insights of Ervine et al. (1997) who explore theoretically the lateral spread of circular water jets by assuming that the diameter of the jet is determined by the combined effect of the contraction of the jet due to gravitational acceleration and the spread of the jet caused by turbulence at the nozzle. Ervine et al. (1997) give

$$\epsilon = \frac{1.14TuU^2}{g}\left[\sqrt{\frac{2L}{D_0{F_0}^2}+1}-1\right] \tag{2.8}$$

for the widening of jets depending on the initial turbulence intensity Tu, the distance to the nozzle L, the initial diameter of the jet D_0 and the initial Froude number F_0.
Castillo and Carrillo (2012, 2013); Castillo et al. (2014, 2015); Carrillo et al. (2020a,b, 2021) adapt this relationship for nappes, describing the impingement nappe width B_j as a combination of the nappe thinning due to gravitational acceleration and the lateral spread of the nappe caused by turbulence effects.

$$B_j = \frac{q}{\sqrt{2gH}} + 2\zeta \tag{2.9}$$

with q the specific volume flow, H the fall height and ζ the lateral nappe spread. This is dependent on empirical parameters for rectangular jets as outlined by Ervine et al. (1997).

According to turbulence intensity measurements of water jets by Bollaert et al. (2002), Bollaert and Schleiss (2005) estimate initial turbulence intensity of nappes to be 0 to 3 %. The location for the initial turbulence intensity value is not defined in more detail. Turbulence production at the water-air interface is irrelevant for low velocity flows like sharp-crested weir nappes (u$\leq$ 3 m/s for $h \leq 0.9$ m) due to low initial velocity gradients (Ervine et al., 1997).

The paper by Castillo et al. (2014) presents numerical investigations of the flow behavior of a sharp-crested weir nappe with a drop depth of about 2.4 m, dropping into a basin. The study was conducted using a commercial computational fluid dynamics (CFD) software called ANSYS Fluent. Transient calculations over 60 seconds were performed at a frequency of 20 Hz. The transient statistics were obtained by considering that permanent conditions are reached after 20 s of simulation. The finest mesh size used in the numerical simulations has an edge length of 1 mm, which corresponds to half of the nappe width at the impingement conditions. The study evaluated the performance of four URANS turbulence models, namely the standard k-ϵ model, RNG k-ϵ model, k-ω based SST model and Omega-based baseline Reynolds stress model. The study utilized the Eulerian-Eulerian multiphase flow model to simulate the two-phase flow behavior. The model's inlet boundary conditions consider the mass flow rate and subgrid turbulent kinetic energy ($k_s = 0.00036$ m^{2}s^{-2} for $q = 0.058$ m^{3}s^{-1}m^{-1}, $k_s = 0.00019$ m^{2}s^{-2} for $q = 0.037$ m^{3}s^{-1}m^{-1} and $k_s = 0.00011$ m^{2}s^{-2} for $q = 0.023$ m^{3}s^{-1}m^{-1}). The outlet condition assumes an opening condition. The walls of the upper inlet channel, the weir, and the dissipation basing use no-slip wall conditions and smooth walls. Different upstream turbulence intensities ranging 1 % to 15 % 0.5 m upstream of the weir were investigated. The results show no influence of differences in turbulence intensities on the nappe characteristic.

Mokos et al. (2022) performed Smoothed Particle Hydrodynamics (SPH) simula-

tions on the test setup shown in Fig. 1.2 with a sharp-crested weir. In the simulation, the geometry of the experimental structure is accurately replicated, but to reduce computational expenses, adjustments have been made. Specifically, the length of the experimental tank has been shortened by removing the area further from the weir, where the experimental inlet is located. Instead, the simulation inlet has been positioned at the boundary opposite the weir. The inlet velocity has been modeled using a logarithmic velocity profile The aim of the research was to compare the trajectory of the nappe, the velocity of the nappe and the pressure conditions in the stilling basin with experimentally obtained data. The authors found good agreement with the experimental data regarding the pressure conditions. They utilized friction at the water-air interface as a tuning parameter to adjust the falling velocity of the nappe. In the provided article, the authors mention that they did not use a specific turbulence model. Instead, they suggest that the Lagrangian nature of SPH can be viewed as a simplified model of turbulence, akin to approaches such as Large Eddy Simulation (LES) or under-resolved Direct Numerical Simulation (DNS). The authors discuss an intriguing aspect of the internal structure of the nappe, particularly the appearance of voids in the experimental observations. They relate these voids to the dynamic properties of the flow, probably driven by inertia and surface tension. However, the SPH model used in the study exhibit a uniform distribution of particles throughout the nappe. The authors suggest that incorporating a turbulence model could provide valuable insights into the internal dynamics of the nappe, particularly in understanding the formation and behavior of voids.

Experimental investigations on a sharp-crested weir nappe were performed at the Hydraulics Laboratory of Universidad Politécnica de Cartagena (UPCT), Spain by (Carrillo et al., 2020a,b, 2021). A device specifically designed for the study of rectangular free falling jets was used which consists of an inlet channel of length 4 m and width 1.05 m, which ends in a rectangular sharp-crested weir with a vertical falling distance of 2.2 m. The aim of the experiment was to simulate and analyze the air entrainment in a rectangular free falling jet. To minimize the possible scale effects that may affect the initial conditions of the jet in the weir, two specific flow rates were analyzed (0.048 and 0.072 $m^3 s^{-1} m^{-1}$) with total head over the weir of 0.08 to 0.109 m. The air-water distribution was measured in eleven

cross-sections from the weir crest to a falling distance up to 2.0 m on perpendicular cross-sections which were obtained by considering the flow trajectory of the central nappe proposed by Scimemi (1937). The cross-sections were 0.2 m apart in the vertical direction. The water-air distribution was measured with conductivity probes with a spatial resolution of 1 mm in each cross-section, with the probe tip aligned with the streamlines of the flow. The studies identified the entrainment of air into the nappe as the cause of nappe widening. The quantity of entrained air is evaluated based on a phase change frequency similar to the bubble frequency used by Felder and Chanson (2013), in order to obtain a temporally averaged phase distribution. The investigations reveal that initially, there is clear water at the start of the nappe, but as it progresses, there is an increase in the phase change frequency.

The study conducted by Bercovitz et al. (2016) investigated the performance of a sharp-crested weir under conditions of comparable total head. Their model setup includes a tray with dimensions of 1 m in length and 0.4 m in width, representing a drop depth of 5 m for the nappe. The study examines flow rates of 0.0255, 0.05, 0.075, and 0.1005 $m^3 s^{-1} m^{-1}$. In these investigations, however, no air bubbles were seen inside the nappe. This suggests that nappe flows at weirs cannot be categorized as ambient surface aeration flows like water jets according to Lakshmana Rao et al. (1975).

2.8 Nappe Vibration at Weirs

The appearance of nappe vibrations is characterized by spatial regular wave fronts which result in acoustic emissions (Lodomez et al., 2019). The investigated nappes have drop depths of about 3 m to 4 m. Fig. 2.3 gives an overview over investigated weir crest geometries.

Crookston et al. (2014); Lodomez (2016); Anderson and Tullis (2018); Lodomez et al. (2018, 2019) investigated quarter round weir crests (Fig. 2.3a) or half round weir crests (Fig. 2.3c). Kitsikoudis et al. (2021) extend the examined weir crest types by a variety of different geometries: quarter round with extension Fig. 2.3b, truncated half round Fig. 2.3d, rectangular Fig. 2.3e, rectangular with rounded edge on upstream side Fig. 2.3f. For the rectangular weir crest (Fig. 2.3e) with

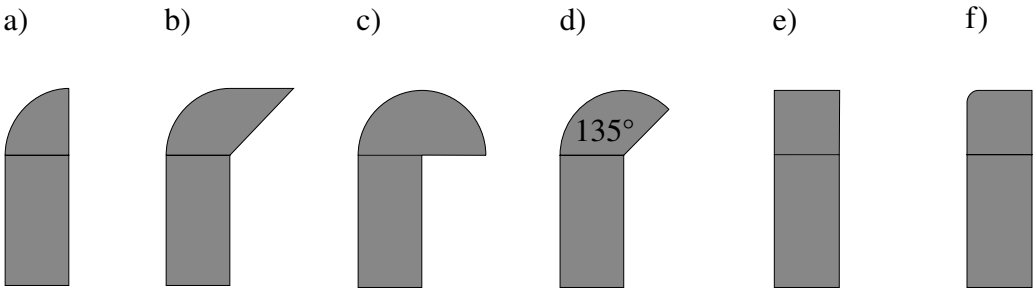

Fig. 2.3. Overview over investigated weir crest geometries with regard to nappe vibration. Flow from left to right. Quarter round (a), quarter round with extension (b), half round (c), truncated half round (d), rectangular (e), rectangular with rounded edge on upstream side (f). For more information on the geometry of b,c,d,e,f see (Kitsikoudis et al., 2021).

thickness=5 cm and q ranging $0.01 - 0.06$ m^2/s no nappe vibration was observed, however the same weir crest with a rounded edge on the upstream side Fig. 2.3f (R=1 cm) showed nappe vibration for $q = 0.023$ m^2/s (Kitsikoudis et al., 2021). Kitsikoudis et al. (2021) therefore suspect the sharp deflection at the upstream edge of the rectangular weir crest to be the reason for the lack of nappe vibration. Enclosed air behind the nappe is not necessary and nappe vibration is also seen for fully ventilated nappes (Anderson and Tullis, 2018; Lodomez et al., 2018). However, enclosed air behind the nappe acts as an amplification of the effect by an oscillation of positive and negative pressure (Anderson and Tullis, 2018; Lodomez et al., 2018). With regard to the impact situation at the tailwater side, the vibrating nappe has an enlarged impact area. However, the effect of nappe vibration is limited to low head water levels and disappears for unit discharges higher than 0.055 m^2/s (Lodomez et al., 2019). In addition, the effect can be mitigated by introducing upstream turbulence (Crookston et al., 2014).

Finally, there is energy-dissipation due to viscosity which can be counted among the holding forces. By reducing the turbulence kinetic energy at the interface, the phase-mixing potential is decreased and thereby this increases the interface stability.

2.9 Boundary Layer Stability at the Water-Air Interface

In chapter 2.4, it has already been mentioned that investigations of Bercovitz et al. (2016) show deviations in the fall velocity of nappes from the theoretically achievable velocity due to gravity, and there is even a decrease in nappe velocity at greater drop depths. This chapter will now discuss a possible cause for the observed development of the fall velocity. Ervine et al. (1980); Ervine and Falvey (1987); Ervine et al. (1997), all state that air entrainment in water jets is influenced by turbulence acting at the water-air interface. For nappes, turbulence is also considered an important influencing parameter in nappe widening (Castillo et al., 2015; Castillo and Carrillo, 2017a,b; Carrillo et al., 2020a,b, 2021). Bollaert and Schleiss (2002) estimate the turbulence intensity at weirs to be relatively low (0 % to 3 %). This raises the question of whether instabilities produced by shear stress at the water-air interface could lead to nappe widening. Therefore, this chapter will focus on the flow conditions at the water-air interface, emphasizing the potential for the development of instabilities at this interface.

Newton's third law states that forces acting are in equilibrium. Hence, shear stress needs to be continuous at the water-air interface:

$$\mu_w \frac{\partial u_w}{\partial y} = \mu_a \frac{\partial u_a}{\partial y} \tag{2.10}$$

with the dynamic viscosity of water $\mu_w = 10^{-3}$ Ns/m^2, the dynamic viscosity of air $\mu_a = 1.8 \cdot 10^{-5}$ Ns/m^2, u_w and u_a the velocity of water and air, in the direction parallel to the water-air interface and y the direction normal to the water-air interface. Given the large difference in dynamic viscosity between water and air ($\mu_a/\mu_w \approx 0.02$), the shear stress balance at the interface leads to a much higher velocity gradient in the air phase and the jump in viscosity leads to a sharp slope in the velocity profile. Hence, the velocity profile has no inflection point at the interface, but is continuous due to the no-slip condition at the interface. The boundary layer thickness for laminar boundary layer flows along a flat plate is approximated by (Pope, 2000)

$$\delta \approx \frac{5x}{\sqrt{Re_x}}. \tag{2.11}$$

Eq. 2.11 shows that the boundary layer thickness is proportional to the square root of the kinematic viscosity ($Re = u \cdot x/\nu$). Hence, the boundary layer in the air phase is four times thicker than the boundary layer in the water phase ($\sqrt{\nu_a/\nu_w} \approx 3.86$). A velocity profile in the water phase is measured by Okuda (1982) for air blowing over initial calm water to form waves with air velocity of 6.5 m/s and shows a linear decreasing velocity profile in the water phase over $\sim$ 3 mm starting from the water surface. Shaikh and Siddiqui (2008) measured velocity profiles in air blowing over water by using particle image velocimetry for air velocity up to 4.4 m/s and show logarithmic velocity profiles with the lowest velocity at the water-air interface. The findings from wind over water can be partially transferred to nappes as the physics behind the momentum exchange is the same.

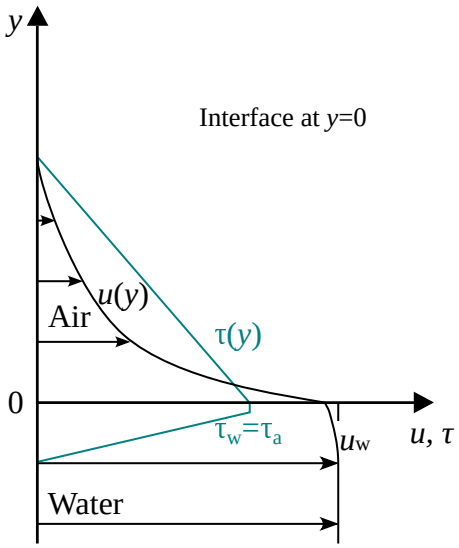

Fig. 2.4. Schematic velocity and shear stress profile at the water-air interface for moving water.

Fig. 2.4 shows a schematic velocity distribution at the water-air interface for moving water in calm air. The water moves with the velocity u_w. At $y = 0$ (water-air interface) air and water move with the same interface velocity u_i and for $y- > \infty$ the velocity is zero.

The stability of boundary layers on flat plates is described by the Orr-Sommerfield equation which is a simplification of the Navier-Stokes equation by assuming a parallel flow situation where velocity is only a function of the normal distance to the plate y. Both experimental and analytical studies show that boundary layers without inflection point can stay stable up to a critical Reynolds number of $Re_{\delta^*,\text{crit}} \approx 520$ where δ^* is the displacement thickness of the boundary layer or $Re_{x,\text{crit}} = 91000$ where x is the cord length of the boundary layer (White, 1991). The neutral curve of the Orr-Sommerfield equation gives the disturbances that neither grow nor decay. The smallest unstable wavelength is of the order of $\lambda \approx 6\delta$ (White, 1991).

Given the discussion above, there is a possibility for the formation of instabilities on the nappe surface due to shear stress. The significant difference in viscosity between water and air causes a sharp velocity gradient at this interface, and although the velocity profile is continuous, the lack of an inflection point indicates that the boundary layer remains stable up to a critical Reynolds number. Beyond this critical point, disturbances may start to grow, leading to potential instabilities. These instabilities could be one of the reasons for the deviations in the fall velocity of the nappe observed by Bercovitz et al. (2016) compared to the theoretically calculated value due to gravity. The significant widening of the nappe, described even as breakup, increases its interaction area with the surrounding air which appears to be a plausible explanation for the observed decrease in the nappe's fall velocity.

2.10 Numerical Modeling of free-Surface Flows

The following section outlines two-phase flow models that are intended for simulating free-surface flows. Free surfaces are commonly encountered in various flow situations, such as ocean waves, bubbly flows, and industrial processes involving liquid-gas interfaces. Here, some of the difficulties associated with modeling free-surface flows, along with current approaches to address these challenges are discussed.

The Two-Fluid Method, also known as the Euler-Euler method due to its use of an Eulerian reference frame for both fluids, is most suitable for two-phase flows

where the interface is much smaller than the chosen grid size (Yan and Che, 2018). In this approach, the interface is not directly resolved, but interface processes are accounted for. This is achieved by solving the mass conservation and momentum conservation equations separately for both phases. The latter equations include a source term that facilitates momentum exchange between the phases. However, this source term is empirical, making the development of suitable models for momentum exchange the greatest challenge in two-fluid models.

In **The Mixture Model Approach**, each phase is treated as a continuous medium that interpenetrates with the other phases. The model assumes that the phases share the same velocity field, which is a weighted average based on the volume fractions of the phases. Each phase is represented by a volume fraction, indicating the proportion of that phase within a computational cell. The sum of the volume fractions for all phases in a cell is always equal to one. The mixture model employs a set of conservation equations for mass and momentum. Similar to the Euler-Euler approach, these equations include terms for interactions between phases, such as drag forces. The physical properties of the mixture, such as density and viscosity, are calculated as weighted averages of the properties of the individual phases, based on their volume fractions. A relative velocity between phases, also known as slip velocity, can be accounted for. This slip velocity represents the difference in velocity between the phases and is used to model the interphase momentum transfer. Overall, the mixture model can be seen as a simplified version of the Euler-Euler model, requiring less computational effort and less closure assumptions (Brennan, 2001).

The Volume of Fluid (VOF) Method introduced by Hirt and Nichols (1981) stands as a widely embraced technique among interface capturing methods. It operates by discretizing the computational domain into fixed cells, determining the surface via a void fraction. Hence, VOF methods inherently conserve mass. However,VOF methods can suffer from numerical diffusion, particularly near the fluid interface, leading to inaccuracies in interface sharpness. With the goal of minimizing numerical diffusion, a second class of methods known as "interface tracking methods" has been developed. In these approaches, the free surface is positioned at one boundary of the mesh, and the mesh undergoes deformation as the free surface shifts. However, this significantly limits the flow situations that

can be investigated, as a highly deformed mesh can lead to stability issues in the calculation.

The Level Set Method introduced by Osher and Sethian (1988) stands as another grid-based technique for modeling free surfaces and air entrainment in numerical simulations. In contrast to the VOF method, the position of the phase boundary is defined by a Level-Set function given by

$$\frac{\partial \phi}{\partial t} + \mathbf{U} \cdot \nabla \phi = 0. \tag{2.12}$$

This function assigns a value to each point in the computational domain, representing the distance to the phase boundary. Positive values represent points inside the phase, negative values represent points outside, and zero values correspond to the boundary itself. However, a significant drawback of the Level-Set method is its susceptibility to unphysical loss of fluid mass because of the necessity to regularly reinitialize the function to maintain an accurate representation of the phase boundary.

Euler-Lagrangian Approaches can be used for multiphase flows with one continuous and one dispersed phase. The conservation equations of the continuous phase are solved in an Eulerian reference frame, which is a fixed coordinate system. The dispersed phase is modeled in a moving coordinate system. The equation of motion for the Lagrangian particles is described by the forces acting on the particles, including gravity, drag force, buoyancy force, pressure gradient, and contact force (Matysiak, 2007). The coupling to the continuous and the dispersed phase can either be unidirectional, where the forces from the flow affect the particles, or more complex, where the forces from the particles also influence the flow, and the particles interact with each other through collisions. Since a separate force balance must be established for each particle, the computational effort increases with the number of particles.

Smoothed Particle Hydrodynamics (SPH) presents a mesh-free approach suitable for simulating intricate fluid flows characterized by free surfaces and air-entrainment. SPH discretizes fluid properties into particles and employs kernel functions to calculate fluid properties at each point in the domain. This method is well-suited for problems involving large deformations, complex geometries, and

fluid-structure interactions. However, the choice of kernel function and smoothing length can significantly impact simulation accuracy and stability and require tuning for the specific flow situation.

2.11 Numerical Modeling of Air Entrainment

Air entrainment occurs when air is introduced into the liquid phase, creating bubbles or forming a frothy mixture. This is common in processes like breaking waves, waterfall impact, or industrial processes involving liquid jets. The widening of free fall water flows like water jets and nappes is often associated with air entrainment. Albeit, nappes, as studied by (Bercovitz et al., 2016) in a laboratory model of a sharp-crested weir with a 5 m drop depth, do not exhibit air bubble entrainment. However, nappe surface deformations and rough nappe surfaces are observed (Tsang, 1987), which could be precursors of breaking surface waves which lead to air entrainment for water jets (Hoyt and Taylor, 1975, 1977b,a). Therefore, similar air entrainment could occur in nappes under much harsher conditions, such as significantly deeper drop depths. However, for the case in question, the drop depths do not seem sufficient to cause actual air entrainment on the nappe surface. This is consistent with the observations of the author in a laboratory model with a drop height of 7.5 meters, which already represents a typical scale for the weir structures in focus here.

For large-scale models that focus on the conditioning of the tailwater side of weir, the direct simulation of the nappe surface exceeds the currently available computing capacities. The use of RANS and URANS simulations will therefore remain the workhorse for hydraulic engineering issues processing large-scale flow situations for years to come (Rodi, 2017; Bombardelli, 2020; Maulik et al., 2021; Brenner et al., 2022; Song et al., 2022). The model idea of URANS models is to extend the traditional Reynolds-Averaged Navier-Stokes (RANS) approach by incorporating time-dependent terms, allowing for the simulation of transient and unsteady turbulent flows. In the context of a large-scale model setup, however, this is reaching its limits for the resolution of highly dynamic nappe surfaces. Therefore, the question arises whether an air entrainment model can be used to model the widening of nappes in URANS simulations.

Several air entrainment models were developed for URANS simulations, each for a specific air entrainment mechanism and situation in mind. All of them identify collapsing cavities at the water-air interface as the major cause for air entrainment. An air entrainment model for predicting the location of air entrainment was developed and used for predicting air entrainment around naval surface ships (Ma et al., 2011b), at a hydraulic jump (Ma et al., 2011c), at a plunging liquid jet (Ma et al., 2011c) and at a surf zone breaking wave (Ma et al., 2011a). A more general air entrainment model is implemented in the simulation software FLOW-3D within the Volume-of-Fluid method and tested on plunging jets, drop shafts, hydraulic jumps and spillways (Hirt, 2003). Since Flow3D is a commercial code, there is not much information concerning the implemented equations and the procedure. The basic idea of the model is that air is entrained into the flow when the stabilizing effects of surface tension and gravity are overcome by turbulence. The entrainment of air is realized by a source term which is implemented in the volume fraction transport equation and controlled by an air entrainment factor. This factor was calibrated for predicting self-aerated spillway flows (Valero and García-Bartual, 2016).

Another air entrainment model was developed for estimating the local air entrainment of ship bow waves by using the one-phase level-set method within the OpenFOAM® environment (Moraga et al., 2008). The model is based on threshold values for the velocity normal to the water-air interface pointing towards the liquid phase and for the velocity pointing into the vertical direction. Both need to be higher than 0.22 m/s for starting the entrainment of air.

A similar approach was chosen for the development of an air entrainment model for predicting the self-aeration process of chutes within the Volume-of-Fluid method (Lopes, 2017). Here, a threshold value of 0.8 m/s is used for the velocity normal to the water-air interface pointing towards the liquid phase and for the velocity pointing into the vertical direction. The model is expanded by an additional threshold for the turbulent kinetic energy at the free surface which needs to overcome 0.2 m^2/s^2. All threshold values need to be overcome to start the entrainment of air.

All the existing models are developed for stratified flow situations which are defined by a density variation in the direction of the gravity-induced pressure

gradient. Then, the pressure gradient acts as a conserving force for the water-air interface. This does not fit the requirements of free-falling nappes. For the conservation of the nappe-shape, gravity has no effect since there is no pressure gradient in the free-falling water body and centrifugal force due to nappe curvature counterbalances the gravitational acceleration component in normal direction to the resulting velocity vector (as shown in section 2.4). Hence, these models cannot be used for modeling the development of nappes.

2.12 Modeling Turbulence at Water-Air Interfaces

Two-phase flow turbulence can be either modeled with individual transport equations for the subgrid turbulence properties for every phase, including exchange terms or by mixture turbulence models which solve for the turbulence of the resulting two-phase mixture. The latter have proven to be suitable for stratified flow situations where the mixture mainly consists of one fluid. Hence, these models are widely used for hydraulic engineering approaches. However, difficulties arise for modeling turbulence at the high density gradient water-air interface. By assuming ρ to be constant over the interface area, turbulence properties can freely be exchanged between the phases. This behavior is not physically correct. Since the turbulent fluctuation is related to the moving mass, the density gradient affects the transport of turbulence properties. Moreover, for stratified flow situations the water-air-interface acts like a deformable wall and dampens turbulence in perpendicular direction to the interface (Fulgosi et al., 2003).

The main focus of the current modeling approaches of turbulence at high density gradient interfaces is on the one hand side the consideration of the density in the transport equations and on the other hand side the damping of the turbulence at the interface for stratified flow situations. As a good example the model of Egorov et al. (2004) can be named which dampens turbulence at the interface by an additional source term in the energy dissipating transport equation. Since this model suffers from mesh dependency, Fan and Anglart (2019) propose an alternative method which is based on computing of the turbulence damping length scale. The damping of turbulence is considered to be the same on both interface sides which tends to underestimate the turbulence in the higher density phase.

Since there is no stratified flow situation within nappes and free-fall water jets, this kind of turbulence treatment is not necessary for the modeling process.

2.13 Experimental Investigation of Flows with Air Entrainment

2.13.1 Limitation of Froude Scaled Models

Experimental investigations of free surface flows with air entrainment are usually carried out with Froude scaled models. Since air entrainment processes are also determined by Weber number and Reynolds number, Froude scaled models will have scale effects (Ervine and Ahmed, 1982; Ervine and Falvey, 1987; Chanson, 2009; Bollaert, 2002). By applying Froude similarity, turbulence effects are underestimated and the effects of surface tension is overestimated (Heller, 2011). Hence, the geometric scaling ratio of Froude models ($l_{\text{model}}/l_{\text{prototype}}$) must be limited or Reynolds number and Weber number must be in an adequate range, to ensure that modeling effects remain small. For stepped spillways, investigations indicate that the maximal geometric scale ratio is about 1:10 to 1:15 for investigating void fraction and mixture flow velocity (Boes, 2020; Chanson, 1989). For avoiding relevant scale effects of turbulence and air bubble size in high-speed air-water flows, either $We > 19600$ or $Re > 1.5 \cdot 10^5$ to $Re > 3 \cdot 10^5$ must be satisfied (Pfister and Chanson, 2012). It is noted that void fraction and velocity are less dependent on scaling ratios. However, if the investigation relates to air bubble sizes and turbulence, then the recommended maximum geometric scaling ratio is reduced to 1:3 or even 1:2 (Pfister and Chanson, 2014).

2.13.2 Measuring Void Fraction

The beginnings of water-air studies were carried out with backflushing pitot tubes for measuring void fractions in chutes (Ehrenberger, 1926). Nowadays, there are several methods for measuring void fraction which can be non-intrusive or intrusive. Non-intrusive methods are used for measuring spatially averaged void fractions over a line or in a volume. For bubbly flows in pipe systems ultrasonic

technique (e.g. Chakraborty et al., 2009; Carvalho et al., 2009), radiometric density meter (e.g. Schulze, 2018) and capacitance technique (e.g. Ma et al., 1991) were applied. The first two methods mentioned are based on difference in absorption of sound respectively radiation for water and air. The latter method takes advantage of the difference in the dielectric constant of water and air. The measurements are spatially averaged since the void fraction over the entire pipe cross-section influences the measurement signal.

Void fractions at certain points in space are measured with intrusive methods. For these kind of single-point measurements, optical fiber probes (e.g. Cartellier, 1990; Boes, 2000; Kramer, 2004; Pfister, 2007; Florez et al., 2016; Guyot et al., 2016) and conductivity probes are typically used.

The measurement of void fraction with conductivity probes is based on the huge difference in electrical conductivity between water and air (Herringe, 1973; Muñoz-Cobo et al., 2017). The probe consists of two electrodes which are electrically isolated (Chanson, 1997). While the tip of the probe is covered in water, electricity can easily flow between the two electrodes. This circuit is open when air blocks the connection between the two electrodes. The measuring principle was first used by Lamb and Killen (1950), whereby the two electrodes were spatially separated from each other. Probes used today have a much smaller distance between the two electrodes (a few millimeters) and the electrodes are less than 1 mm in diameter (e.g. Toombes and Chanson, 2007; Bung, 2011; Muñoz-Cobo et al., 2017; Carrillo et al., 2020a). Depending on the design, conductivity probes vary in the number of tips.

The most simple method for evaluating the void fraction is to apply a single voltage threshold value (V_t) to distinguish between phases. $V_t = 0.5(V_l - V_g)$ is a typically used threshold where V_l is the voltage level in the liquid phase and V_g is the voltage level in the gas phase (e.g. Toombes and Chanson, 2007). This method has proven to be very stable. However, each phase change from water to air comes with a drying process of the probe tip which is accompanied by sub-threshold voltages at the begin of the drying process. Hence, the single threshold method underestimates the time of the probe tip being inside the air phase. This can be counteracted by applying two threshold values (e.g. Boes, 2000; Kramer, 2004). By doing so, the threshold can be closer to the physical air phase, but also increases the risk of

detecting artificial phase changes due to choosing a threshold value which is inside the noise level of the conductivity probe. For preventing artificial detections, some methods rely on an additional condition. The detection of a phase change is linked to a monotonically increasing respectively decreasing voltage signal. This extension was applied with single threshold methods (e.g. Muñoz-Cobo et al., 2017) as well as for double threshold methods (e.g. Thorwarth, 2009). Due to the differences in the methods, the results of void fraction measurements are highly sensitive to the chosen evaluation method (Bung, 2012; Thorenz and Grefenstein, 2022).

2.14 Summary

The currently used methods for evaluating hazard risks of downstream fish passages at overflown weirs based on fall height and tailwater level are not sufficient to evaluate the complex hydraulic flow situation at overflown weirs (Thorenz et al., 2018). The nappe characteristic is decisive for air entrainment and immersion depth of the nappe at the tailwater side (Baylar and Bagatur, 2006) which also affect the hazard risks of fish migration due to collision with obstacles and the risk of predation (Odeh et al., 2002).

In the reviewed literature, there is often no differentiation between nappes and free-fall water jets. Accordingly, knowledge gained from water jets is transferred to sharp-crested weir nappes. Breakup length of nappes were estimated using empirical formulas for breakup length of water jets given by Horeni (1956) and nappe widening is seen to origin in surface aeration similar to water jets (Carrillo et al., 2020a,b, 2021). However, it is shown that sharp-crested weir nappes with drop depths of 5 m still consist of coherent structures that can be followed from the weir crest to the bottom and that there are no air bubbles inside nappes (Bercovitz et al., 2016).

In this work, a distinction is therefore made between water jets and nappes. The upstream flow situation of the free-fall area is used as a differentiation criterion. Water jets origin from an enclosed area with $l/d \geq 10$, leading to a fully diffused boundary layer over the water jet cross section. In this situation the friction at the structure is the main origin of turbulent kinetic energy which, depending on the

kinetic energy level, deforms the water air interface and entrains air by breaking surface waves and collapsing cavities (Killen and Anderson, 1969). Nappes are defined by not having a fully diffused boundary layer when entering the free-fall area.

The entrainment of air and the deformation of the water-air interface can be counteracted by gravity, surface tension and viscosity. For free-falling flow situations like nappes and water jets with a horizontal velocity component, centrifugal force counterbalances the gravitational force component normal to flow direction. Therefore, gravity has no stabilizing effect on the water-air interface and necessary kinetic energy for deforming the water-air interface is reduced.

Turbulence production at the water-air interface is decisive for the development of water jets with high initial velocities. For initial velocities ≤ 3 m/s, this type of turbulence production is negligible (Ervine et al., 1997).

There are numerical modeling approaches for air entrainment situations of stratified flows within unsteady Reynolds-averaged Navier Stokes simulations (URANS). All of the models accept turbulent kinetic energy as the driving force of air entrainment and gravity and surface tension as the conserving forces. Hence, these kind of models are not suitable for non stratified flows like nappes.

Turbulence modeling for hydraulic engineering approaches is widely based on mixture models which solve for the turbulence of the resulting two-phase mixture. These models assume ρ to be constant over the interface area which leads to physically incorrect behavior at the water-air interface. Current modeling approaches aim for dampening turbulence at the water-air interface (Egorov et al., 2004; Fan and Anglart, 2019). However, for free falling flows turbulence damping is not essential since for non stratified flows there is no pressure gradient in the direction of the density gradient and hence gravity has no restoring effect on the water-air interface.

2.15 Aims and Objectives

The literature review indicates that turbulence influences the characteristics of free jets. The origin of turbulence is considered to stem from both the flow conditions at the nozzle and the shear stress at the water-air interface. However, both factors

seem to have minimal impact on nappes at sharp-crested weirs. This is partly due to the limited boundary layer growth induced by the sharp-crested geometry of the weirs and the relatively low velocities over weirs compared to water jets typically studied in research on jet spreading and air entrainment. Nonetheless, nappes at prototype scale exhibit deformations on the nappe surface, extending over the entire length of the nappe, which become visible already at the weir crest. In this work, the hypothesis is proposed that turbulence generated upstream of the weir may influence nappes. Hence, the study aims to investigate the influence of upstream turbulence on the development of nappe flows over sharp-crested weirs during the free fall. Specifically it aims to examine the correlation between the intensity of upstream turbulence and the widening of the nappe. Additionally, it endeavors to evaluate the effectiveness of URANS turbulence models in depicting the development of the nappe during free fall.

The objectives to achieve these goals are as follows:

Assess the Influence of Upstream Turbulence Intensity:

Vary the upstream turbulent intensity within numerical simulations using LES simulations to see if upstream turbulence effects the development of nappe flows during the free fall. Quantify the relationship between upstream turbulence intensity and nappe widening.

Evaluate the URANS Turbulence Models:

Utilize URANS turbulence models and compare results from LES simulations to assess the predictive capability of URANS turbulence models.

Conduct Experimental Investigations:

Conduct experimental tests under controlled conditions to observe the development of nappe flows and compare them with numerical simulation results. Qualitatively assess the agreement between experimental observations and numerical predictions to validate the accuracy of the simulations.

By accomplishing these objectives, this study aims to deepen our understanding of nappe flows, particularly focusing on their development during free fall and its dependence on upstream turbulence.

Chapter 3

Numerical set-up and pre-validation

3D numerical investigations are performed using the Volume-of-Fluid method (VOF) with Large Eddy Simulations (LES) and unsteady Reynolds-averaged Navier Stokes (URANS) models to evaluate the influence of upstream turbulence on the development of a nappe flowing over a sharp-crested weir. For this purpose, the modeling process of turbulence in two-phase flow simulations is discussed and the chosen evaluation method for nappe widening is presented. The numerical investigations of nappes are preceded by preliminary studies concerning the formation of artificial velocities at the water-air interface, the generation of upstream turbulence, mesh independence studies and by the influence of an artificial compression term in the VOF equation.

3.1 Modeling of Two-Phase Flows

The Volume-of-Fluid (VOF) method is utilized for modeling the two-phase flow scenario of nappes. This method is chosen due to its inherent conservation of mass and its avoidance of surface reconstruction or the calibration of exchange terms between the phases. In the modeling approach, an incompressible and isothermal flow regime is assumed, where advection plays a dominant role in mass transport ($Pe >> 1$):

$$Pe = \frac{uL}{D_\mathrm{m}} \tag{3.1}$$

with u the velocity, L the characteristic length and D_m the molecular diffusivity. For calculating the flow of the nappe, the spatially filtered or time-averaged incompressible Navier Stokes and the continuity equations for LES and unsteady RANS, respectively, coupled with the VOF method to account for the water and air phase (Hirt and Nichols, 1981) are given by:

$$\nabla \cdot \overline{\boldsymbol{U}} = 0 \tag{3.2}$$

$$\frac{\partial(\rho\overline{\boldsymbol{U}})}{\partial t} + \nabla \cdot (\rho\overline{\boldsymbol{U}\boldsymbol{U}}) = -\nabla p_\mathrm{rgh} + \nabla \cdot (\tau^\nu + \tau) - g \cdot \boldsymbol{x}\nabla\rho + \sigma_\mathrm{st}\kappa\nabla\alpha. \tag{3.3}$$

Here, ρ denotes the density, $\overline{\boldsymbol{U}}$ the spatially filtered or temporally averaged velocity vector, p_rgh the pressure minus the hydrostatic component, τ^ν the viscous stress tensor, τ the turbulent sub-scale stress tensor, g the gravitational acceleration and $\boldsymbol{x}$ the position vector. The last term on the right-hand side denotes the surface tension force with σ_st the surface tension, κ the curvature of the interface and α the volume fraction of water. In addition, Eq. 3.4 is solved for tracking the volume fraction:

$$\frac{\partial\alpha}{\partial t} + \nabla \cdot (\overline{\boldsymbol{U}}\alpha) = 0 \tag{3.4}$$

The resulting fluid properties are calculated by a volume-fraction-based-mixture

$$\phi_\mathrm{m} = \alpha\phi_\mathrm{l} + (1 - \alpha)\phi_\mathrm{g}, \tag{3.5}$$

where ϕ_l denotes the water-phase property and ϕ_g denotes the air-phase property.

The α-transport equation used for the presented investigations has an additional term on the left-hand side for counteracting numerical diffusion (Rusche, 2002),

$$\frac{\partial \alpha}{\partial t} + \nabla \cdot (\overline{\boldsymbol{U}}\alpha) + \nabla \cdot (\alpha(1-\alpha)U_\mathrm{r}) = 0 \tag{3.6}$$

where

$$U_\mathrm{r} = ((1 - c_{\mathrm{i}\alpha})c_\alpha |U_\mathrm{sf}| + c_\alpha c_{\mathrm{i}\alpha} |\overline{\boldsymbol{U}}|) \frac{\nabla \alpha}{|\nabla \alpha|}, \tag{3.7}$$

with c_α the face-flux compression coefficient and $c_{\mathrm{i}\alpha}$ the isotropic compression contribution as user defined values, U_sf being the velocity in surface normal direction. For the simulations carried out within this thesis, $c_\alpha = 0.1$ and $c_{\mathrm{i}\alpha} = 0.1$ was chosen as a result of a sensitivity study (see section 3.4.8).

Accuracy and stability play an important role in the solution process of the conservation equations. In addition, the computational costs for reaching the solution are not negligible. A good compromise between the three is in most cases the motivation for choosing the following numerical methods and settings.

To guarantee the conservation of quantities, the finite volume method is used for the discretization in space on a collocated grid which eases to solve the equations, as all parameters are stored at the same location. To avoid chequerboard oscillations, a correction term is added to the linear interpolation of the face fluxes (Rhie and Chow, 1983).

For temporal discretization a mixed implicit explicit Crank-Nicolson scheme with second order accuracy is used. Within OpenFOAM® a Crank-Nicolson weighting coefficient is used which gives for zero pure Euler and for one pure Crank-Nicolson. Within these investigations, a Crank-Nicolson coefficient of 0.3 is used since higher values led to instabilities at the water-air interface of the nappe. The boundedness of the phase-fraction is preserved by using the mules flux correction algorithm (Boris and Book, 1973) on the α field. The iterative solving process of the momentum equation and the coupling of the pressure and the velocity field is done by the pimple algorithm which is a combination of the SIMPLE (Semi-Implicit Method for Pressure-Linked Equations) and PISO (Pressure Implicit with Splitting of Operator) procedures as described by Greenshields and Weller (2022). The steps of the solving procedure are shown in Fig. 3.1.

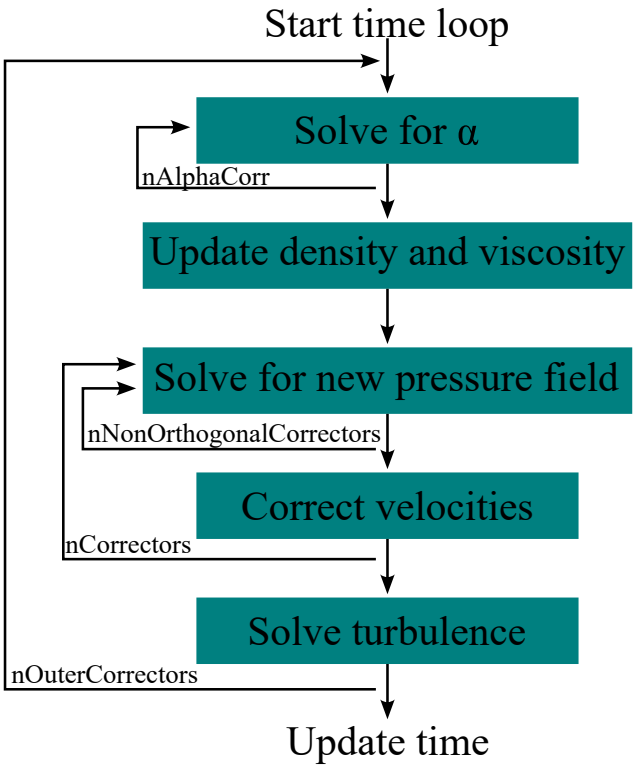

Fig. 3.1. Solving procedure.

At a new time step, the α field is calculated by using the previous time step velocity field. The new α field is then used to update density ρ and viscosity ν. A new pressure field is calculated, which is used to correct the velocity field. The turbulence transport equations are solved in the last step of the solution procedure. The stability and accuracy of the solution is improved with four corrector loops. For better identification OpenFOAM®-specific designations of the corrector loops are given: nAlphaCorr defines the number of iterations of the phase fraction equation for a solution step. nNonOrthogonalCorrectors defines how often the pressure equation is recaculated for correcting non-orthogonality mesh effects. nCorrectors defines how often the momentum equation is recalculated with corrected fluxes. nOuterCorrectors defines the number of the solution process runs over the entire system with all equations per time step.

The corrector loops were adjusted during runtime of the later investigations to find stable and accurate settings. For three nAlphaCorr loops, the calculated

α values stayed within the natural limit of $0 \leq \alpha \leq 1$. The maximum mesh non-orthogonality was below 65° (orthogonal =0°) which made one nNonOrthogonalCorrectors loop sufficient to correct the non-orthogonality effects. Three nCorrectors loops were sufficient to reach a stable pressure - momentum coupling which produced a converging solution. Two nOuterCorrectors loops were applied since there were no differences in velocity and pressure field compared to solutions with more loops.

3.2 Modeling of Turbulence

The upstream flow situation of sharp-crested weir nappes with specific volume flow rates of 0.16 m^2/s and upstream water levels of ~1 m are in the fully turbulent regime with $Re = 2 \cdot 10^5$ based on the upstream water level. The length scales of turbulence structures range from geometric length scales down to Kolmogorov length scale calculated by

$$\eta = \left(\frac{\nu^3}{\epsilon}\right)^{1/4} \tag{3.8}$$

with ν the kinematic viscosity and ϵ the viscous dissipation which is estimated by

$$\epsilon \approx \frac{u^3}{l} \tag{3.9}$$

with u the velocity and l the length scale (half the water depth for a free surface flow) (Nakagawa et al., 1975). This results in $\eta \approx 0.1$ mm as the length scale of the smallest eddies.

Discretizing the upstream flow situations of such a nappes with a model domain sizes of about 1m x 1m x 3m by using cell edge lengths of the Kolmogorov length scale would lead to a numerical model with more than 10^{12} cells. This would exceed the available computational resources of the used High Performance Computing (HPC) system by far which has in total 21504 CPU's and 172 TB RAM. Hence, turbulence effects are modeled with different degrees of modeling depending on the applied approach. For modeling the turbulent dissipation range, a LES model is used, which is based on Kim and Menon (1995) which uses a dynamic

k-equation subgrid-scale model (SGS). The "dynamic" in the dynamic k-equation model refers to the dynamic procedure used to solve for the subgrid-scale kinetic energy. In this approach, the model estimates the dissipation rate of the subgrid-scale kinetic energy based on the resolved-scale kinetic energy and its dissipation rate. This feature is particularly useful in simulating flow scenarios characterized by non-uniform or unsteady conditions with turbulence structures generated and mixed at multiple locations, such as expected for the flow situation of nappes. For modeling a significantly larger part of the turbulence length scales and only calculate the large vortex structures a k-ω-SST model and an incompressible, but density variation considering version k-ω-SST$_\rho$ which are both based on Menter and Esch (2002); Menter et al. (2003) are used. The k-omega-SST turbulence model is an advanced variant of the Reynolds-Averaged Navier-Stokes turbulence models that excels in accurately modeling fluid turbulence in various flow situations. One of its main advantages over other RANS turbulence models is its ability to perform well in both near-wall and far-field turbulent flows. This particular attribute motivates the incorporation of the k-omega-SST turbulence model in the present study, as the dynamics of the flow involve turbulence development in the far-field region of the nappe in the upstream area, while turbulence generation is expected to occur at the weir crest. The time-considering variants of the turbulence models (URANS) are used here to directly calculate the large turbulent length scales of the transient flow situation.

The subgrid turbulent kinetic energy k_s for the LES model is calculated by

$$\frac{\partial(k_\mathrm{s})}{\partial t} + \nabla \cdot (\overline{\boldsymbol{U}} k_\mathrm{s}) = 2\nu_\mathrm{t} S \nabla \overline{\boldsymbol{U}} - \frac{c_\epsilon \sqrt{k_\mathrm{s}}}{\overline{\Delta}} + \nabla \cdot [(\nu + \nu_\mathrm{t}) \nabla k_\mathrm{s}], \tag{3.10}$$

where

$$\nu_\mathrm{t} = c_\mathrm{v} \sqrt{k_\mathrm{s}}\, \overline{\Delta} \tag{3.11}$$

with $\overline{\Delta}$ the grid scale filter. The values c_v and c_ϵ of the LES model are dynamically computed by using a mathematical identity between the turbulent kinetic energy respectively the dissipation rate resolved at the grid scale filter level $\overline{\Delta}$ and a test filter level $\hat{\Delta} = 2\overline{\Delta}$ (Kim and Menon, 1995).

The subgrid turbulent kinetic energy k_s for the URANS model is calculated by

$$\frac{\partial(\rho k_s)}{\partial t} + \nabla \cdot (\rho \overline{\boldsymbol{U}} k_s) = \rho \tilde{P}_{k_s} - \rho \beta^* \omega k_s + \nabla \cdot [\rho(\nu + \sigma_{k_s} \nu_t) \nabla k_s] \tag{3.12}$$

with

$$\tilde{P}_{k_s} = \min(2\nu_t \nabla \overline{\boldsymbol{U}} S, 10\beta^* \omega k_s) \tag{3.13}$$

for limiting the turbulent kinetic energy production where

$$\nu_t = \frac{a_1 k_s}{\max(a_1 \omega, S F_2)}. \tag{3.14}$$

By applying

$$F_2 = \tanh\left[\left[\max\left(\frac{2\sqrt{k_s}}{\beta^* \omega y}, \frac{500\nu}{y^2 \omega}\right)\right]^2\right] \tag{3.15}$$

a differentiation between a boundary layer and a free stream flow situation is made with y the wall distance.
The dissipation is calculated via the turbulent specific dissipation rate equation (Menter and Esch, 2002; Menter et al., 2003)

$$\frac{\partial(\rho\omega)}{\partial t} + \nabla \cdot (\rho \overline{\boldsymbol{U}} \omega) = \frac{\gamma \rho G}{\nu_t} - \beta \rho \omega^2 + (1 - F_1) \rho C D_{k_s \omega} + \nabla \cdot [\rho(\nu + \sigma_\omega \nu_t) \nabla \omega] \tag{3.16}$$

where again a distinction is made between a boundary layer flow situation close to the wall and a free stream flow situation depending on the distance to the wall by applying

$$F_1 = \tanh\left[\left[\min\left[\max\left(\frac{\sqrt{k_s}}{\beta^* \omega y}, \frac{500\nu}{y^2 \omega}\right), \frac{4\sigma_{\omega 2} k_s}{C D^+_{k_s \omega} y^2}\right]\right]^4\right] \tag{3.17}$$

where

$$C D^+_{k_s \omega} = \max\left(2\rho\sigma_{\omega 2} \frac{1}{\omega} \nabla k_s \nabla \omega, 10^{-10}\right). \tag{3.18}$$

The constants of the model are calculated as a blending via $\phi = \phi_1 F_1 + \phi_2 (1 - F_1)$ where the constants are given in table 3.1.
Not blended constants are $\beta^* = 0.09$ and $a_1 = 0.31$.

Table 3.1. Constants for k-ω-SST model are blended by $\phi = \phi_1 F_1 + \phi_2(1 - F_1)$.

σ_{k_s1}	σ_{k_s2}	$\sigma_{\omega1}$	$\sigma_{\omega2}$	β_1	β_2	γ_1	γ_2
0.85	1	0.5	0.856	0.075	0.0828	5/9	0.44

3.3 Modeling of Turbulent Scalar Flux Terms

Reynolds-averaging scalar transport equations for URANS like the α-transport equation generates additional turbulent scalar flux terms $\nabla \cdot (\overline{\boldsymbol{u}'\alpha'})$ which are neglected within the implementation of OpenFOAM® v2012 (Eq. 3.6). These terms refer to the transport of a quantity due to turbulent fluctuations in a flow field. Spatially filtering the transport equations for LES approaches would also result in turbulent scalar flux terms. However, these terms are ignored for LES simulations due to the explicit resolution of the large turbulent structures. These resolved structures inherently contribute to turbulent mixing effects, eliminating the need for an additional turbulent flux term. Nevertheless, in two URANS test cases, these terms are modeled to incorporate the turbulence transport of α at the water-air interface of the nappe. The full unsteady Reynolds-averaged α-transport equation is given by

$$\frac{\partial \overline{\alpha}}{\partial t} + \nabla \cdot (\overline{\boldsymbol{U}\alpha}) + \nabla \cdot (\overline{\boldsymbol{u}'\alpha'}) + \nabla \cdot (\overline{\alpha}(1 - \overline{\alpha})U_\mathrm{r}) = 0 \tag{3.19}$$

with the fourth term on the left hand side counteracting numerical diffusion. A gradient-diffusion hypothesis for modeling the turbulent scalar flux term (third term on LHS) was used by Thorenz and Grefenstein (2022) to model the impact of turbulence on the distribution of air in a stilling basin of a weir:

$$\overline{\boldsymbol{u}'\alpha'} = -D_\mathrm{t} \nabla \overline{\alpha} \tag{3.20}$$

where

$$D_\mathrm{t} = \frac{\nu_\mathrm{t}}{Sc_\mathrm{t}} \tag{3.21}$$

is the turbulent mass diffusivity and Sc_t the turbulent Schmidt number which is for hydraulic flow situations typically between 0.1 and 1 (Watanabe et al., 2005).

The resulting α-transport equation including the model for the turbulent scalar flux term is given by

$$\frac{\partial \overline{\alpha}}{\partial t} + \nabla \cdot (\overline{\boldsymbol{U}\alpha}) - \nabla \cdot (D_\mathrm{t} \nabla \overline{\alpha}) + \nabla \cdot (\overline{\alpha}(1 - \overline{\alpha}) U_\mathrm{r}) = 0. \tag{3.22}$$

This transport equation was implemented in an interFoam-based solver of OpenFOAM® v2012 with the turbulent Schmidt number $Sc_\mathrm{t} = 1$ and used here for the two test cases given in Table 3.2.

3.4 Preliminary Studies for Modeling Nappes

3.4.1 Velocity Field at the Water-Air Interface

Internal nappe turbulence interacts with the turbulence produced at the water-air interface. As shown in section 3.1 the Volume-of-Fluid method generates a continuous transition between water and not a sharp interface as is physically correct. Hence, the calculation of the interface velocity is investigated concerning the influence of the continuum surface force (CSF) for modeling surface tension, different gradient schemes, different divergence schemes and different mesh sizes. Fig. 3.2 shows the 2D model setup for investigating the velocity at the water-air interface. The flow direction is from left to right. Water with $U = 0.25$ m/s enters the domain via the inlet boundary patch and leaves the domain via the open boundary patches. The weir and the bottom of the model have a noslip boundary condition. The sides of the modeled domain (y-direction) have a slip boundary condition to avoid a boundary layer flow situation. The step in the middle (-0.05 m $\leq x \leq 0$ m) dams the water and generates the nappe with a spill height of about 0.07 m, with $Re = 4515$ based on spill height. For turbulence modeling the k-ω turbulence model is used. In order to prevent the nappe from attaching to the wall, there is an open boundary in the step through which air can enter the modeled domain. The domain is discretized with perfect orthogonal cells. The discretization is 2D with one cell in the depth direction.
Fig. 3.3 shows the resulting speed $U = \sqrt{u^2 + w^2}$ over z at $x = -0.0125$ m for different surface tensions (a), gradient schemes (b), divergence schemes (c) and

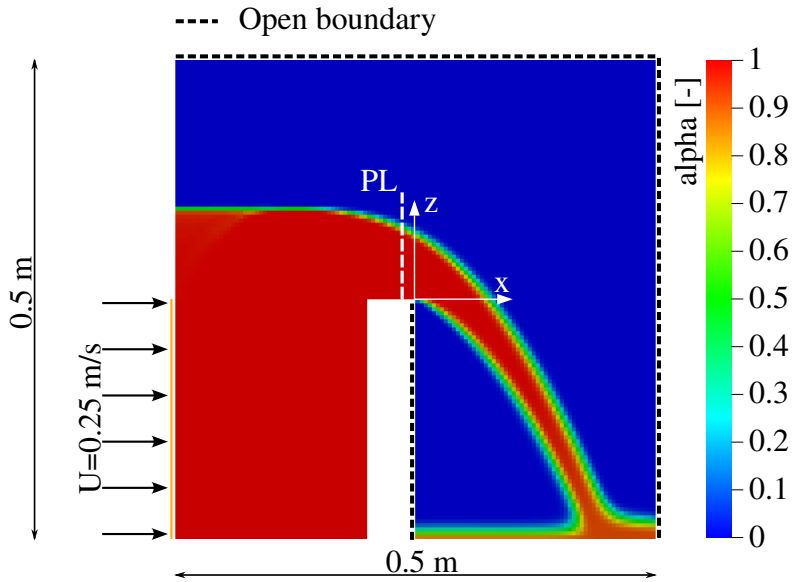

Fig. 3.2. 2D test case for investigating artificial velocities at the water-air interface. Flow from left to right. The vertical slice is colored by the water distribution of the Volume-of-Fluid-method (alpha).

mesh sizes (d). The red line marks the center of the water-air interface at which $\alpha = 0.5$ at $z = 0.067$ m. All plots show two velocity peaks. The lower peak at $z = 0.02$ m can be explained by the transformation of hydrostatic energy into kinetic energy as pressure inside the nappe equals ambient pressure. The upper peak at $z = 0.08$ m has an artificial origin as the upper part of the nappe is not accelerated by hydrostatic pressure transformation. The pressure here already equals ambient pressure. The artificial velocity results in false turbulence production at the water-air-interface. Several investigations on single bubble motion (e.g. Harvie et al., 2006) trace artificial interface velocities back to errors in the interface curvature calculation for the calculation of surface tension via the continuum surface force (CSF) model (Brackbill et al., 1992). However, Fig. 3.3a shows that the disabling of the surface tension force term of Eq. 3.3 has no influence on the formation of the artificial interface velocity.

Fig. 3.3b compares the formation of the artificial interface velocity for different gradient schemes which are given in OpenFOAM®-specific designations. The divergence theorem method (or Green-Gauss method) is called 'linear' and the least-squares minimisation is called 'leastSquares'. The leastSquares scheme cal-

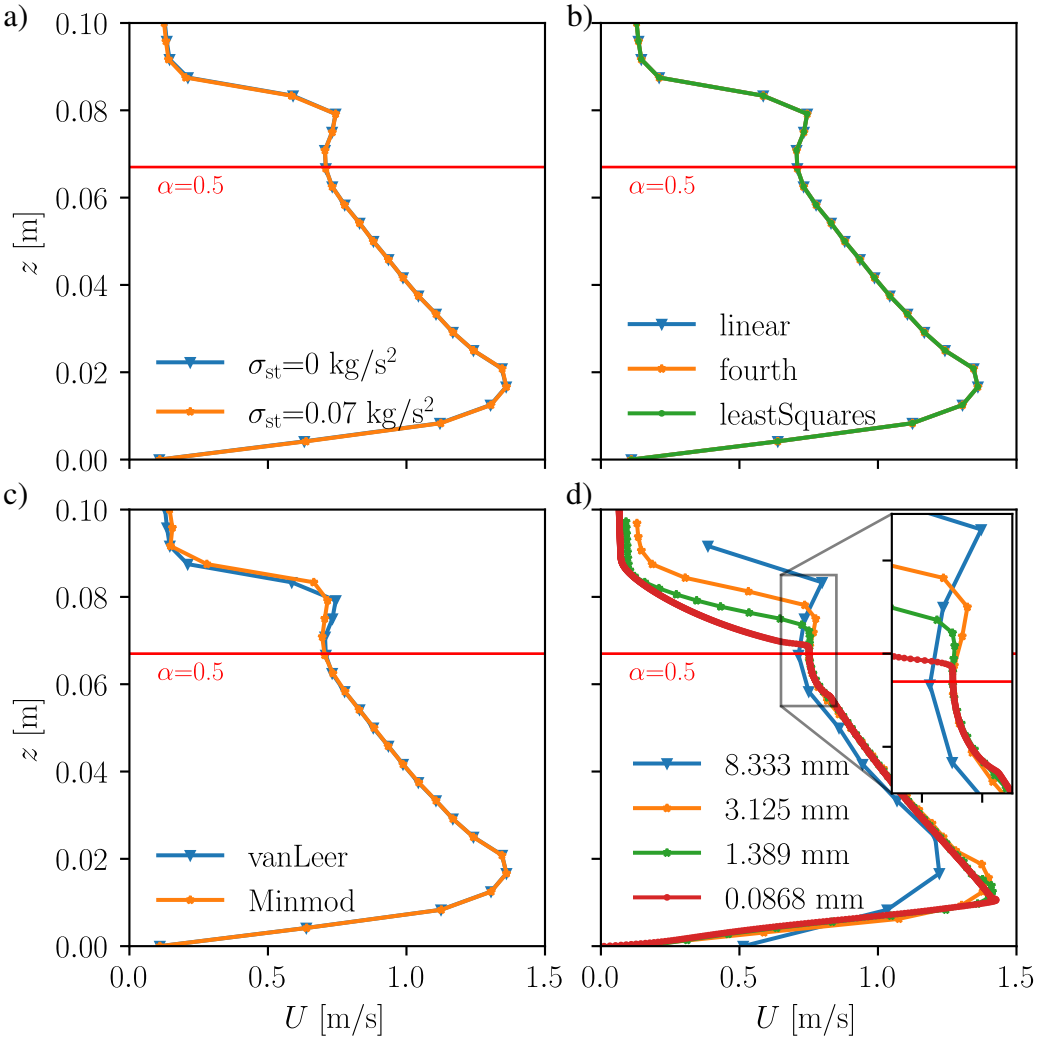

Fig. 3.3. Sensitivity analysis of velocity distribution to surface tension (σ_{st}) (a), gradient schemes (b), divergence schemes (c) and mesh size (d). The velocity is evaluated along z on PL shown in Fig. 3.2.

culates the gradients by extrapolating the cell value with a guessed cell gradient to the centroids of neighboring cells and minimises the squared difference between the extrapolated cell values and the actual cell values. This gives a second order function. The scheme 'fourth' is also available in OpenFOAM®, which in addition to the neighboring cell values also takes neighboring cell gradients into account and minimizes the squared differences. However, the gradient schemes show no influence on the formation of the artificial interface velocity and the 'linear' scheme

is used for all later investigations.

Fig. 3.3c compares two total variation diminishing (TVD) divergence schemes which have the property to monotonically decrease the total variation of the solution as the solution progresses in time and hence preserve spurious oscillations of the solution (Cox and Nishikawa, 1991). The vanLeer scheme is based on van Leer (1974) and the Minmod scheme is based on Harten (1983). The choice of the divergence scheme makes a slight difference in the shape of the artificial velocities. Still, those velocities exist for both investigated schemes. Since the two examined schemes do not show a significant difference in the generation of artificial velocity, the vanLeer scheme is used for all later investigations.

Fig. 3.3d compares the velocity distribution for different mesh sizes. The uniform cell-edge length of the hexahedral mesh is varied here. The upper and the lower peak are effected by the mesh size. The lower peak increases while the upper peak decreases with finer meshes.

The increase in the lower peak shows the cell size dependence of the transformation of hydrostatic pressure into kinetic energy. The velocity distribution at the lower peak is nearly the same for cell edge length 1.389 mm and 0.0868 mm, which shows that the solution reached convergence for a cell edge length of 1.389 mm. The upper peak shows a clear difference between the velocity distribution for cell edge length 1.389 mm and 0.0868 mm, not so much in the height of the peak but in its position in relation to the water-air interface ($\alpha = 0.5$) and the steepness of the velocity drop in the air phase which is initially steeper for the finer mesh (0.0868 mm) and later steeper for the coarser mesh (1.389 mm).

After the preceding investigations have already shown that the generation of artificial velocities at the interface can be effectively reduced by decreasing the mesh size, the influence of turbulence modeling on the velocity field at the water-air interface shall now also be examined. The objective of the investigations is to depict the acceleration of the nappe due to the pressure changes when flowing over the weir edge. Therefore, the focus is not primarily on directly capturing or modeling turbulent structures at the water-air interface. Fig. 3.4 shows the velocity profile of the nappe with a cell edge length of 0.0868 mm for two different URANS models (k-ω-SST and k-ω-SST$_\rho$) and for no turbulence model, which is not a Direct Numerical Simulation as the cell edge length is about 10 times larger

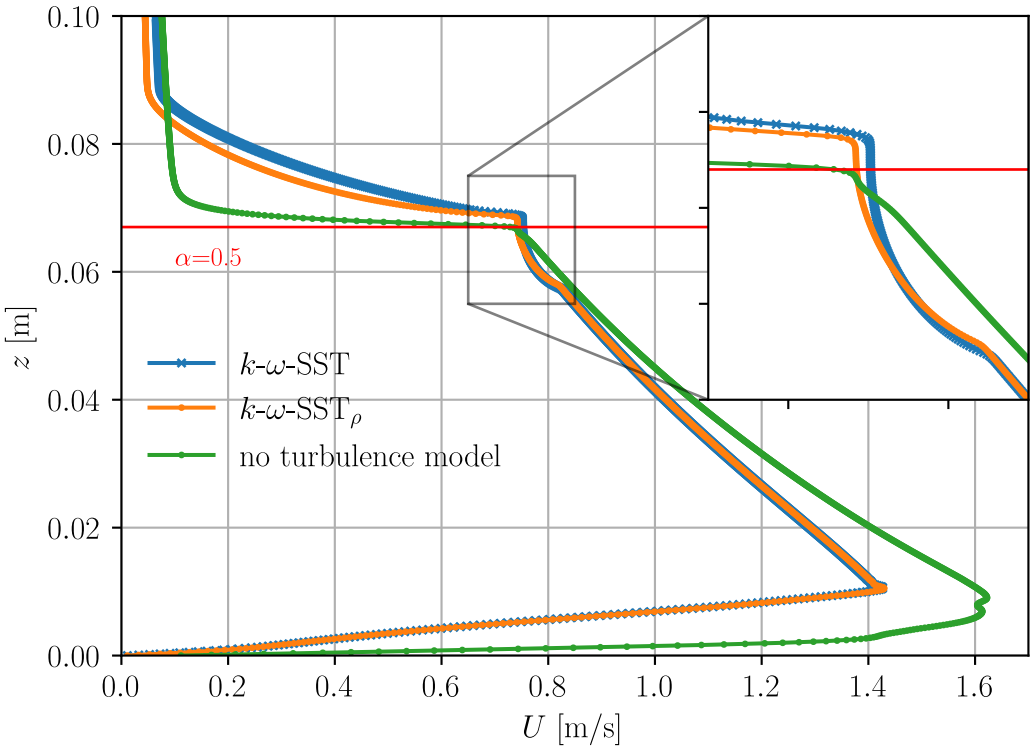

Fig. 3.4. Velocity profile of k-ω-SST, k-ω-SST$_\rho$ and for no turbulence model. 0.0868 mm cell edge length. The velocity is evaluated along z on PL shown in Fig. 3.2.

than the Kolmogorov length scale η (calculation in section 3.2).

The velocity profiles of the URANS models are identical for $z \leq 0.055$ m. At the water-air interface ($z = 0.67$ m) the computed velocity with the k-ω-SST model is sightly higher. The gradient of the velocity in the air phase is higher for the k-ω-SST$_\rho$ model. Both URANS models show an area of constant velocity at the water-air interface which is not seen when no turbulence model is used. Without turbulence model, the velocity gradient is constant in the water phase and significantly increases in the air phase, immediately at the water-air interface. The lower peaks velocity is higher when no turbulence model is used.

Due to the difference in kinematic viscosity μ between water and air and due to a continuous shear stress at the interface (as discussed in section 2.9) the velocity gradient in air has to be higher compared to the velocity gradient in water, as shown by the velocity profile when no turbulence model is used.

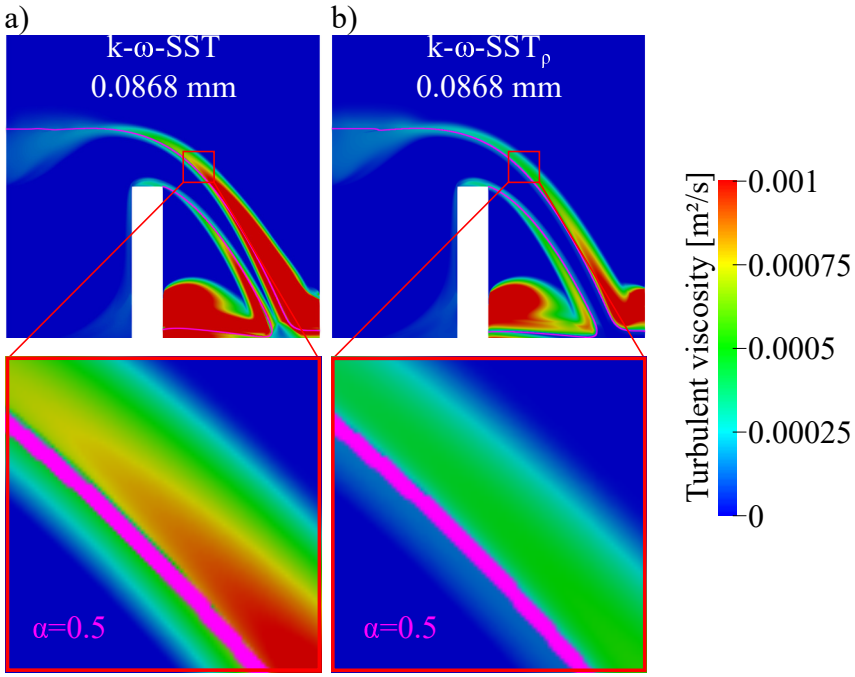

Fig. 3.5. Distribution of turbulent viscosity ν_t for k-ω-SST (a) and k-ω-SST$_\rho$ (b).

Fig. 3.5 shows the distribution of turbulent viscosity for the k-ω-SST model (a) and the k-ω-SST$_\rho$ model (b) for a cell edge length of 0.0868 mm. Both models show the main origin of turbulent viscosity ν_t in the air phase over the whole drop depth of the nappe, with higher values of ν_t for the k-ω-SST model. The distribution of ν_t for the k-ω-SST model is not effected by the water-air interface ($\alpha = 0.5$), whereas ν_t is lower for the k-ω-SST$_\rho$ model on the water side of the interface.

As described in section 3.2, the k-ω-SST model does not take variations in density ρ into account. Hence, subgrid turbulent kinetic energy k_s produced in the air phase can diffuse into the water phase unaffected by the phase change. The k-ω-SST$_\rho$ model takes density into account and hence reduces k_s that diffuses into the water phase due to the density gradient. This explains the lower values of ν_t in the water phase for the k-ω-SST$_\rho$ model. The reduction of ν_t in the water phase increases the gradient of k_s between the water and the air phase which increases the diffusion of k_s into the water phase. Therefore, the k-ω-SST$_\rho$ model tends to reduces k_s in the modeled domain when the main origin of k_s is in the air phase.

Turbulent viscosity at the water-air interface increases the momentum transport

which explains the constant velocity at the interface for the URANS models (seen in Fig. 3.4).

The refining of mesh size at the water-air interface is capable of reducing the artificial velocities. However, the necessary mesh size to avoid the development of artificial velocities ($\leq$ 1.386 mm, as shown in Fig. 3.3) cannot be provided for nappes of prototype scale. For this, the nappe surface would have to be heavily refined over the entire drop depth. The computational resources of the later investigations were limited to cell edge length of 3.125 mm at the water-air interface. Hence, if the water-air interface is underresolved, it will invariably result in inaccuracies in the simulation outcomes. These discrepancies can significantly affect the forecasted flow characteristics, encompassing turbulence intensity, velocity distributions, and surface attributes. Consequently, accurately predicting the effects of the water-air interface on the nappe surface is only partially feasible, and accounting for the impact of artificial velocities at the interface becomes imperative when scrutinizing the nappe behavior.

The velocity profiles for k-ω-SST, k-ω-SST$_\rho$ and no turbulence model are shown in Fig. 3.6 for a cell edge length of 3.125 mm. All three profiles show similar peak velocities at the upper and lower peak. The upper velocity peak and the drop in velocity are closer to the water-air interface when no turbulence model is used. Therefore, the generation of turbulence at the water-air interface will be influenced by the generation of artificial velocities for the later investigations independent of the turbulence model.

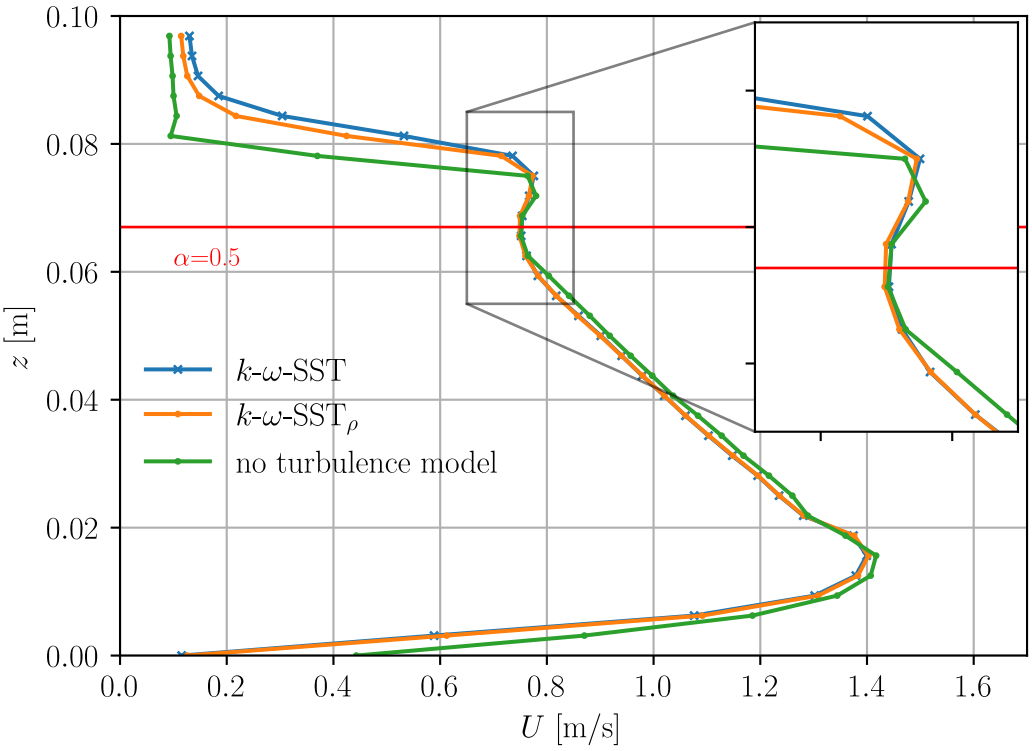

Fig. 3.6. Velocity profile of k-ω-SST, k-ω-SST$_\rho$ and for no turbulence model. 3.125 mm cell edge length. The velocity is evaluated along z on PL shown in Fig. 3.2.

3.4.2 Model Setup for Numerical Investigations of a Nappe

The dimensions of the numerical model setup as length and width of the upstream channel and the drop depth of the nappe are based on the experimental setup at the EDF laboratory at Chatou (Bercovitz et al., 2018). The nappe is modeled with spill heights of 0.17 m to 0.41 m, resulting in Reynolds numbers of $1.7 \cdot 10^5 \leq Re \leq 2.7 \cdot 10^5$ based on spill height. The examined volume flow rates are similar to those seen at the EDF setup at Chatou. Furthermore, volume flow rates higher than a unit discharges of 0.055 m^2/s ensures that investigations are far away from volume flow rates that are critical to nappe vibrations (Lodomez et al., 2019) which are not directly the subject of this thesis. The chosen nappe spill heights are also motivated by their relevance for fish downstream migration. A spill height of 0.17 m theoretically allows fish with body heights up to 8 cm to use the nappe as a

downstream migration channel (DWA, 2005) which already includes many local fish species.

Since the model setup has prototype scale there is no modeling issue due to Weber or Froude number. The model setup is shown in Fig. 3.7.

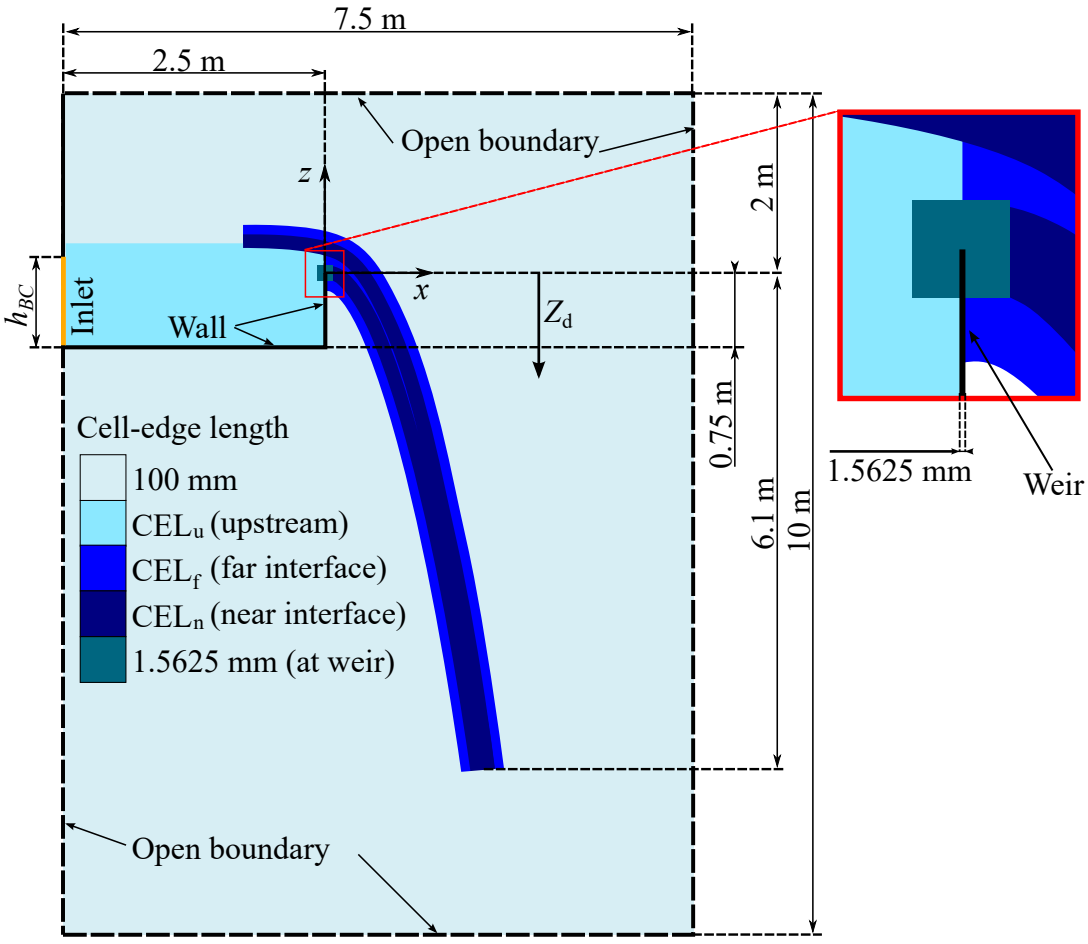

Fig. 3.7. Model domain and mesh sizes. Water enters the domain via the inlet on the left-hand-side and leaves the domain via the open boundary on the bottom. The nappe itself is resolved with variable mesh sizes with different cell-edge lengths (CEL_u, CEL_n, CEL_f) depending on the investigated case (see Table 3.2). At the weir crest, the resolution is 1.5625 mm. The Reynolds number over the weir crest based on the spill height is $1.7 \cdot 10^5 \leq Re \leq 2.7 \cdot 10^5$. The domain is 1 m deep with frictionless walls, respectively, a periodic boundary condition for Case 5.11-5.13.

The nappe with a drop depth of 6.1 m and a width of 1 m is fed by a 2.5 m long flume and starts at a 0.75 m high weir. The bottom of the flume and the

weir have a no-slip boundary condition. The sides of the modeled domain (in y-direction) have a slip boundary condition to avoid boundary layers, respectively, a periodic boundary condition (cyclicAMI) is used for cases with increased volume flow (Case 5.11-5.13) for coupling the boundary patches in the y-direction by an arbitrary mesh interface (AMI) interpolation. All other boundaries of the modeled domain (in x- and z-direction) are chosen to be open. Hence, the nappe is able to leave the modeled domain and air can enter the domain from x- and z-direction. The unstructured mesh refinement is octree-based and uses an α-iso-surface in order to refine the mesh around the water-air interface. The nappe was resolved with different mesh sizes around the nappe (CEL_f, CEL_n) as well as in the upstream part of the nappe (CEL_u) depending on the investigated case (see Table 3.2). At the weir crest the mesh was refined to 1.5625 mm cell-edge length. Depending on the investigated case, up to 60 million cells were used to discretize the domain.
The same mesh and solver settings were employed for both the LES and the URANS simulations. Consequently, differences in the results primarily stem from the chosen turbulence model. This investigation is conducted against the backdrop of previous studies where no influence of upstream turbulence on nappes was observed, and these investigations were based on URANS models. Therefore, the aim here is to examine whether the choice of turbulence model is causative. The calculation is performed with an adaptive time step size which is controlled by the maximum Courant-Friedrichs-Lewy-number of $C = 0.5$ within the model domain. For the given mesh and velocity distribution this results in a time step size in the range of $0.0001\ \text{s} \leq \Delta t \leq 0.0002\ \text{s}$. The time-averaging of the falling nappe was started after reaching a quasi-steady state. The averaging time was limited to 11 s due to the high computational time (after reaching quasi steady state of the upstream flow). An overview over the performed numerical investigations on this model setup is given in Table 3.2.

Table 3.2. Overview of numerical investigations. Q: Volume flow; BC: inlet boundary condition type as defined by Fig. 3.8, 3.9 in section 3.4.3; h_{BC}: inlet patch height; Turbulence model: dynamic k-eqn (LES) and k-ω-SST, k-ω-SST$_\rho$ (URANS); $k_{s_{in}}$: inlet subgrid turbulent kinetic energy; α-transport equation: Eq. 3.6 without turbulent scalar flux, Eq. 3.22 using a gradient-diffusion hypothesis for the flux; c_α, $c_{i\alpha}$: artificial compression coefficients of Eq. 3.7; CEL_u, CEL_n, CEL_f: mesh cell-edge lengths in specific areas defined by Fig. 3.7; Amp: the relative amplitude between low and high velocity areas of the inlet BC; I: the cross-sectionally averaged values of the turbulence intensity (see Eq. 3.23) 1 m upstream of the weir.

Case	Q [m^3/s]	BC	h_{BC} [m]	TM	$k_{s_{in}}$ [m^2/s^2]	α-eqn.	c_α	$c_{i\alpha}$	CEL_u [mm]	CEL_n [mm]	CEL_f [mm]	Amp [-]	I [%]
1	0.16	A	0.8	dyn k eq	0.0001	3.6	0.1	0.1	6.25	3.125	6.25	0.0	7.5
2	0.16	B	0.8	dyn k eq	0.0001	3.6	0.1	0.1	6.25	3.125	6.25	0.05	7.6
3	0.16	C	0.8	dyn k eq	0.0001	3.6	0.1	0.1	6.25	3.125	6.25	0.1	9.8
4	0.16	D	0.8	dyn k eq	0.0001	3.6	0.1	0.1	6.25	3.125	6.25	0.15	11.9
5	0.16	E	0.8	dyn k eq	0.0001	3.6	0.1	0.1	6.25	3.125	6.25	0.2	13.8
5.1	0.16	E	0.8	dyn k eq	0.0001	3.6	0.1	0.1	6.25	6.25	12.5	0.2	13.8
5.2	0.16	E	0.8	dyn k eq	0.0001	3.6	0.1	0.1	6.25	12.5	25	0.2	13.8
5.3	0.16	E	0.8	dyn k eq	0.0001	3.6	0.0	0.1	6.25	3.125	6.25	0.2	13.8
5.4	0.16	E	0.8	dyn k eq	0.0001	3.6	0.2	0.1	6.25	3.125	6.25	0.2	13.8
5.5	0.16	E	0.8	dyn k eq	0.0001	3.6	0.3	0.1	6.25	3.125	6.25	0.2	13.8
5.6	0.16	E	0.8	dyn k eq	0	3.6	0.1	0.1	50	100	100	0.2	8.6
5.7	0.16	E	0.8	dyn k eq	0	3.6	0.1	0.1	25	100	100	0.2	9.9
5.8	0.16	E	0.8	dyn k eq	0	3.6	0.1	0.1	12.5	100	100	0.2	11.0
5.9	0.16	E	0.8	dyn k eq	0	3.6	0.1	0.1	6.25	100	100	0.2	11.0
5.10	0.16	E	0.8	dyn k eq	0	3.6	0.1	0.1	3.125	100	100	0.2	11.0

Table 3.2. Overview of numerical investigations. Q: Volume flow; BC: inlet boundary condition type as defined by Fig. 3.8, 3.9 in section 3.4.3; h_{BC}: inlet patch height; Turbulence model: dynamic k-eqn (LES) and k-ω-SST, k-ω-SST$_\rho$ (URANS); $k_{s_{in}}$: inlet subgrid turbulent kinetic energy; α-transport equation: Eq. 3.6 without turbulent scalar flux, Eq. 3.22 using a gradient-diffusion hypothesis for the flux; c_α, $c_{i\alpha}$: artificial compression coefficients of Eq. 3.7; CEL_u, CEL_n, CEL_f: mesh cell-edge lengths in specific areas defined by Fig. 3.7; Amp: the relative amplitude between low and high velocity areas of the inlet BC; I: the cross-sectionally averaged values of the turbulence intensity (see Eq. 3.23) 1 m upstream of the weir.

Case	Q [m^3/s]	BC	h_{BC} [m]	TM	$k_{s_{in}}$ [m^2/s^2]	α-eqn.	c_α	$c_{i\alpha}$	CEL_u [mm]	CEL_n [mm]	CEL_f [mm]	Amp [-]	I [%]
5.11	0.16	E	0.8	dyn k eq	0.0001	3.6	0.1	0.1	6.25	6.25	6.25	0.2	13.8
5.12	0.48	J	1	dyn k eq	0.0001	3.6	0.1	0.1	6.25	6.25	6.25	0.2	14.2
5.13	0.64	K	1.07	dyn k eq	0.0001	3.6	0.1	0.1	6.25	6.25	6.25	0.2	14.3
6	0.16	F	0.8	dyn k eq	0.0001	3.6	0.1	0.1	6.25	3.125	6.25	0.25	15.9
7	0.16	G	0.8	dyn k eq	0.0001	3.6	0.1	0.1	6.25	3.125	6.25	0.3	17.8
8	0.16	H	0.8	dyn k eq	0.0001	3.6	0.1	0.1	6.25	3.125	6.25	0.35	19.7
8.1	0.16	H	0.8	k-ω-SST	0.0001	3.6	0.1	0.1	6.25	3.125	6.25	0.35	20.4
8.2	0.16	H	0.8	k-ω-SST	0.0001	3.22	0.1	0.1	6.25	3.125	6.25	0.35	20.4
8.3	0.16	H	0.8	k-ω-SST$_\rho$	0.0001	3.22	0.1	0.1	6.25	3.125	6.25	0.35	20.4

Preliminary Studies
Upstream mesh dependency (section 3.4.4)
Nappe mesh dependency (section 3.4.7)
Artificial compression term (section 3.4.8)
Main Investigations
Nappe widening for Q = 0.160 m^3/s
Nappe widening for increased Q (section 4.4)
RANS cases (section 4.3)

3.4.3 Upstream Turbulence Generation

In this work, the hypothesis is to be tested that upstream induced turbulence is one cause of the observed widening of nappes. In particular, the effect of large-scale turbulent structures is to be investigated, which necessitates the generation of such turbulent structures and not just the introduction of subgrid turbulent kinetic energy.

Real weirs are fed by channel flows with integral length scales likely approaching the water depth as in developed and uniform channel flows (Nakagawa et al., 1975). Here, a setup was closer to the laboratory facility as in Fig. 1.2 with relatively short feeding tank where the flow is not a developed channel flow. Thus, rather than attempt to simulate developed channel turbulence with a high computational cost, inlet conditions with different turbulence intensities were simulated artificially, freeing the computational resources for the nappe. Yet, care was taken to choose a method which generates large-scale structures at the inlet of the upstream feeding tank, not just a random field, and that with different turbulence intensities, with the aim of promoting the development of turbulent structures akin to those encountered in natural river flows. To this end, an in-house development of The Federal Waterways Engineering and Research Institute (Bundesanstalt für Wasserbau) was used as follows: The inlet velocity field is determined in such a way that a specified flow rate is achieved. In addition, a fluctuation and an inflow angle can be added to the velocity field. A swirl can also be added but not used here since the inlet flow situation is assumed to be free of swirl. The velocity distribution of the inlet patch has a pie-piece shape which rotates around the center of the patch. The number of these rotors and the rotation speed can be changed. This setup can generate large-scale flow structures which disintegrate into turbulence. In order to create structures that are of the desired size, the inlet patch consists of four rotating velocity fields. Rotation speeds of 8 to 11 1/min (different rotation speed for every inlet patch) were chosen and the number of blades per patch was set to one. No propeller swirl was applied. The total volume flow ranges between $0.16\ \mathrm{m}^3/\mathrm{s} \leq Q \leq 0.64\ \mathrm{m}^3/\mathrm{s}$. The resulting turbulence intensity I one meter upstream of the weir is varied via the amplitude which determines the ratio between high and low velocity areas.

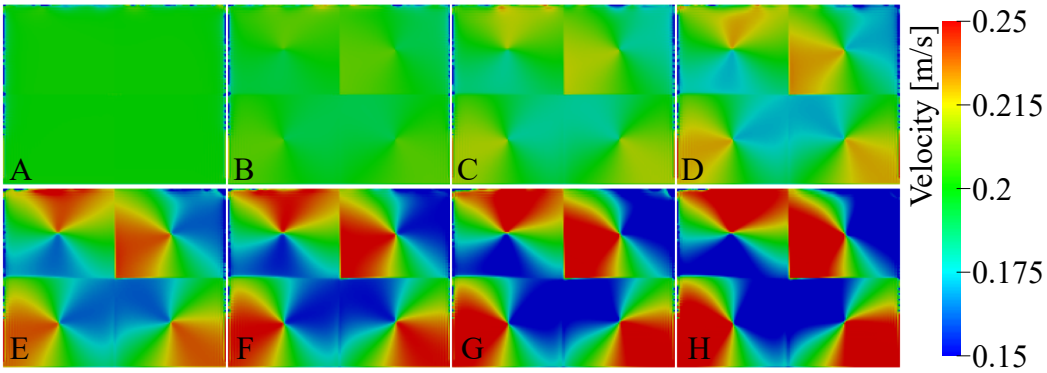

Fig. 3.8. Snapshot of the inlet boundary conditions (BC) for generating velocity distributions at a given instant in time. The inlet patch consists of four individually rotating velocity fields. The resulting turbulence intensity I downstream (see Eq. 3.23) is varied by the amplitude which determines the ratio of velocity between high and low velocity areas. The flow rate is kept constant.

Fig. 3.8 shows the inlet velocity fields for the generation of eight different turbulence settings, at a given instant in time.

The resulting turbulence intensity I is calculated as an average over the cross-sectional area of the channel one meter upstream of the weir,

$$I = \left\langle \frac{\sqrt{\overline{u_i'^2}} + \sqrt{\frac{2}{3}k_s}}{\sqrt{\overline{U_i^2}}} \right\rangle_{(i=1,2,3)} \tag{3.23}$$

where k_s is the subgrid turbulent kinetic energy. Table 3.2 lists the resulting values of I ranging $7.5 \leq I \leq 20.4$ %. The resulting I are of the same magnitude as those of Castillo et al. (2014) with 1 % to 15 % 0.5 m upstream of the weir and Muralha et al. (2020) with 1 % to 15 % 0.62 m upstream of the backward facing step which produces the investigated free jet. Both introduce turbulence intensity I by a boundary condition which specifies the subgrid turbulent kinetic energy k_s at the inlet, but not velocity variations. This is different from the method used here, where velocity differences lead to the generation of turbulence.

As part of the investigation, the influence of upstream turbulence with increasing volume flow rates is also examined. Fig. 3.9 shows the inlet velocity fields for generating volume flow rates of $0.16\ \mathrm{m^3/s} \leq Q \leq 0.64\ \mathrm{m^3/s}$ with similar I. The

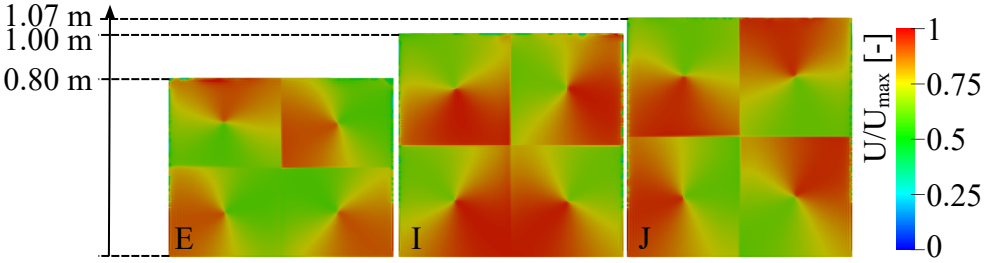

Fig. 3.9. Snapshot of the inlet boundary conditions for different volume flow rates with similar I at a given instant in time. Inlet patch height is adapted to volume flow rate (see Table 3.2). $U_{\mathrm{max,E}} = 0.27$ m/s, $U_{\mathrm{max,I}} = 0.6$ m/s and $U_{\mathrm{max,J}} = 0.76$ m/s.

patch size is adapted to the head water level for creating turbulent structures of the desired size. By doing so, the inflow velocities increase with increasing volume flows. Hence the rotation speed of the inlet patches is increased proportionally. The amplitude of the boundary condition which determines the ratio of high to low velocities on the inlet patches is constant for all setups.

3.4.4 Mesh Independence of Upstream Turbulence Transport

Cases 5.6-5.10 which differ in mesh cell-edge length in the channel $\mathrm{CEL_u}$ (see Table 3.2) are investigated for determine a proper mesh size for the turbulence development and transport in the upstream channel for LES simulations. For these investigations, the inlet subgrid turbulent kinetic energy $k_{\mathrm{s_{in}}}$ is chosen to be zero since the mesh dependency of the directly simulated turbulence, introduced by the boundary condition, is of interest. For finer cell edge length it is expected that directly simulated turbulent kinetic energy $k = 1/2\left(\overline{(u')^2} + \overline{(v')^2} + \overline{(w')^2}\right)$ increases and subgrid turbulent kinetic energy k_{s} decreases. Inlet subgrid turbulent kinetic energy $k_{\mathrm{s_{in}}}$ would therefore falsify the evaluation of the mesh dependency. The evaluation is based on turbulence intensity I (calculated according to Eq. 3.23) and I_{d}, which is the directly simulated part of I:

$$I_{\mathrm{d}} = \left\langle \frac{\sqrt{\overline{u_i'^2}}}{\sqrt{\overline{U_i^2}}} \right\rangle_{(\mathrm{i=1,2,3})}, \tag{3.24}$$

both evaluated 1 m upstream of the weir.

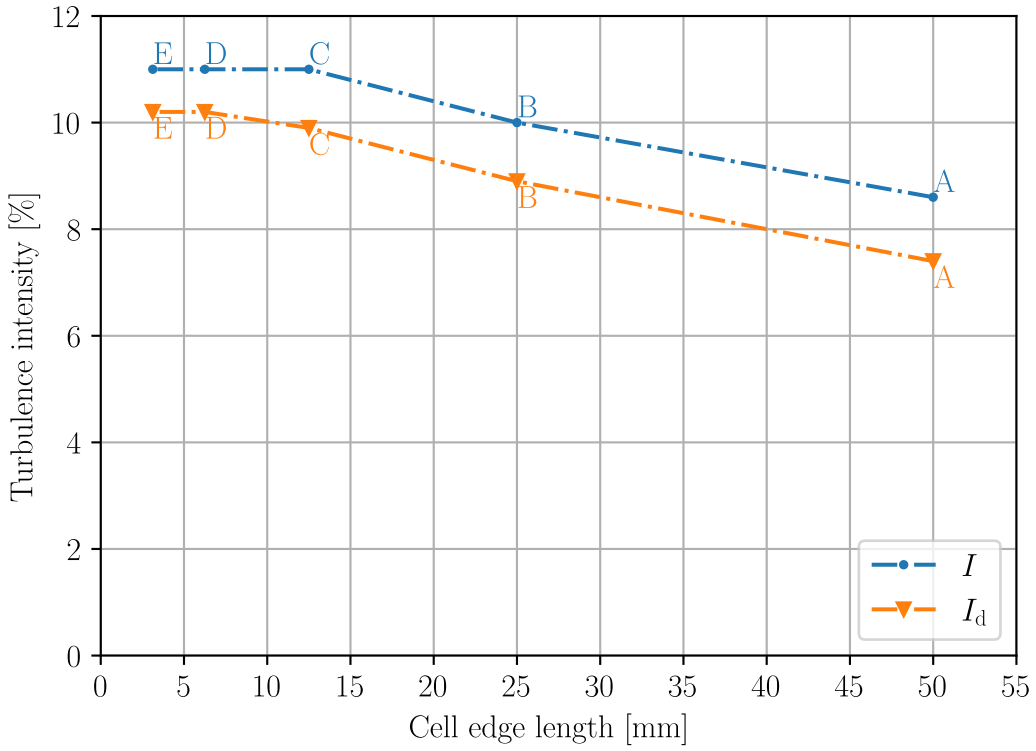

Fig. 3.10. Mesh independence study of upstream turbulence transport for different cell edge lengths in the upstream channel (CEL_u). Comparing Case 5.6 (A), Case 5.7 (B), Case 5.8 (C), Case 5.9 (D) and Case 5.10 (E) (see Table 3.2).

Fig. 3.10 shows the directly simulated part of the turbulence intensity (I_d) as well as the total turbulence intensity (I) as a function of the upstream cell edge length (CEL_u). The investigated cell edge lengths range 3.125 mm $\leq CEL_u \leq$ 50 mm. I and I_d increase linearly with smaller upstream cell edge lengths. For $CEL_u < 12.5$ mm no further increase in I is observed. I_d shows no further increase for $CEL_u < 6.25$ mm.

The mesh independence study shows that the turbulence intensity I and the directly simulated turbulence intensity I_d are converged for $CEL_u < 12.5$ mm with 93 % of the turbulent kinetic energy being directly simulated, calculated by I_{d_D}/I_E. Hence, the mesh of Case 5.6 (D) with $CEL_u = 6.25$ mm, resulting in ~12.7 Mio. cells, is used as the upstream mesh for later investigations.

3.4.5 Development of Upstream Turbulence

The model setup shown in Fig. 3.7 is investigated for the flow situation of Case 5 (see Table 3.2) concerning the development of the upstream velocity field and turbulence characteristics along the channel. Case 5 is examined because the turbulent intensity of this case (I = 13.8 %) is in the middle range of the examined turbulent intensities.

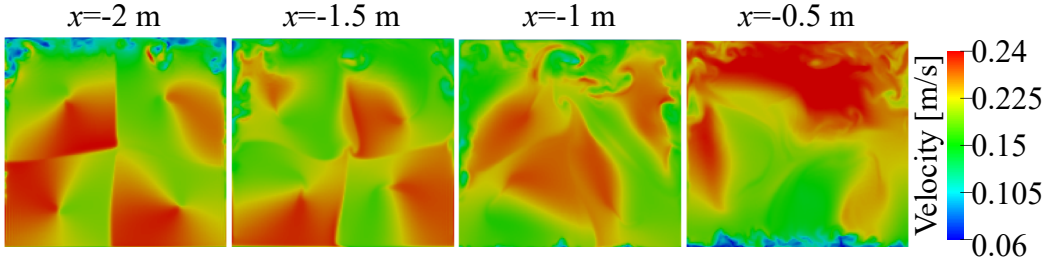

Fig. 3.11. Snapshots of the instantaneously water phase velocity upstream of the weir of Case 5 (see Table 3.2) for $x = -2$ m, -1.5 m, -1 m and -0.5 m at a given instant in time.

Fig. 3.11 shows snapshots of the upstream velocity field on vertical slices through the channel (yz-plane) for different x-positions of Case 5 (see Table 3.2). For $x = -2$ m the velocity field is clearly dominated by the inlet boundary condition (compare Fig. 3.8) which is located at $x = -2.5$ m. The more the flow approaches the weir (which is located at $x = 0$ m) the lower is the recognition of the boundary condition. At $x = -1$ m there are still areas of high velocity which are reminiscent of the inlet boundary condition, however, the shape of the velocity field is distorted and constantly changes over time. At $x = -0.5$ m separated velocity fields no longer appear. The strong deflection of the flow at the weir results in strong acceleration of the flow in the upper part. In contrast, the flow at the bottom of the channel is slowed down.

The turbulence characteristics are evaluated at P1-7 (see Fig. 3.12). For this purpose, the velocity profile in the y-direction (spacing of 6.25 mm) is recorded over 120 s with a frequency of 2208 Hz.

Fig. 3.13a shows u and $\overline{u}$ and Fig. 3.13b shows the distribution of the velocity fluctuations u' for P3. Beside short-term fluctuations of u, Fig. 3.13a shows long-term fluctuations which are quantified by Fig. 3.13c. In particular, two frequency

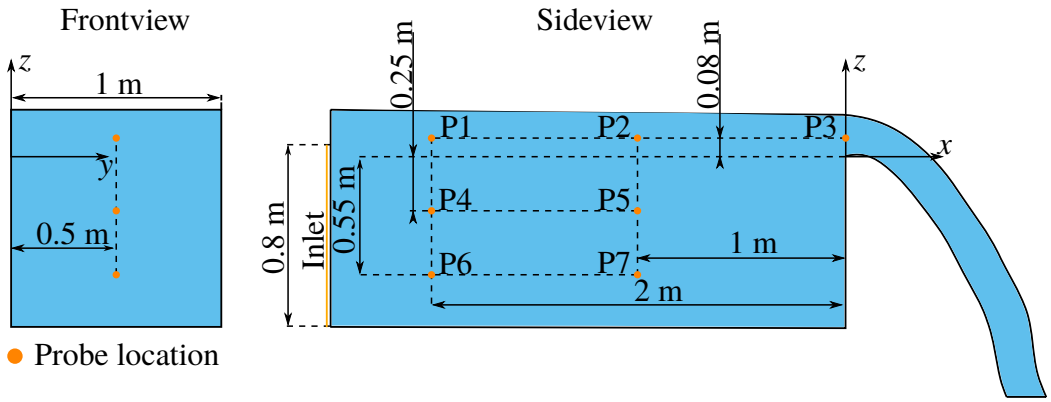

Fig. 3.12. Location of probes in numerical model. At every probe the velocity profile in y-direction (spacing 6.25 mm) is recorded for 120 s with a frequency of 2208 Hz.

peaks and one frequency range are distinguished here. A: $1.65 \cdot 10^{-2}$ Hz, B: $1.65 \cdot 10^{-1}$ Hz and $3 \cdot 10^{-1}$ Hz $\leq$ C $\leq 9 \cdot 10^{-1}$ Hz. A and B are both linked to the rotation frequency variation of the inlet boundary condition (see section 3.4.3) where B is the rotation frequency of each individual inlet patch (10 1/min) and A is the difference in the rotation frequency between the individual inlet patches (1-3 1/min), resulting in similar inflow situations every $\sim$ 60 s. The frequency range of C can be related to the sloshing frequency of the channel which is $f = 0.62$ Hz according to

$$f = \frac{\sqrt{gH}}{2L} \tag{3.25}$$

with g the gravitational acceleration, H the water level and L the tank length.

Fig. 3.14a,b show the water distribution α (a) and the time-averaged velocity $\overline{U}$ on a vertical slice at the center of the flume at $y = 0.5$ m. Streamlines of the time-averaged velocity field (S1,S2,S3) are included which run through P2,P5,P7. The development of turbulence is investigated in the following using the measuring points that are close to the same streamlines, where P1,2 are close to S1, P3,4,5 are close to S2 and P6,7 are close to S3.

Following Taylor's hypothesis of 'frozen turbulence' for flows with small turbulence intensity (here $I_d = 10.2$ % calculated by Eq. 3.24 at $x = -1$ m), stating that vortex structures do not change during the advection process and time series

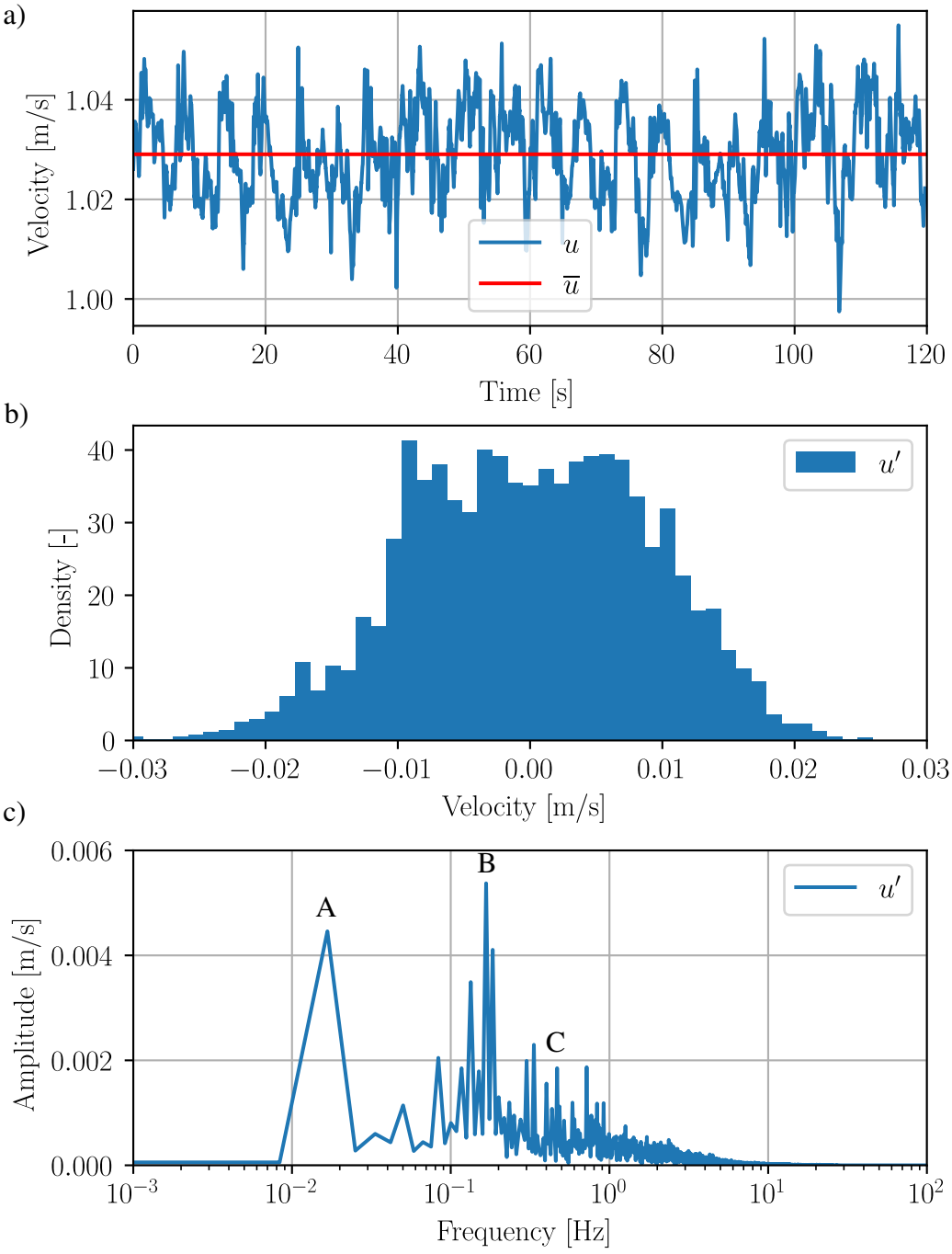

Fig. 3.13. Velocity data at P3 (Fig. 3.12). Velocity in x-direction u and average velocity in x-direction $\overline{u}$ (a), distribution of velocity fluctuations u' (b) and a fast Fourier transform of the velocity fluctuations u' (c).

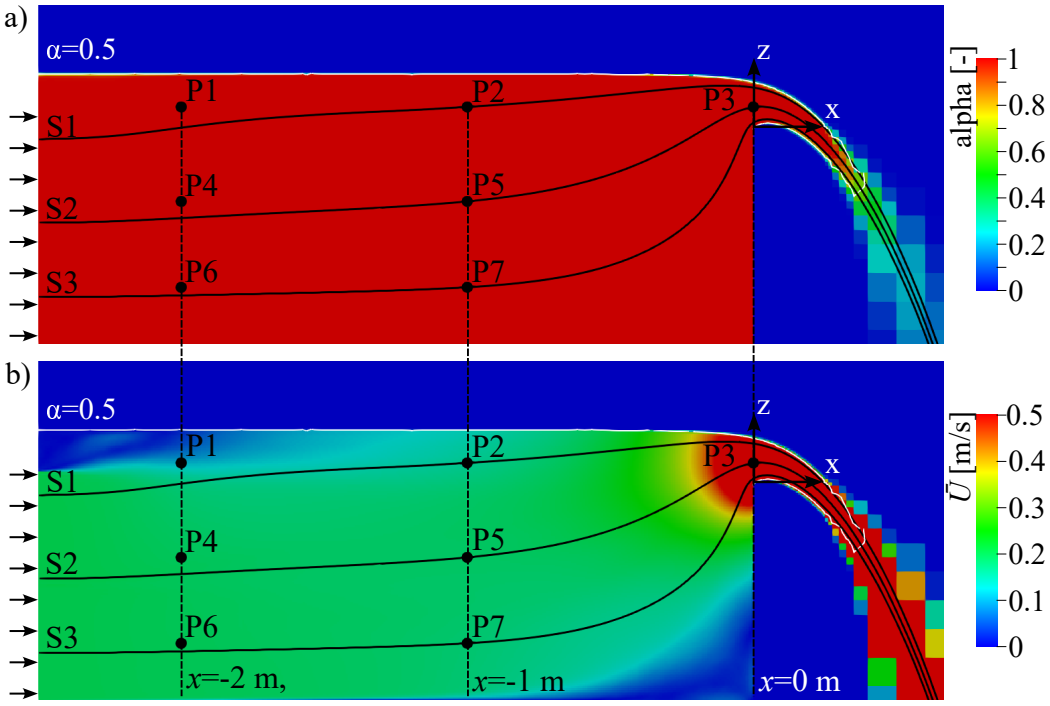

Fig. 3.14. α-distribution (a) and time-averaged velocity (b) on a central slice y = 0.5 m with three streamlines (S1,S2,S3) of the time-averaged velocity field running through P2, P5 and P7.

measured at a fixed point can be interpreted as spatial variations (Taylor, 1938), integral time scales and integral length scales are calculated concerning the first zero crossing of the correlation functions (shown in Figs. 3.15 - 3.17).

Figs. 3.15 - 3.17 show autocorrelations of P1-7 (see Fig. 3.12) where P1,2 are near the water surface, P3 is above the weir, P4,5 are at the center height of the flume and P6,7 are at the bottom of the flume. The integral time scales of P1-7 range 0.59 s $\leq T_{i_i} \leq$ 0.85 s. The integral length scales, however, range 0.08 m $\leq L_{i_i} \leq$ 0.7 m. It is very noticeable here that the integral length scale increases significantly for P3 at the weir with L_{i_3} = 0.7 m. This shows that the vortex structures experience a strong elongation while approaching the weir.

The correlation functions shown in Figs. 3.15 - 3.17 also show periodic behavior with a period length of $P \approx$ 6 s for P1,3,4,5, $P \approx$ 5 s for P2 and $P \approx$ 7 s for P6,7 which is defined by the lag of the first maximum of the correlation function in positive regime. The period lengths fit the rotation frequency of the inlet

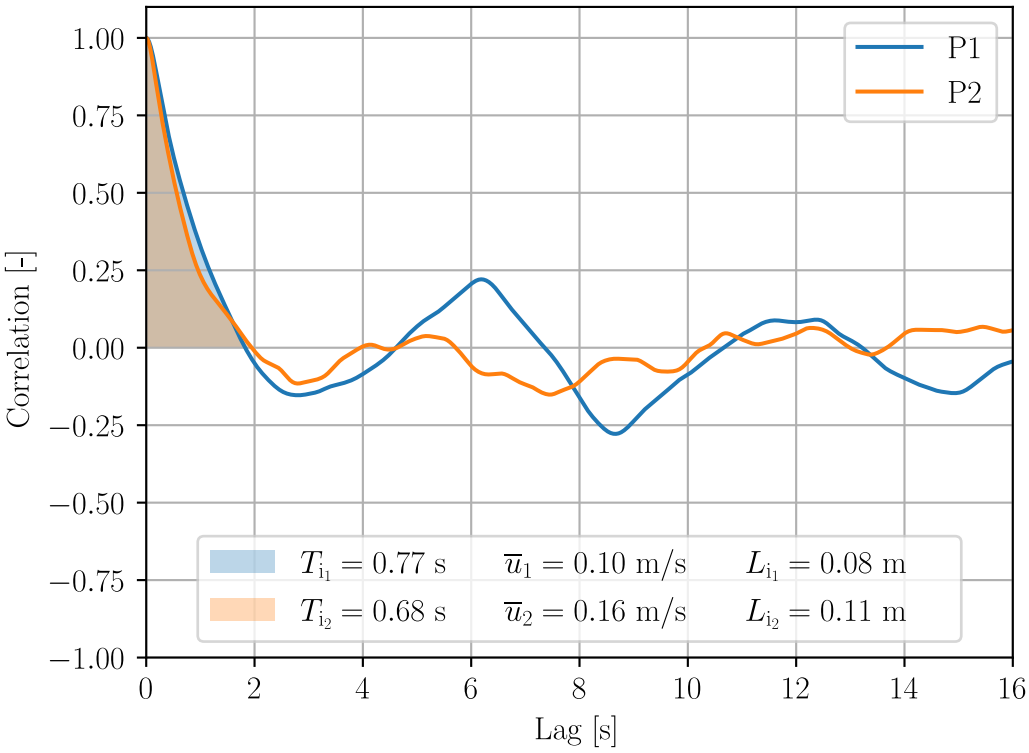

Fig. 3.15. Autocorrelation for P1,2 (see Fig. 3.12). The integral time scale T_i is calculated with the first zero crossing. The integral length scale L_i is calculated with the average velocity in x-direction $\overline{u}_i$.

boundary condition which is about 10 1/min. This reveals for an average velocity of $\overline{u}_3 = 1.03$ m/s vortex structures of ~ 6 m at the weir in main flow direction (x-direction).

Table 3.3. P_i/L_{i_i} for P1-7.

	$x = -2$ m	$x = -1$ m	$x = 0$ m
S1:	P1: 75 s/m	P2: 45.5 s/m	
S2:	P4: 54.5 s/m	P5: 50 s/m	P3: 8.5 s/m
S3:	P6: 46.6 s/m	P7: 46.6 s/m	

Table 3.3 gives the ratio of P_i/L_{i_i} for P1-7. The ratio is not constant, as could be supposed for flows with vortex structures decaying into multiple, but smaller structures over time. Rather, the ratio decreases continuously along the streamlines with increasing length of the vortex structures. This shows that the acceleration

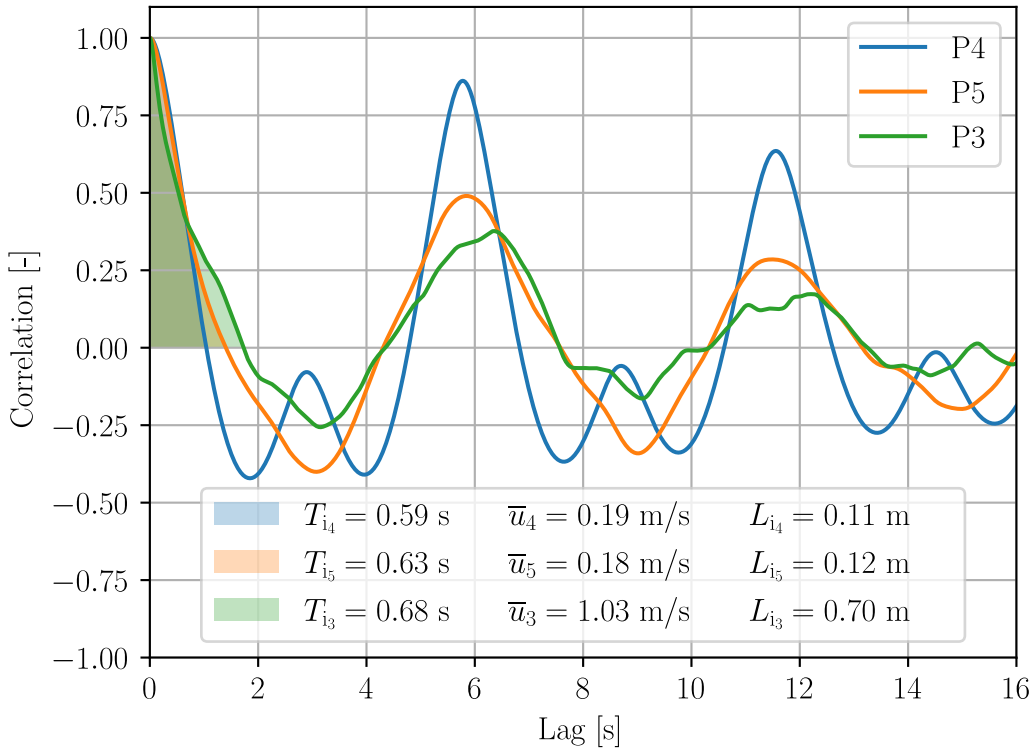

Fig. 3.16. Autocorrelation for P3,4,5 (see Fig. 3.12). The integral time scale T_i is calculated with the first zero crossing. The integral length scale L_i is calculated with the average velocity in x-direction $\overline{u}_i$.

of the flow along the streamlines elongates the large vortex structures without splitting them into individual pieces.

The intensity of the periodicity is defined by the correlation value after a lag of the period length P and given in table 3.4.

Table 3.4. Intensity of periodicity along streamlines S1, S2, S3.

	$x = -2$ m	$x = -1$ m	$x = 0$ m
S1:	P1: 0.22	P2: 0.04	
S2:	P4: 0.87	P5: 0.5	P3: 0.38
S3:	P6: 0.82	P7: 0.75	

The intensity of the periodicity decreases along S1, S2 and S3 which shows that the vortex structures have less similarity as they get closer to the weir. Along S1 the periodic intensity is much lower than for S2 and S3 and reduces from 0.22

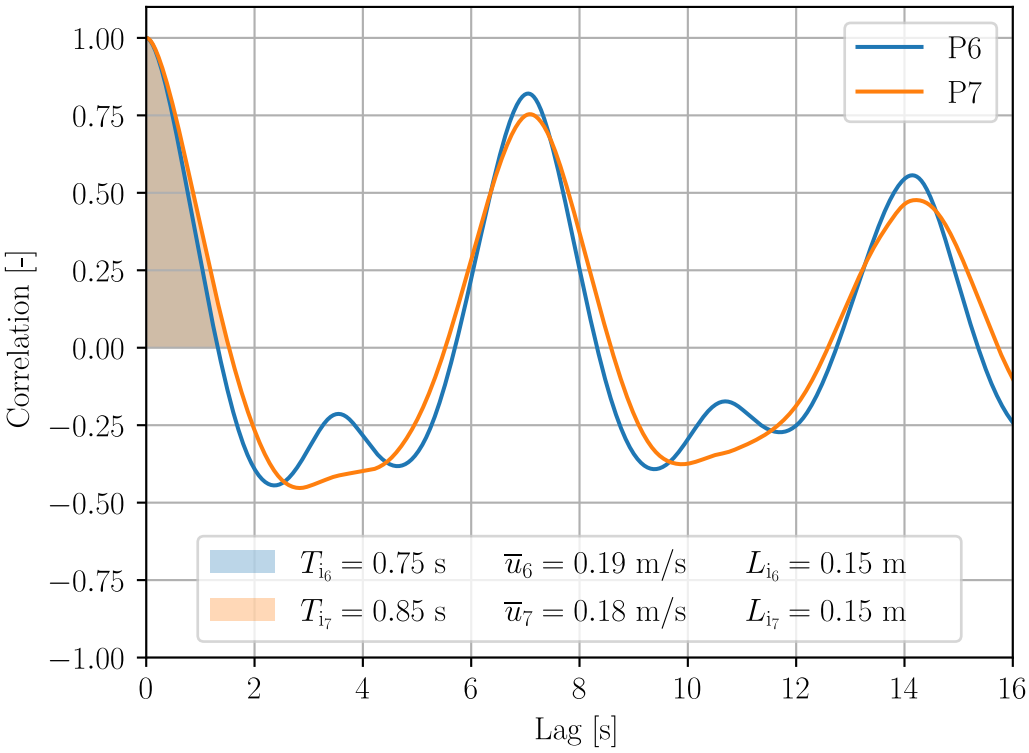

Fig. 3.17. Autocorrelation for P6,7 (see Fig. 3.12). The integral time scale T_i is calculated with the first zero crossing. The integral length scale L_i is calculated with the average velocity in x-direction $\overline{u}_i$.

at $x = -2$ m to 0.04 at $x = -1$ m. Fig. 3.14b shows that P1 and P2 are close to the edge of the inlet boundary. Therefore, the flow situation is dominated by turbulence generation at the edge of the entering water jet and less effected by the periodicity of the inlet boundary condition.

Figs. 3.18 - 3.20 show spatial autocorrelations of P1-7 (see Fig. 3.12) in the y-direction for v'. The integral length scale is calculated concerning the first zero crossing of the spatial autocorrelation function. For P1 the integral length scale is $L_{i_1} = 0.07$ m and at P2 the integral length scale is $L_{i_2} = 0.08$ m. Following the streamline S2 (see Fig. 3.14a,b) in Fig. 3.19, the integral length scale increases from $L_{i_4} = 0.06$ m at $x = -2$ m to $L_{i_5} = 0.1$ m at $x = -1$ m and then decreases again to $L_{i_3} = 0.05$ m at the weir crest ($x = 0$ m). P3 shows periodicity with a period length of ~ 0.1 m with small intensity of about -25 %. For P6 the integral length scale is $L_{i_6} = 0.06$ m which increases by following the streamline S3 to P7

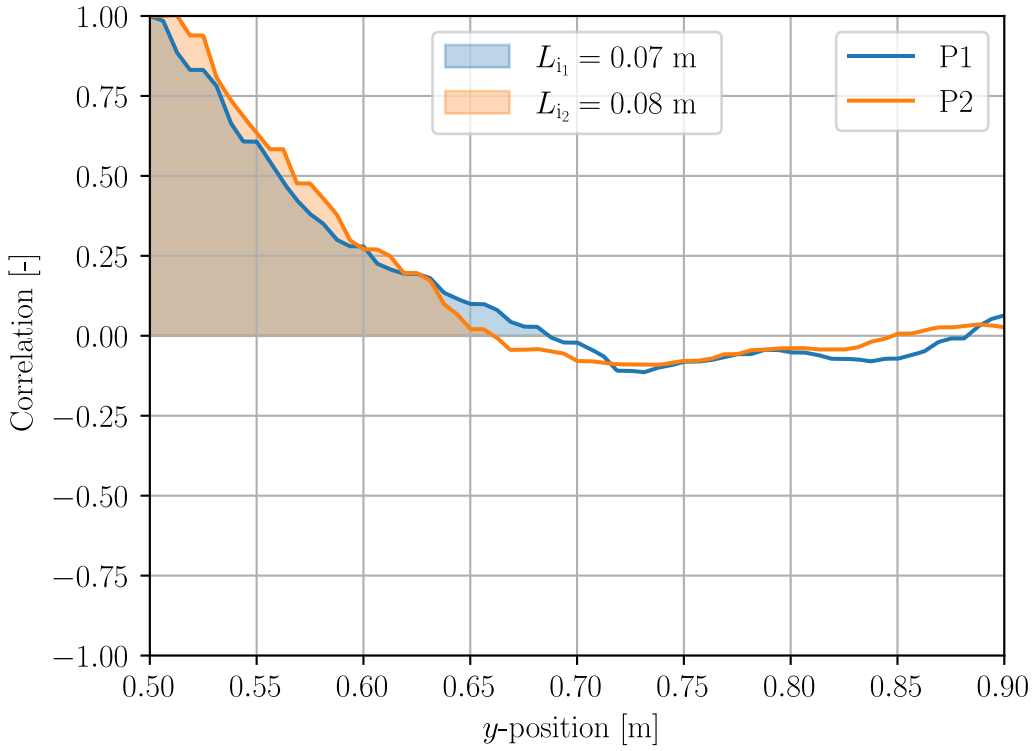

Fig. 3.18. Spatial autocorrelation in y-direction for P1,2 (see Fig. 3.12). The integral length scale L_i is calculated with the first zero crossing.

at which the integral length scale is $L_{i_7} = 0.08$ m.

P4 and P6 show high correlation at $y \sim 0.75$ m.

Fig.3.21 shows the inlet boundary patch with the four rotors. As described in section 3.4.3, the velocity fields rotate around the center of the patches. The rotation direction is the same for all patches, but the rotation velocity is different to increase the complexity of the upstream flow situation.

The seen high correlation for P4 and P6 at $y \sim 0.75$ m is explained by their proximity to the inlet boundary, albeit the reason cannot be given in absolute terms since the velocity fields of the inlet patches overlap at $x = -2$ m where P1,4,6 are located.

P1 does not show such a high correlation, albeit the x-distance to the inlet patch is the same. Fig. 3.12 and Fig. 3.21 show that P1 is located at the edge of the inlet patch and therefore not influenced by the rotating velocity field of the inlet boundary.

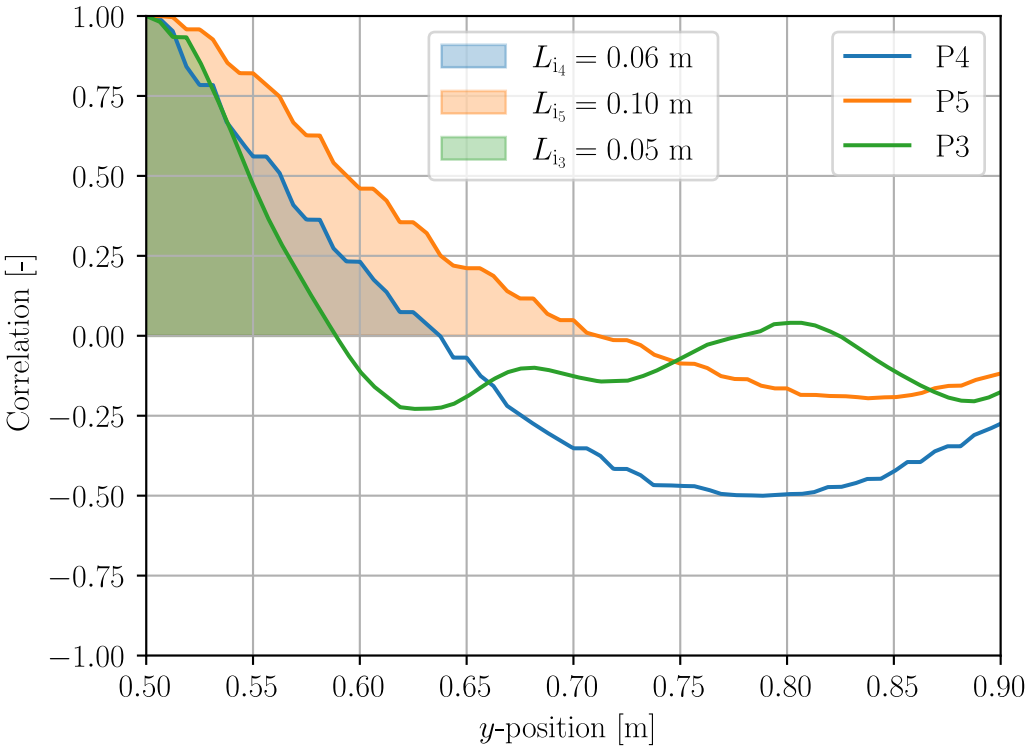

Fig. 3.19. Spatial autocorrelation in y-direction for P3,4,5 (see Fig. 3.12). The integral length scale L_i is calculated with the first zero crossing.

P3 shows a period length of about 10 cm, which fits the observations of later investigations shown in section 4.3.

Fig. 3.22 shows the power spectrum density (PSD) of the time series of u', v' and w' at P3. The PSDs of all three velocity fluctuations start to decrease at 0.5 Hz, following nearly the same curvature up to 7 Hz. Here, the curvature changes towards the -3 slope of the dissipation range. At $f = 20$ Hz, the PSDs slightly increase and then drop.

The first part of the PSD (up to 7 Hz) has its origin in the large scale turbulence structures generated by the inlet boundary condition which disintegrate into smaller structures (see integral length scales along streamline S2) (Fig. 3.19). These structures are superimposed by boundary layer turbulence which is generated at the edge of the inlet boundary (along streamline S1) and at the bottom of the flume. The drop in the PSD shows that the inertial range of turbulence is missing and the turbulent flow has not yet fully developed.

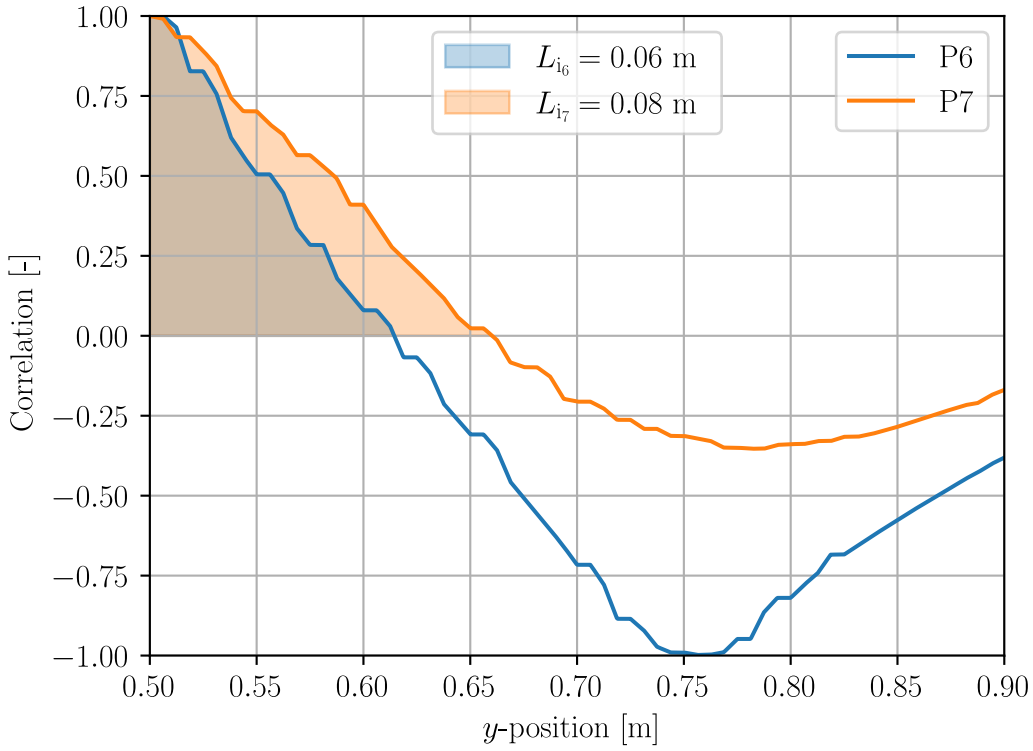

Fig. 3.20. Spatial autocorrelation in y-direction for P3,6,7 (see Fig. 3.12). The integral length scale L_i is calculated with the first zero crossing.

In summary, it can be said that the boundary condition generates vortex structures with integral length scales of about $L_i \approx 0.1$ m which reduce down to $L_i \approx 0.05$ m at the weir where they experience a significant elongation in the x-direction due to the acceleration. The flow at the weir is still influenced by the boundary condition in terms of periodicity.

3.4.6 Evaluation Method for Nappe Widening

To evaluate the nappe widening, an evaluation method was chosen which is independent of a water-air interface definition using α. For a given y-position, the standard deviation σ is calculated in the following manner, with the subscript i the cell index,

$$\sigma = \sqrt{\frac{\sum_i (\overline{\alpha_i} A_i (x_i - x_{CG})^2)}{\sum_i (\overline{\alpha_i} A_i)}} \tag{3.26}$$

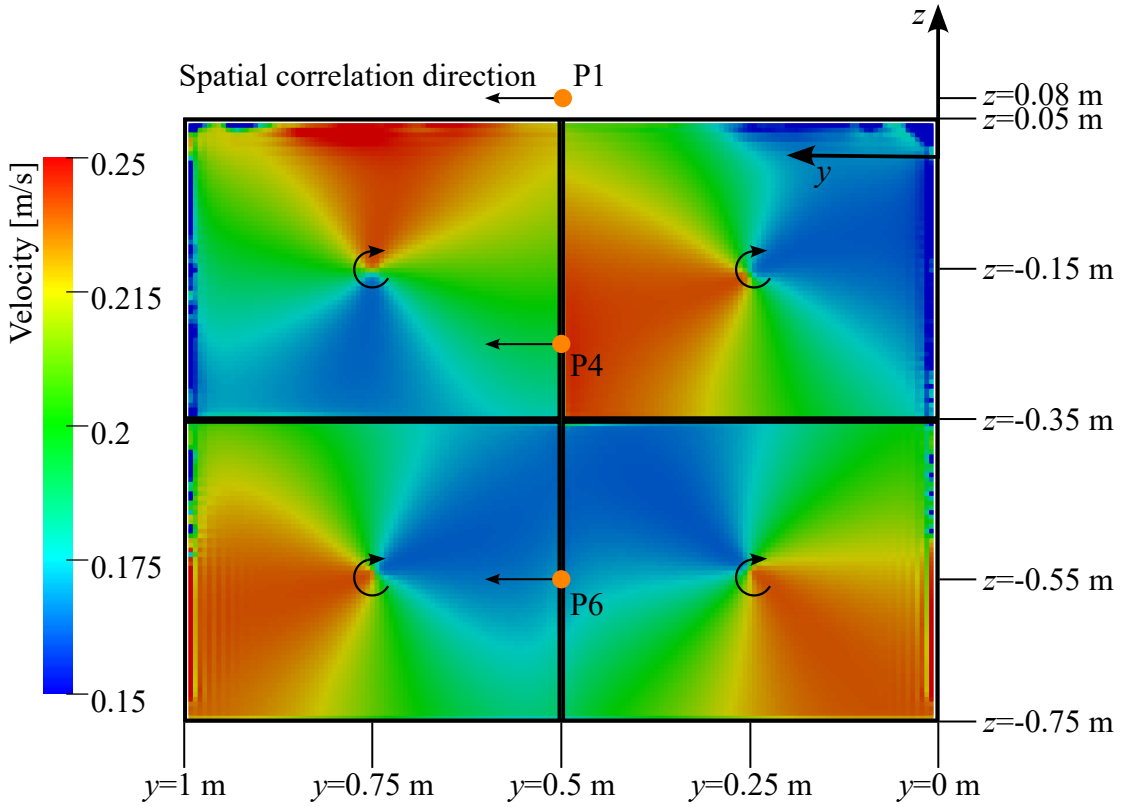

Fig. 3.21. Inlet patch with rotating velocity fields and measurement locations P1,4,6 and spatial correlation direction.

where

$$x_{\mathrm{CG}} = \frac{\sum_i (x_i \overline{\alpha_i} A_i)}{\sum_i (\overline{\alpha_i} A_i)} \tag{3.27}$$

is the x-coordinate of time-averaged center of gravity, $\overline{\alpha_i}$ the time-averaged volume fraction of cell, A_i the surface area of the cell and x_i the x-coordinate of the cell center. The variance (before taking the square root) is normalized by the total area of the nappe in the given horizontal slice since the nappe is continuously evolving while free-falling. In principle, since the flow is 2D, any y-position would yield the same result. However, due to the relatively short averaging time leading to diffuse time-averaged nappes as seen later in Fig. 4.3, the standard deviation (Eq. 3.26) was computed at 16 spanwise (y) positions each for a calculation width of 50 mm over the central part of the nappe (-0.4 m $\leq y \leq$ 0.4 m) where the flow can be considered two-dimensional without edge effects. The entire mass of a cell is

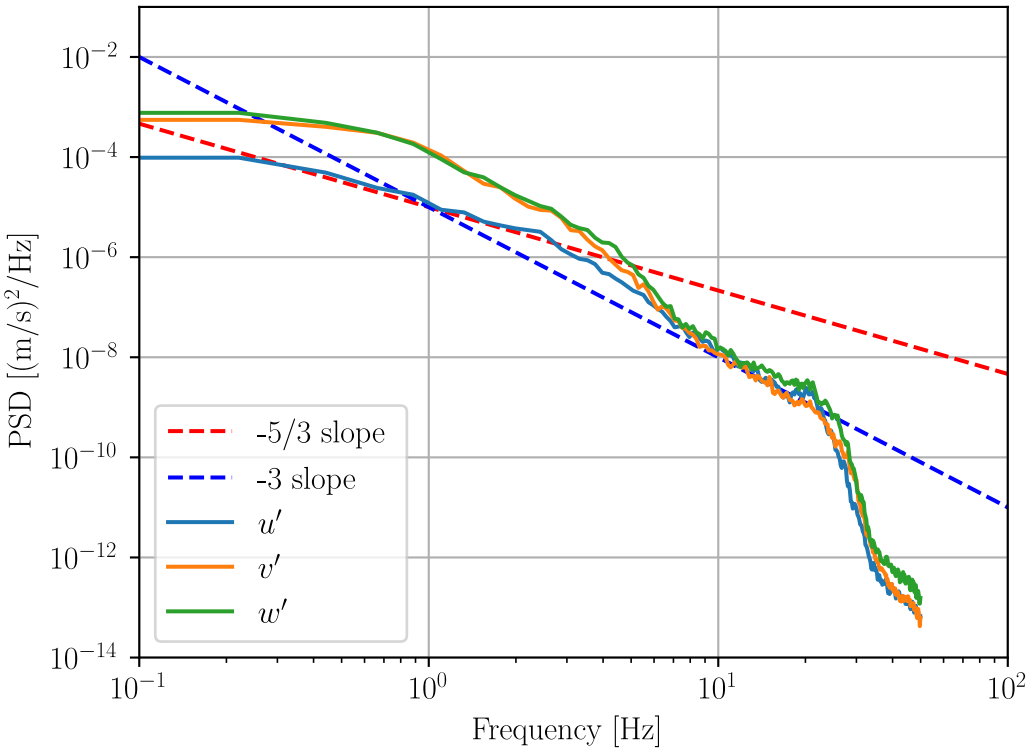

Fig. 3.22. Power spectrum density of the upstream flow situation for P3 (see Fig. 3.12).

attributed to a spanwise position when the center of the cell is located inside the calculation width. This can lead to an underestimation or an overestimation of the nappe mass in a spanwise positions. The biggest possible error is that the mass of half a cell is assigned incorrectly on both sides of the calculation width. With a maximum cell edge length of 6.25 mm at the nappe and a calculation width of 50 mm, this results in a maximum error of 12.5 %. However, the expected error is 6.25 % and even less since most parts of the nappe has a maximum cell edge length of 3.125 mm. The standard deviation computed at the 16 spanwise (y) positions is then averaged over all positions. The result was also denoted σ for simplicity and yields a characteristic lateral width of the undulating nappe. It should be noted that since the centroid x_{CG} is defined for each y-position, the final spatially-averaged standard deviation of all 16 y-positions eliminates the dispersive effects due to non-convergence at each position.

3.4.7 Mesh Independence of Nappe Development

The upstream flow situation of Case 5.9 with CEL_u = 6.25 mm is applied to different cell-edge lengths for the water-air interface in the vicinity of the nappe (Case 5, Case 5.1 and Case 5.2, see Table 3.2).
The used cell-edge length depends on the distance r to the $\alpha = 0.5$ iso-surface of the nappe. For $r \leq 4$ cm the cell-edge length is given by CEL_n and for 4 cm $< r \leq 10$ cm the cell-edge length is given by CEL_f (see Fig. 3.7), both cell-edge length are given in Table 3.2.

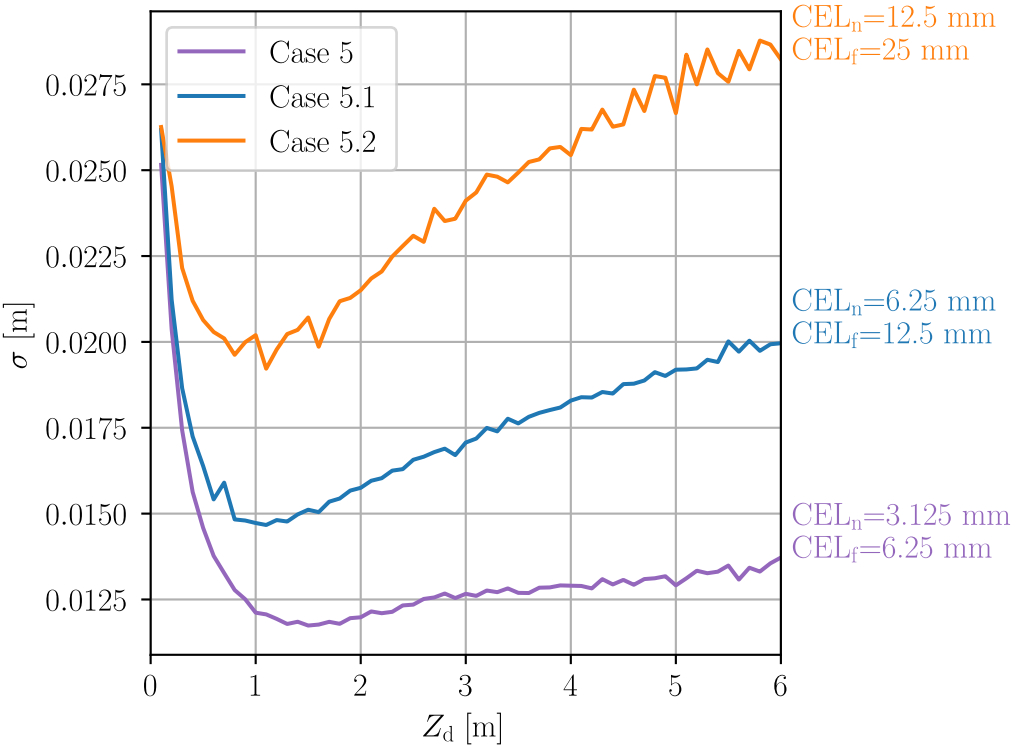

Fig. 3.23. σ against Z_d for different cell-edge lengths (CEL_n, CEL_f) (see Fig. 3.7 and Table 3.2) at the water-air interface in the nappe area.

The results are given in Fig. 3.23, where it can be seen that the finest mesh (Case 5) does not reach convergence. The extent to which σ drops for $Z_d \leq 1.5$ m and the increase in σ for $Z_d > 1.5$ m show a clear dependence on the mesh size where for a finer mesh the start of the increase in σ is retarded and the increase is lower.
For later investigations, cell-edge lengths of CEL_n = 3.125 mm and CEL_f =

6.25 mm are chosen (Case 5), since a finer grid is no longer manageable due to the limitation of calculation resources.

3.4.8 Artificial Compression Term

The influence of the artificial compression term on the nappe development is investigated which is introduced to counteract numerical diffusion. The transport equation of α with the artificial compression term (3. term LHS) is given again by

$$\frac{\partial \alpha}{\partial t} + \nabla \cdot (\overline{\boldsymbol{U}}\alpha) + \nabla \cdot (\alpha(1-\alpha)U_\mathrm{r}) = 0 \tag{3.28}$$

where

$$U_\mathrm{r} = ((1 - c_{\mathrm{i}\alpha})c_\alpha |U_\mathrm{sf}| + c_\alpha c_{\mathrm{i}\alpha} |\overline{\boldsymbol{U}}|) \frac{\nabla \alpha}{|\nabla \alpha|} \tag{3.29}$$

is the compression velocity (see section 3.1). The compression velocity is controlled in its intensity by c_α and switches it off for $c_\alpha = 0$. $c_{\mathrm{i}\alpha}$ controls the ratio between compression normal to the direction of flow and isotropic compression such that an increase in $c_{\mathrm{i}\alpha}$ increases the isotropic compression part. For $c_{\mathrm{i}\alpha} = 0$ the isotropic compression is switched off.

Isotropic compression can be used to counteract numerical diffusion at interfaces in the flow direction. Such interfaces exist, for example, at falling water drops. The compression in the flow direction was chosen to account for potential effects due to water-air interfaces. However, no water-air interfaces in the flow direction were observed, leaving the compression in flow direction without effect. Therefore, only the variation of c_α will be discussed in the following.

The model setup shown in Fig. 3.7 is used with the upstream flow situation of Case 5 (see Table 3.2). The mesh and the solver settings beside the user-defined value of c_α are the same for all investigated cases.

The differences in the nappe development concerning the user defined values of Eq. 3.7 can be seen in Fig. 3.24 by comparing the $\alpha = 0.5$ iso-surface of the nappe in the frontal view. The simulation time is the same for all cases. All iso-surfaces show similar deformations at the upper part of the nappe. For $c_\alpha = 0.0$ and $c_{\mathrm{i}\alpha} = 0.1$, areas with $\alpha \geq 0.5$ are present in thread-like structures for $Z_\mathrm{d} \geq 1.5$ m. Applying $c_\alpha = 0.1$ and $c_{\mathrm{i}\alpha} = 0.1$ noticeably counteracts the diffusion of the α field.

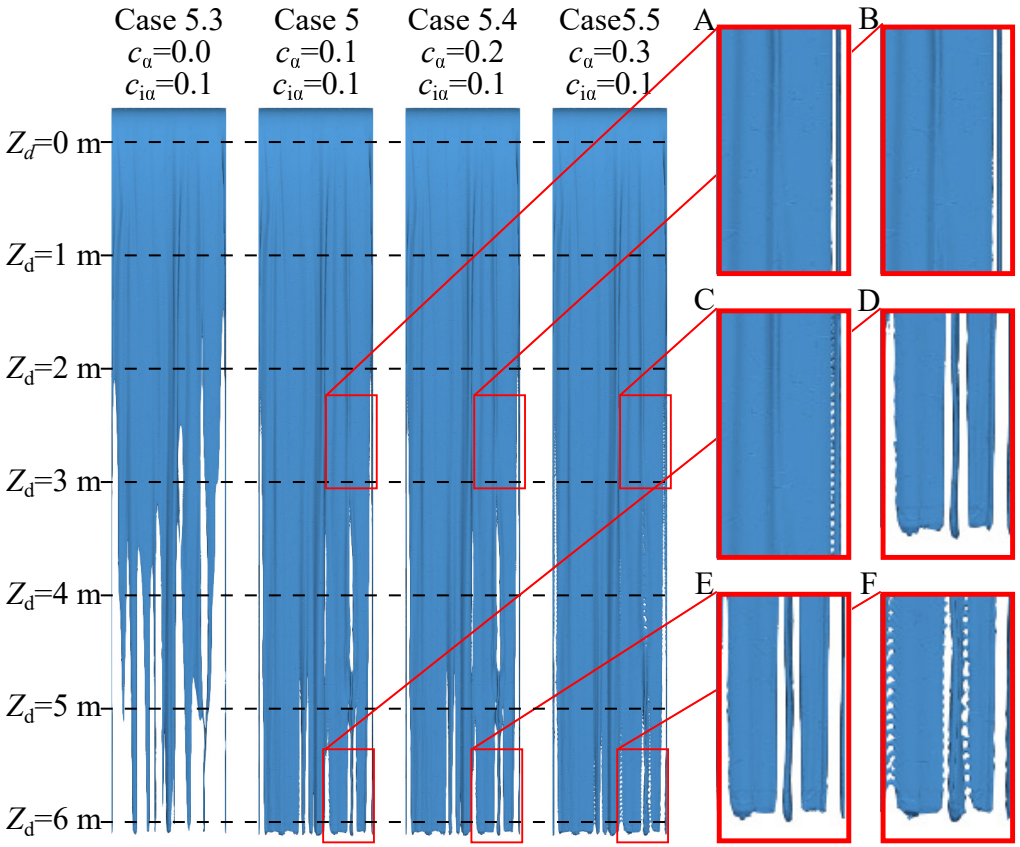

Fig. 3.24. $\alpha = 0.5$ iso-surfaces for different compression factors for similar upstream flow conditions. All iso-surfaces are evaluated at the same simulation time ($t = 33$ s).

A further increase of the compression factor with $c_\alpha = 0.2$ and $c_{i\alpha} = 0.1$ has only a minor impact regarding the reduction of diffusion. For $c_\alpha = 0.3$ and $c_{i\alpha} = 0.1$, a roughening of the nappe surface at the edge arises for $Z_d \geq 2$ m (Fig. 3.24 C). The roughening increases in intensity with increasing Z_d. For $Z_d \geq 5$ m the roughening extends to the center of the nappe (Fig. 3.24 F). These deformations of the nappe surface are not observed for $c_\alpha \leq 0.2$ and $c_{i\alpha} = 0.1$ (compare C,F and A,B,D,E). For the later investigations, $c_\alpha = 0.1$ and $c_{i\alpha} = 0.1$ are chosen. The slight reduction in numerical diffusion for $c_\alpha = 0.2$ and $c_{i\alpha} = 0.1$ is foregone here to ensure that the nappe does not undergo artificial deformations due to the compression velocity.

Chapter 4

Numerical Results

Hydraulic structures like weirs restrict the natural flow of rivers, creating barriers that can limit the movement of aquatic organisms and thereby reduce the ecological connectivity. The descent of fish at such structures can occur via nappes, whose tailwater flow situation is very likely determined by the nappes impact situation. The scope of this chapter is to investigate whether upstream induced turbulence affects the nappe shape and thereby its impact situation. Therefore numerical CFD simulations were conducted with nappe configurations subjected to varying upstream turbulence intensities. The investigations were carried out using the Volume-of-Fluid method (VOF) with Large Eddy Simulations (LES) and unsteady Reynolds-averaged Navier Stokes (URANS) models, as previous studies based on URANS models have concluded that upstream turbulence has no impact on nappe widening. However, this contradicts the hypothesis proposed in this study based on the author's observations of a prototype-scale nappe. The chapter is structured into four sections. The first section examines the shape of nappe surfaces under various upstream turbulence conditions using LES modeling by presenting visual representations illustrating how the nappe surface changes under different upstream conditions, providing a qualitative understanding of the impact of turbulence on nappe behavior. The second section expands on the previous analysis to assess the widening of the nappes through a more quantitative comparison. The third section compares the effectiveness of LES and URANS models in predicting the behavior of nappes under different turbulence intensities. Finally, the fourth section explores the sensitivity of nappe widening to variations in volume flow rate under same upstream turbulence levels.

4.1 Shape of the Nappe Surface via LES

The impact of upstream-induced turbulence on the development of nappe is only minimally explored. The only investigations conducted thus far have been limited to numerical analysis using an unsteady Reynolds-Averaged Navier-Stokes (URANS) turbulence model, which showed no effect of upstream turbulence on the overflow. However, based on observations from a prototype model, the hypothesis in this work is that upstream turbulence indeed has an impact on nappe development. To investigate this effect, the previous chapter addressed the modeling of multiphase flow and the genearation of turbulent structures by a boundary condition. A evaluation method based on the standard deviation of the nappe was presented to evaluate the nappe development during free fall. The goal of this chapter is to examine and determine the effects of upstream-induced turbulence on nappe development. In this chapter, different levels of turbulence intensity (ranging from 7.5 % to 19.7 %) are generated and their impact on the nappe development is examined. The same mesh, volume flow rate, and solver settings are used for all cases to maintain consistency. To set the turbulence intensity in the upstream tank, a coarser resolution of the nappe is first calculated for 100 seconds and then mapped to the full mesh of each case. An additional 4 seconds is then simulated to allow the nappe to form on the fine mesh. Finally, the water distribution of the nappe is averaged over 11 seconds.

Fig. 4.1 shows the α-distribution on horizontal slices through the nappe at three different drop depths Z_d for all LES cases with $Q = 0.16\ \mathrm{m}^3/\mathrm{s}$ and associated inlet turbulence intensities I (Table 3.2). The snapshots of the nappes were taken at the same simulation time for each case ($t = 15$ s). $t = 0$ s denotes the moment when the calculation of the nappe began over the entire drop depth, using the already converged solution of the upstream flow situation as initialization.

For Case 1, the width of the nappe core (with $\alpha = 1$) decreases with increasing drop depth. This is in line with theory as the velocity of the water in the nappe increases due to gravitational acceleration, the cross-sectional area of the water flowing through the nappe must decrease in order to maintain a constant flow rate. At $Z_\mathrm{d} = 1$ m the core of the nappe with α values of 1 has a width of three cell edge length (9.375 mm). Towards the rim of the nappe (x-direction) the α values

decrease and form the water-air interface ($0 < \alpha < 1$). At $Z_d = 3$ m the core of the nappe ($\alpha = 1$) does not exist any longer. $\alpha = 1$ can only be found in the area of the nappe deformation at $\sim y = 0.6$ m. At $Z_d = 6$ m the maximum α reduces to 0.95 at $\sim y = 0.6$ m. The major part of the nappe profile at this drop depth has $\alpha < 0.75$.

The behavior observed here was also reported by Carrillo et al. (2021) who investigated a nappe at a sharp-crested weir with a specific flow rate of 0.096 $m^3/s/m$. Carrillo et al. (2021) describe how the constriction of the nappe is primarily caused by gravity, but they also observe a widening of the water-air interface around the nappe due to the process of surface aeration or nappe oscillations. Additionally, Carrillo et al. (2021) provide a theoretically calculated breakup length that is similar in magnitude to the drop depth at which the core of the nappe is no longer visible in Case 1 (approximately 3 meters).

The reduction in the maximum α value seen for Case 1 and the increase in the water-air interface width with increasing drop depths could hence result from air entrainment an nappe oscillations, as mentioned by Carrillo et al. (2021). It should be noted that the observed widening of the water-air interface in the experimental studies is based on time-averaged measurements, which are necessary for void fraction measurement. In the numerical simulation shown here, however, the water-air distribution in the nappe is based on an instantaneous snapshot of the flow. Due to the high level of detail provided by the instantaneous snapshot of the water-air distribution in the nappe in the numerical simulation, nappe oscillations or air entrainment would be directly visible. The deformations observed on the nappe surface in the numerical simulation (e.g., Case 1 at 1 meter) do not show the characteristic horizontal wave pattern of nappe vibrations. Instead, they appear sporadically across the width of the nappe. A more recent explanation for the widening of the water-air interface around the nappe in the numerical investigations is numerical diffusion, as the mesh of the nappe still shows mesh dependency (see section 3.4.7).

The nappe profiles at $Z_d = 3$ m with $I \geq 9.8$ % (Case 3 - Case 8) show deformations which are larger in amplitude than the width of the nappe. These deformations increase in amplitude and number with increasing I and have a non-stationary character. Nappes of $I \geq 13.8$ % (Case 5 - Case 8) have discontiguous profiles at

Z_d = 6 m with areas of $\alpha = 1$. The splitting up of the nappe profiles is reminiscent of breakup, as observed for water jets separating into individual falling water packets. However, the horizontal profiles through the nappes shown here do not make it clear whether the nappes break up into separately falling water packages as mentioned by Castillo et al. (2014) or split up into threadlike structures, as observed by Bercovitz et al. (2016).

In experimental investigations, nappe widening and break up can be evaluated by high-speed photography (e.g. Ervine and Falvey, 1987). A similar approach is used here by assuming that the instantaneous $\alpha = 0.5$ iso-surface equals the water-air interface for the instantaneous flow situation. Lightning with a side illumination and shading is used to reveal the deformations of the iso-surface.

Fig. 4.2 shows the resulting front view of the nappes for the different I investigated. In all cases, a deformation of the nappe surface can be identified just after the weir in the upper part of the nappe. The surfaces of the nappes show shadows (darker lines) in the longitudinal direction which increase in their intensity and number as I increases. The nappe surfaces of all cases show gaps which are only located at the sides of the nappe (y-direction) for $I \leq 9.8$ % (Case 1 - Case 3), but for $I \geq 11.9$ % (Case 4 -Case 8) these surface gaps do also exist in the center of the nappe for $Z_d \geq 1.5$ m. A gap in the surface indicates an area with $\alpha < 0.5$. The gaps increase in number with increasing I till the nappe surface is split into thread-like structures (seen for $I \geq 17.8$ % and $Z_d \geq 5$ m). However, a continuous line from the bottom of the nappe at $Z_d = 6$ m to the top at $Z_d = 0$ m can always be found for all cases within the body of water ($\alpha > 0.5$). In other words, the deformation of the nappe surface does not lead to isolated water packages and hence no break up of the nappe occurs which corresponds to the observations of Bercovitz et al. (2016). Furthermore, the threadlike structures seen in Fig. 4.2 are clearly not a signature of nappe vibration which is characterized by a horizontal wave pattern (e.g. Lodomez et al., 2019; Anderson and Tullis, 2018).

Fig. 4.3 depicts horizontal slices through the nappe, showing the time-averaged distribution of the void fraction ($\overline{\alpha}$) as computed from the numerical simulation. To obtain the time-averaged $\overline{\alpha}$ distribution, an averaging period of 11 seconds was used. The time-averaged $\overline{\alpha}$ distribution was obtained by starting the averaging process after the target mesh was initialized with the converged upstream solution.

The numerical simulation for the whole nappe length was then run for an additional 4 seconds before starting the averaging process. The 4-second period allowed sufficient time for any transient behavior in the development of the nappe to end. Since the nappe falls approximately 6 meters per second, this 4-second period was sufficient to allow any transient behavior (The majority of the transient behavior is concentrated at the tip of the nappe, where the water stream punches through the air) to end before starting the averaging process. For Case 1, the nappe width reduces with increasing Z_{d}. At $Z_{\mathrm{d}} = 1$ m the center of the nappe has $\overline{\alpha}$ values of 1 over the total length (y-direction). Such high $\overline{\alpha}$ values do not exist any longer at $Z_d \geq 3$ m.

The simulations show that when the turbulent intensity I is equal to or greater than 11.9% (Case 4 - Case 8) and $Z_{\mathrm{d}} = 1$ m areas with $\overline{\alpha} < 1$ values are present in the center of the nappe. As the turbulent intensity increased, these areas grow in size. The time-averaged profiles of the high I nappes are not as smooth as the low I nappes due to decreasing convergence with higher fluctuations of the deformations within the fixed simulation time. However, the differences between the instantaneous α-distribution (Fig. 4.1) and the time-averaged $\overline{\alpha}$-distribution (Fig. 4.3) increase with Z_{d} and I, as expected with the increasing fluctuations of the deformation. Hence, at $Z_{\mathrm{d}} = 6$ m and $I = 19.7$ % there is no discontiguous nappe profile as seen for the instantaneous α-distribution (Fig. 4.1), but Fig. 4.3 shows a massively diffused $\overline{\alpha}$-distribution.

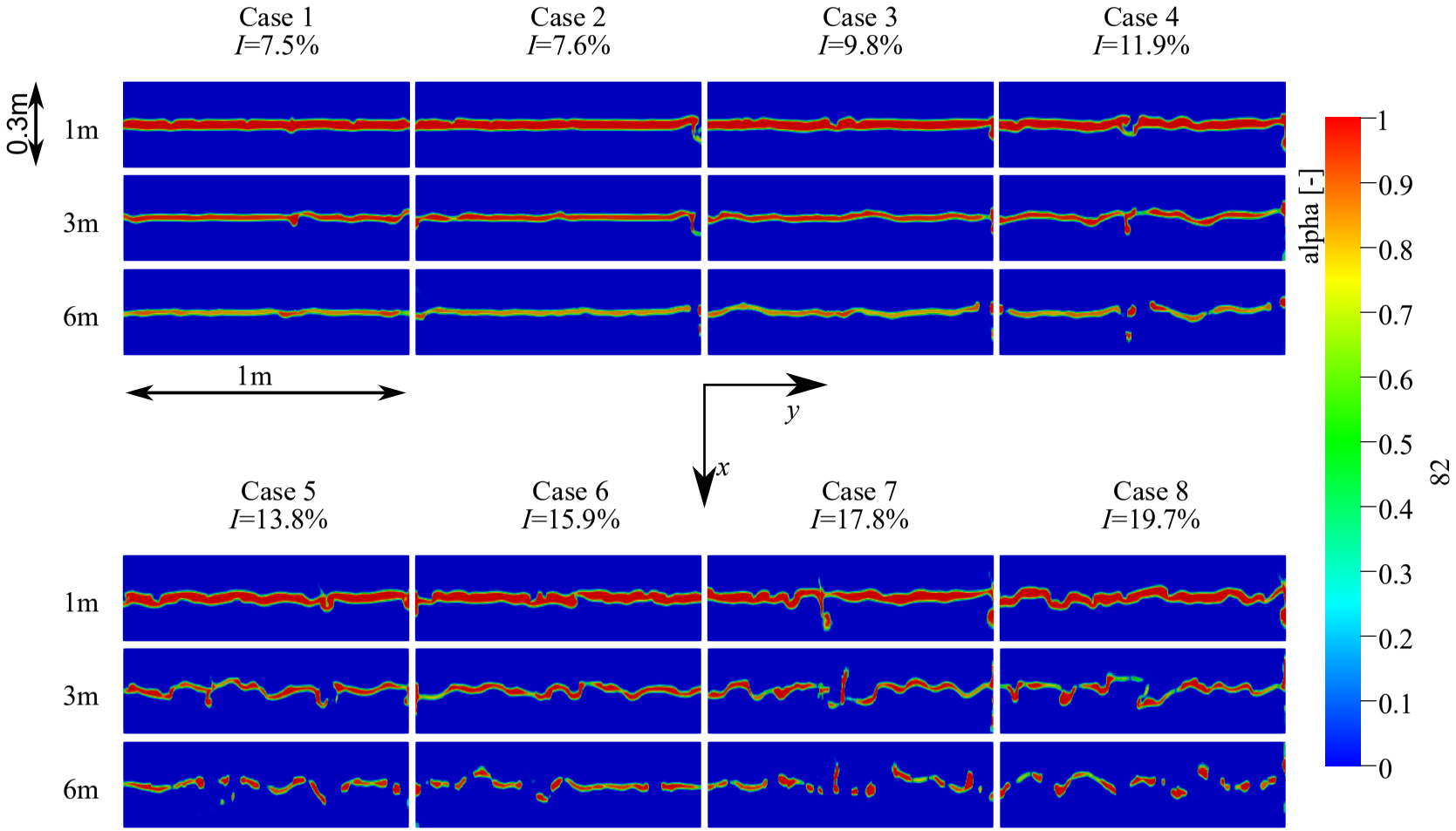

Fig. 4.1. Horizontal slices through the nappe of the instantaneous α-distribution at t=15 s for three levels of Z_d and for all I cases with Q = 0.16 m^3/s simulated with LES.

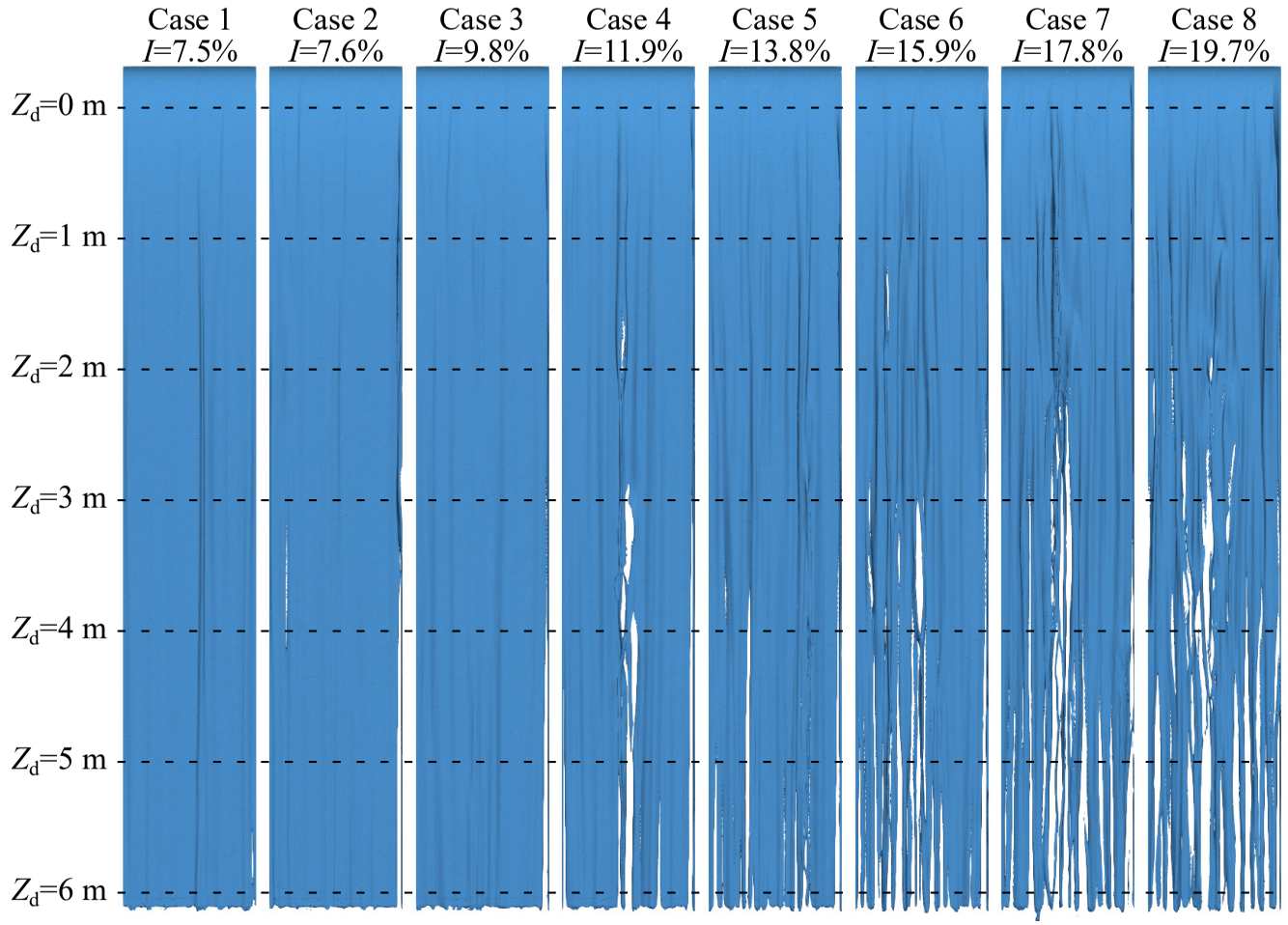

Fig. 4.2. Frontal view of α = 0.5 iso-surface at t=15 s with shading to visualize the nappe surface deformation, for different I.

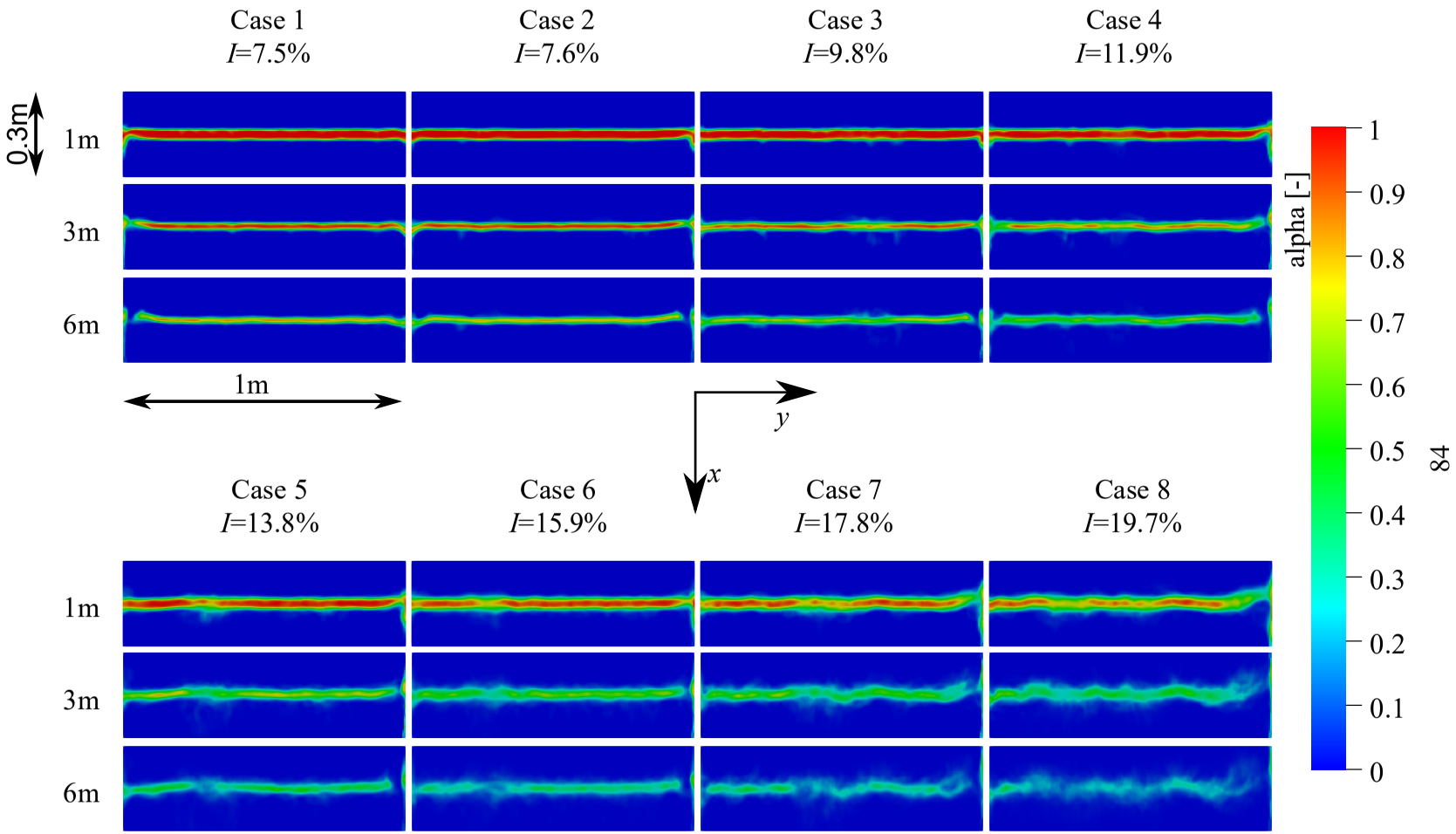

Fig. 4.3. Horizontal slices through the nappe of the time-averaged $\overline{\alpha}$-distribution for three levels of Z_d and for different I.

4.2 Evaluation of Nappe Widening

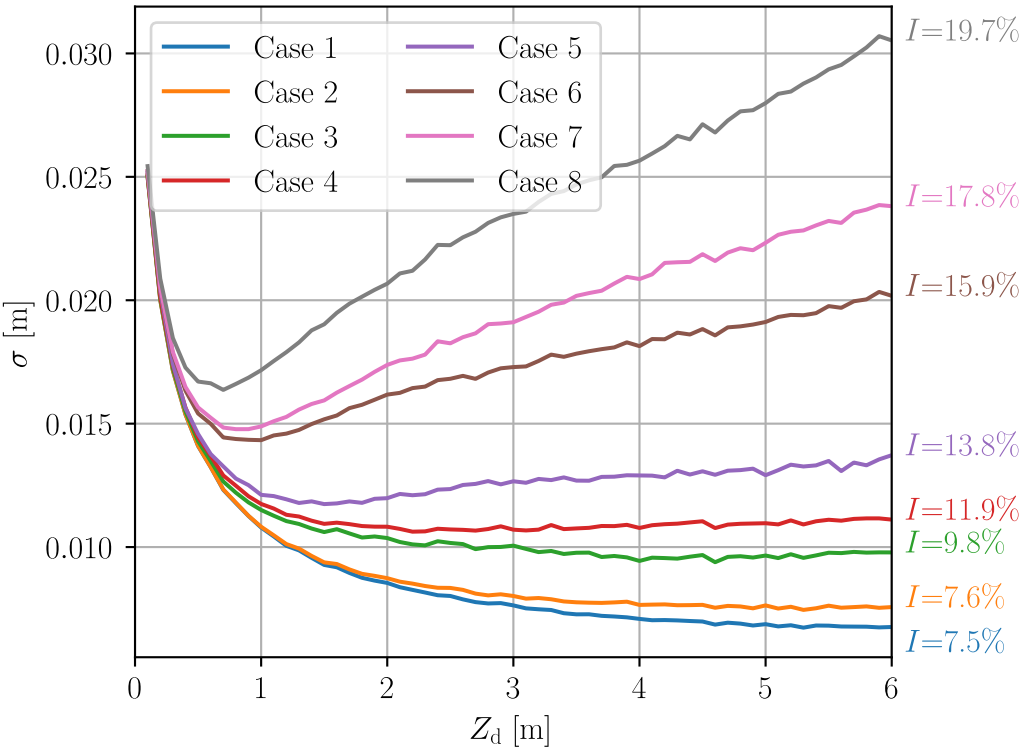

Fig. 4.4. Lateral nappe-width σ against drop depth Z_d for different upstream turbulence intensities I.

Fig. 4.4 shows standard deviation (computed by Eq. 3.26) against drop depths ranging 0.1 m $\leq Z_d \leq$ 6 m for upstream turbulence intensities ranging 7.5 % $\leq I \leq$ 19.7 %. For $Z_d = 0.1$ m the standard deviation σ equals 0.0255 m for all cases. With increasing Z_d σ decreases down to $Z_d \lesssim 0.5$ m for all cases. For $I \leq 9.8$ %, σ continues to decrease monotonically for all Z_d. For nappes with $I \geq 11.9$ % σ also decreases for small Z_d, but a minima accrues in the range 0.7 m $\lesssim Z_d \lesssim$ 1.5 m and σ increases with higher Z_d. The increase of σ itself increases with increasing I while the slope changes at decreasing Z_d with increasing I. For $I = 19.7$ % σ for $Z_d \geq 4$ m exceeds the initial σ value.

All these observations point to the increasing influence on the nappe undulations as I increases, which can be strong enough to counteract the nappe thinning due to gravitational acceleration. In the following, such situations are referred to as

turbulence-driven nappe development.
The results obtained from the simulation process cannot be taken as absolute results, but only as relative results due to the various uncertainties involved in the simulation process. One of the most critical uncertainties in the simulation process is the mesh size, which plays a crucial role in determining the level of accuracy of the results obtained from the simulation. The mesh size has a direct impact on the accuracy of the numerical solution of the α transport equation. Specifically, the mesh size affects the advection term of the transport equation, which describes how the scalar field is transported by the fluid flow. A finer mesh results in less numerical diffusion for the advection term. Hence, an increase in mesh size has similar influence as increasing turbulence intensity.

4.3 Comparison of LES and URANS

The LES simulations are now compared to URANS models to discern their ability to capture the turbulence-driven development of the nappe. The use of URANS models in previous studies concluded that a difference in upstream turbulence has no influence on the nappe characteristic (Castillo et al., 2014; Muralha et al., 2020). For the comparison, the LES model setup of Case 8 with $I = 19.7$ % (see Table 3.2) is used as a reference for the URANS simulations which have approximately the same upstream turbulence intensity with $I = 20.4$ %. The mesh, the time-resolution, the transport schemes and the solver settings were chosen to be identical to the LES simulation in order to restrict differences to the turbulence models. The three URANS simulations, Cases 8.1, 8.2 and 8.3, differ in the chosen turbulence model and in the α-transport equation (see Table 3.2): For Cases 8.1 and 8.2, the standard constant-density k-ω-SST model is used, while for Case 8.3, the density-varying k-ω-SST$_\rho$ model is used (both models are incompressible). Furthermore, while for Case 8.1, the standard transport equation in OpenFOAM® v2012 without turbulent scalar flux term is used (Eq. 3.6), Cases 8.2 and 8.3 use the expanded α-transport equation where the flux is modeled via a gradient-diffusion hypothesis (Eq. 3.22).
Fig. 4.5 shows the front view of the nappes for Cases 8 (LES), 8.1, 8.2 and 8.3 (URANS). The three nappes which were calculated by using URANS models gen-

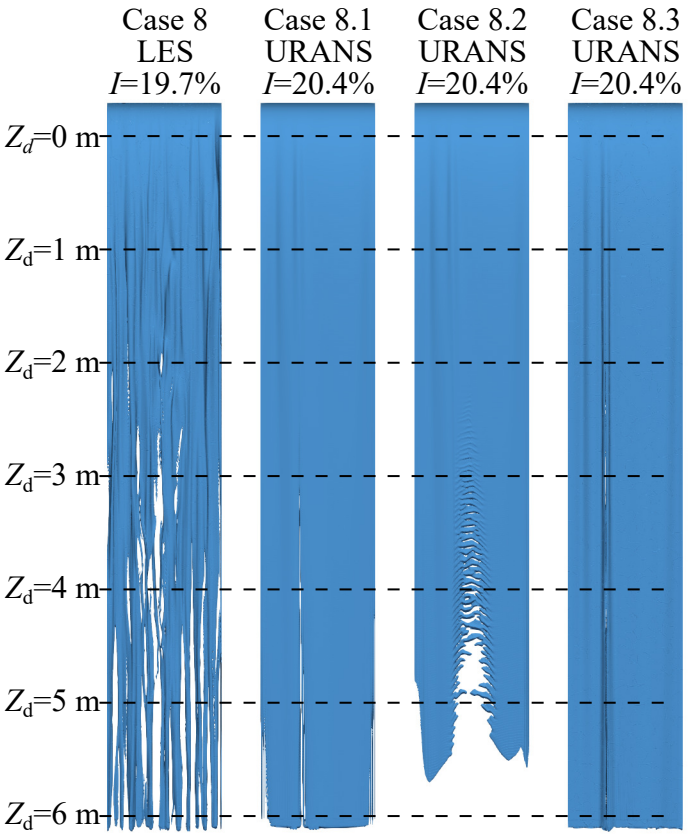

Fig. 4.5. Front view of $\alpha = 0.5$ iso-surface for comparing the nappe-surface deformation for Case 8 via LES with Cases 8.1, 8.2 and 8.3 via URANS (see Table 3.2). Case 8.1: k-ω-SST turbulence model with standard α-transport equation (Eq. 3.6). Case 8.2: k-ω-SST model with α-transport equation expanded by turbulent flux term (Eq. 3.22). Case 8.3: density-varying k-ω-SST$_\rho$ model with expanded α-transport equation Eq. 3.22.

erally reveal fewer and weaker signatures of the widely-occurring and thread-like structures observed in the LES case. While some differences between the three URANS models can be observed for larger drop depths, none captures the nappe deformations as in the LES simulation, although all have approximately the same inlet turbulence intensity I 1 m upstream of the weir. Evidently, the deformations cannot simply be ascribed to the turbulence intensity, but to the underlying turbulent structures. It should also be noted that while the inlet boundary conditions are also the same for all four cases, the resolved part of the turbulence intensity I 1 m upstream of the weir in the three URANS simulations is less than in the LES

simulation ($I_{d_{URANS}}$ = 11.4 %, $I_{d_{LES}}$ = 15.7 %). It can therefore be surmised that only relatively large and strong turbulent structures are simulated in the inlet tank in comparison to the LES model.

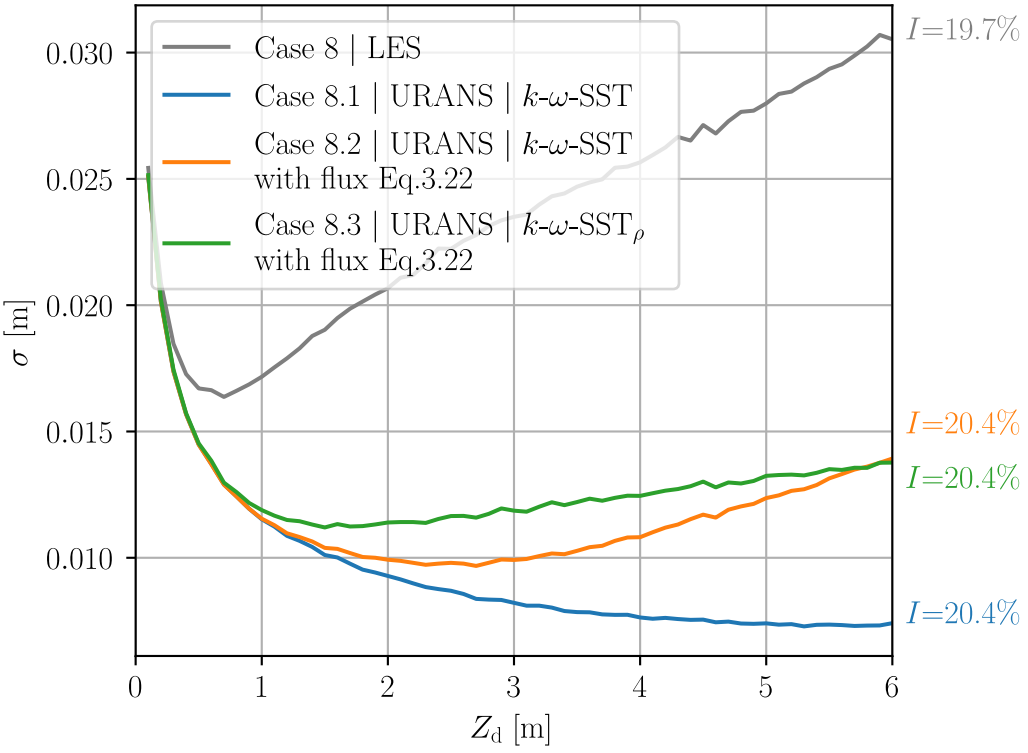

Fig. 4.6. Comparison of LES (Case 8.1) and URANS simulations (Cases 8.1, 8.2 and 8.3). All simulations performed with the same spatial grid and time-resolution.

Fig. 4.6 compares the nappe standard deviation (σ) development for all four cases. It can be readily seen that the curves of the three URANS simulations differ significantly from the curve of the LES simulation. While the behavior of all four cases is congruent with decreasing σ up to $Z_d \approx 0.3$ m, the three URANS continue to decrease congruently up to $Z_d \approx 1.5$ m and the LES case increases for $Z_d > 0.7$ m, resulting in significantly larger nappe standard deviation than the URANS ones for $Z_d > 0.3$ m. Also, the URANS Case 8.1 shows a monotonic decrease similar to the LES Cases 1, 2 and 3 with lower turbulence intensity I at the inlet (see Fig. 4.4). While Case 8.2 is the only URANS simulation which displays a strong increase in σ with Z_d as in the LES, the standard deviation is much lower and the slope change occurs much later.

Clearly, all investigated URANS simulations predict a different nappe behavior than the LES simulation which at least visually corresponds well to the observation in Fig. 1.2. The differences are quantitative for Case 8.2 and also qualitative for Cases 8.1 and 8.3 where no minimum in standard deviations is observed for Case 8.1. Case 8.2 with the standard k-ω-SST model combined with the expanded α-transport equation at least captures a clear increase in nappe standard deviation for larger drop depths, albeit weaker and retarded. Given that all models are run with the same solver parameters, grid, temporal resolution and upstream turbulence intensity, the differences must lie essentially in the turbulence models. More specifically, it can be postulated that it boils down to the models' ability to reproduce the large-scale anisotropic turbulent structures.

In order to pursue this conjecture, the Q-criterion (Jeong and Hussain, 1995) was computed to visualize the vortex structures in the upstream tank and nappe. Fig. 4.7a,b show the results for Cases 8 (LES) and 8.1 (URANS) and Fig. 4.8a,b show the results for Cases 8.2 (URANS) and 8.3 (URANS) combined with the $\alpha = 0.5$ iso-surfaces. The same snapshot time as in Fig. 4.5 is used. The red-green coloring of the structures identifies clockwise and counterclockwise rotating vortices, respectively. It is readily apparent that the LES simulation captures a far greater number of vortex structures within the upstream tank as well as in the nappe. Comparing Fig. 4.7b with Fig. 4.8a,b shows that there is no significant difference in the amount and position of the upstream turbulent structures for the different URANS turbulence models. The differences in the standard deviation seen in Fig. 4.6 can hence not be traced back to differences in the upstream tank. Therefore, the disparity must originate from the chosen combination of the α transport equation and turbulence model, and the associated effects on the development of the nappe.

It can also be seen in the LES results and for the resolved vortex by the URANS simulations, that there is a direct link between the structures and the streaks on the nappe surface, as the streaks and structures are well-aligned. The vortex structures can be seen to follow the flow across the weir. Since the URANS simulations do not capture as many structures in the upstream tank, fewer streaks are observed in the nappe which explains the reduced nappe standard deviations.

The origin of observed structures in the nappe of the LES is not the sharp-crested

weir due to flow separation as might have been surmised. Instead, two upstream origins can be discerned in the LES simulation. The vortex structures which can be seen within the first 0.5 m of the plotted part of the upstream tank, spanning the cross-section, clearly originate at the inlet boundary forcing (2.5 m upstream of the weir) rather the bottom wall. On the bottom wall, smaller forwardly inclined structures indicating the characteristic hairpin wall-boundary layer structures can be observed. As the weir is approached and the flow moves upward (seen clearly in the mean flow streamlines in Fig. 3.14), these structures elongate. The free-stream structures from the inlet also appear to elongate. These elongations and possibly the generation of new streamwise structures could be due to centrifugal instabilities (i.e., Görtler vortices, Saric, 1994) caused by the concave nature of the streamlines, in addition to strong upward acceleration.

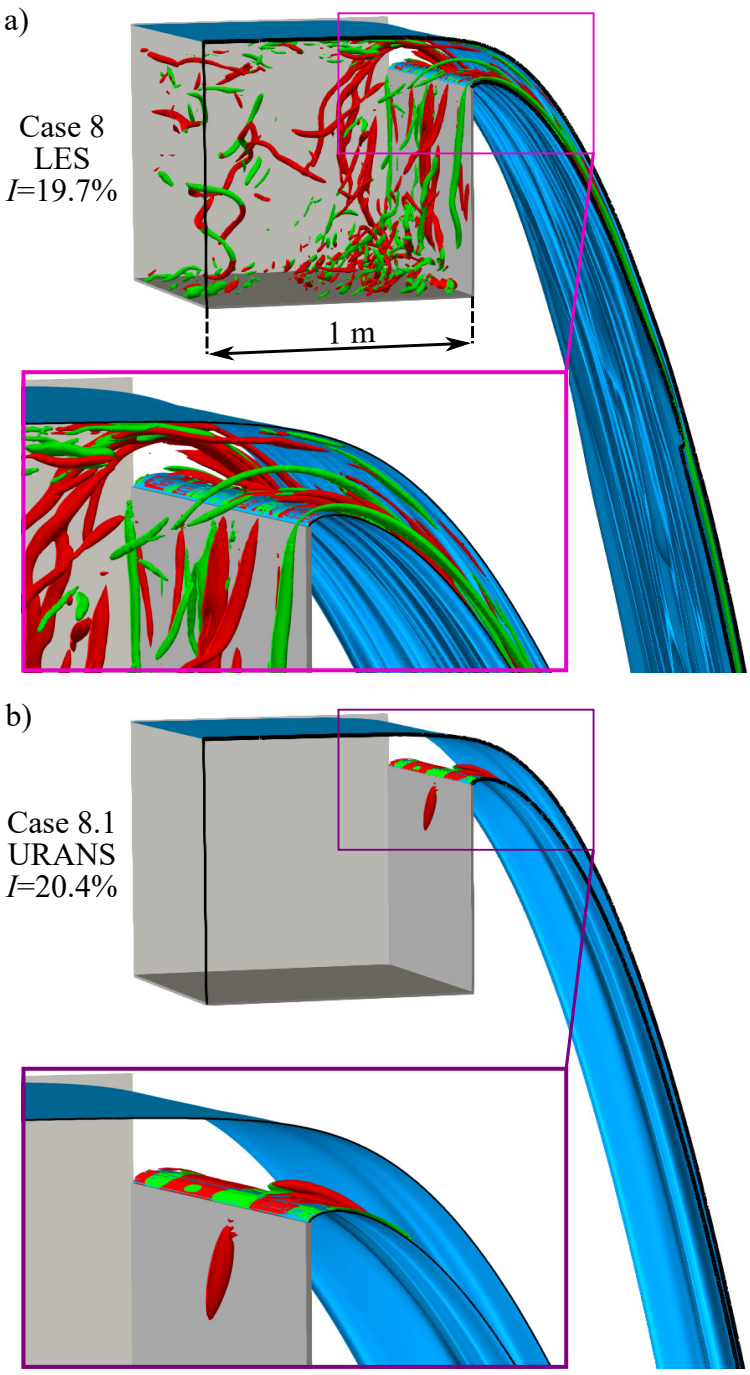

Fig. 4.7. Vortex visualization by the Q-criterion (Q = 10) and the α = 0.5 iso-surfaces (with shading) for Cases 8 (LES) (a) and Case 8.1 (URANS) (b). The plot includes the second half of the inlet tank. Red: clockwise rotation, green: counterclockwise rotation. The same snapshot time as in Fig. 4.5 is used.

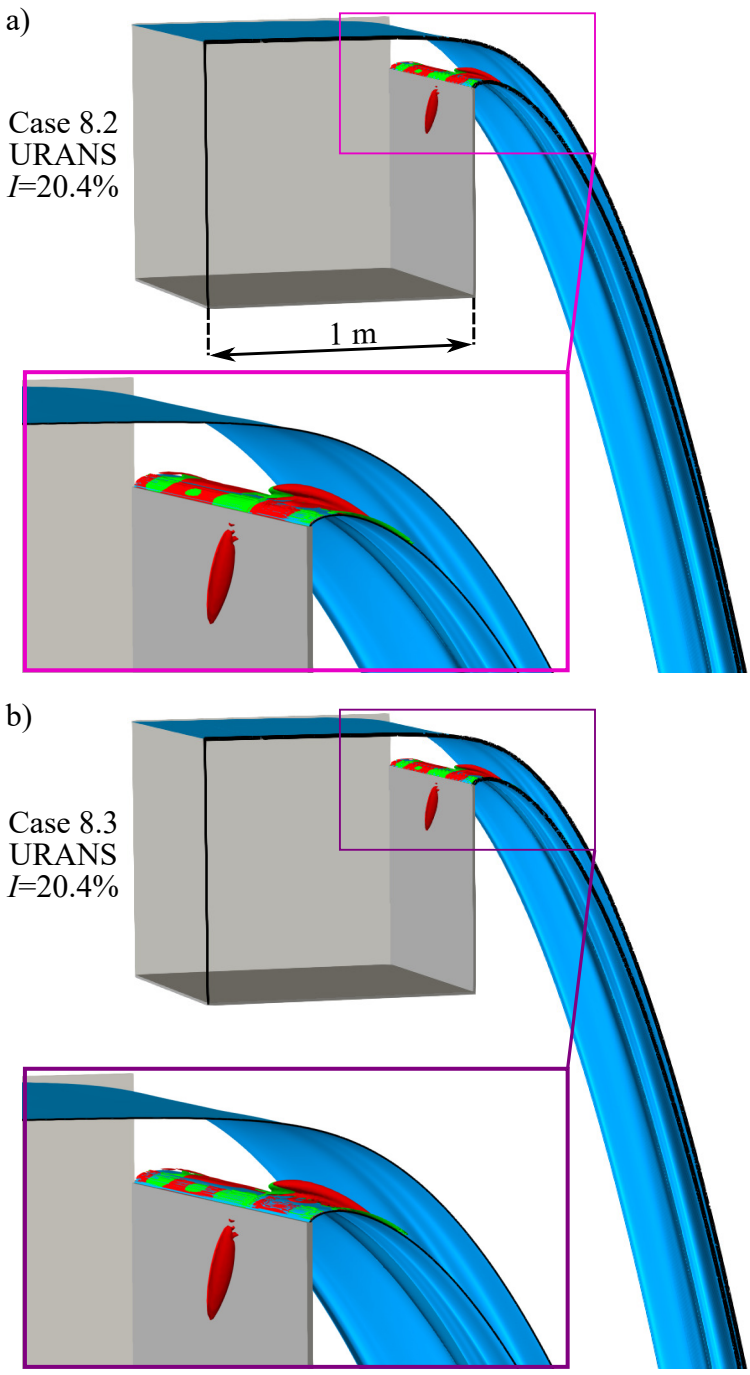

Fig. 4.8. Vortex visualization by the Q-criterion (Q = 10) and the α = 0.5 iso-surfaces (with shading) for Case 8.2 (URANS) (a) and Case 8.3 (URANS) (b). The plot includes the second half of the inlet tank. Red: clockwise rotation, green: counterclockwise rotation. The same snapshot time as in Fig. 4.5 is used.

4.4 Volume Flow Rate Sensitivity

Fish downstream migration at weirs is bound to the spill height of the weir, since it limits the size of descending fish. The necessary spill height is about twice the fish height (DWA, 2005). Hence, spill heights > 0.17 m resulting from specific volume flow rates > 0.16 m^2/s are typically necessary to achieve good ecological continuity. In order to test whether turbulent nappe development must also be taken into account in the case of increased volume flow rates, different volume flow rates with similar turbulence intensities are investigated.

The volume flow rates of Cases 5.11-5.13 range $0.16\,m^3/s \leq Q \leq 0.64\,m^3/s$ which result in spill heights of $0.17\ m \leq h \leq 0.41\ m$ and $1.7 \cdot 10^5 \leq Re \leq 2.7 \cdot 10^5$ based on the spill height. A summary of the investigated cases can be found in Table 3.2. Since the head water increases, the height of the inlet boundary patches and the rotation speed are adapted (see Fig. 3.9 and Table 3.2).

Since larger volume flow rates need a larger refinement area in the vicinity of the nappe, the mesh cell-edge length in the vicinity of the nappe (CEL_n, CEL_f) of all investigated cases here is limited to 6.25 mm for keeping the cell number within a manageable range of ≤ 60 Mio. cells.

The results of the investigation are shown in Fig. 4.9 which shows the development of the standard deviation σ over the drop depth Z_d for different volume flow rates Q, but with similar turbulence intensities I. It can be seen that nappes with higher volume flow rates have a higher initial standard deviation as expected due to the wider initial nappe width. For drop depths in the range of $1\ m \lesssim Z_d \lesssim 1.5\ m$ σ decrease for all cases down to ~ 50 % of the initial standard deviation with the minimum in σ at deeper drop depth for higher volume flow rates. For $1\ m \lesssim Z_d \lesssim 2\ m$, again depending on the volume flow rate, the slope changes and σ increases again with deeper drop depth Z_d, where the slope change is retarded for higher volume flow rates and the slope increases with the volume flow rate.

For making the nappe development independent from its initial lateral width, the standard deviation is normalized by the initial standard deviation at $Z_d = 0.1\ m$ and shown in Fig. 4.10.

$\sigma/\sigma_{0.1}$ of all investigated volume flow rates reduces to ~ 0.5 at $1\ m \geq Z_d \geq 1.5\ m$ with the minimum at a deeper drop depth for higher volume flow rates. After

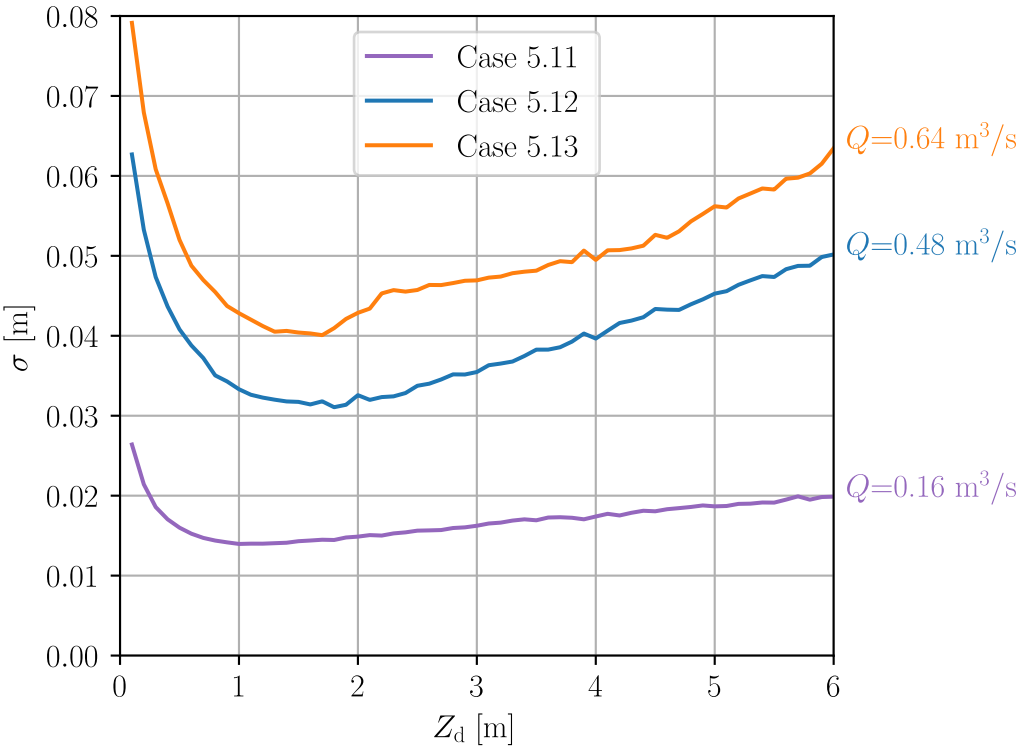

Fig. 4.9. Lateral nappe-width σ against drop-depth Z_d for different volume flow rates Q with similar upstream turbulence intensities $I \approx 14$ %.

reaching the minimum, $\sigma/\sigma_{0.1}$ increases again for all cases linearly and shows general overlap for the further curse. At $Z_d = 6$ m all cases reached nearly the same percentage of $\sim$ 80% of the initial standard deviation. This suggests that the nappe widening becomes more and more independent of the volume flow rate concerning the initial lateral nappe width with increasing drop depth.

With regard to the degree of nappe widening at $Z_d = 6$ m, however, it should be remembered that it had been shown in section 3.4.7 that the here obtained results show dependency on the mesh cell-edge length (CEL_n, CEL_f) and hence, numerical diffusion overestimates the nappe widening.

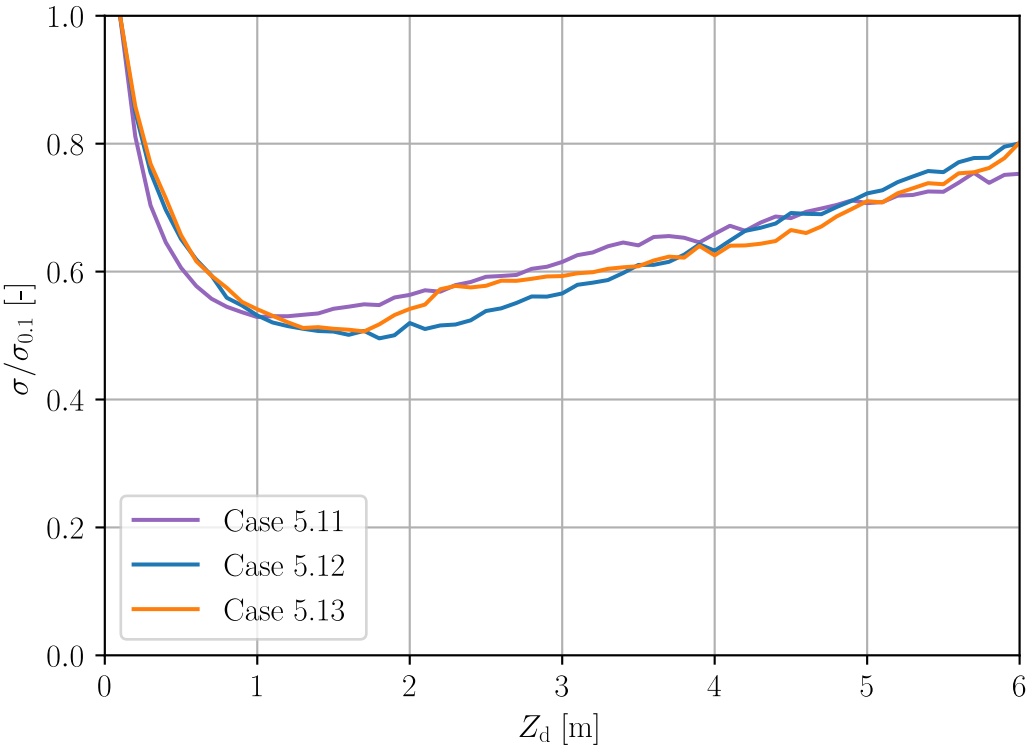

Fig. 4.10. Lateral nappe-width $\sigma/\sigma_{0.1}$ with the initial standard deviation $\sigma_{0.1}$ at $Z_d = 0.1$ m (Fig. 4.9) against drop-depth Z_d.

Chapter 5

Experimental set-up

Experimental investigations of nappes are crucial for improving our understanding of the factors that influence the development of the nappe during the fall. Since there is no self-similarity in nappe flows, scaling down the experiments effects the reliability of the results. Therefore, to ensure that the flow is representative of the system being modeled, nappes must be conducted at or close to prototype scale. This condition applies to the experimental setup situated at the Electricité de France (EDF) laboratory in Chatou, featuring a sharp-crested weir with a drop depth of 9.5 m and a width of 1 m. To analyse the upstream flow conditions of the nappe, acoustic Doppler velocimetry (ADV) measurements were performed in the upstream channel. To measure the nappe development during the fall, a custom-designed conductivity probe was developed and is detailed in this chapter. The evaluation of void fractions with conductivity probes is based on the significant difference in conductivity between water and air. To determine whether the tip of the probe is in air or water, conductivity probes typically rely on threshold-based logic. Here, a single-threshold method was used which is also presented in this chapter. The last section investigates the required measurement time to obtain converged time-averaged nappe profiles across different drop depths.

5.1 Model Setup

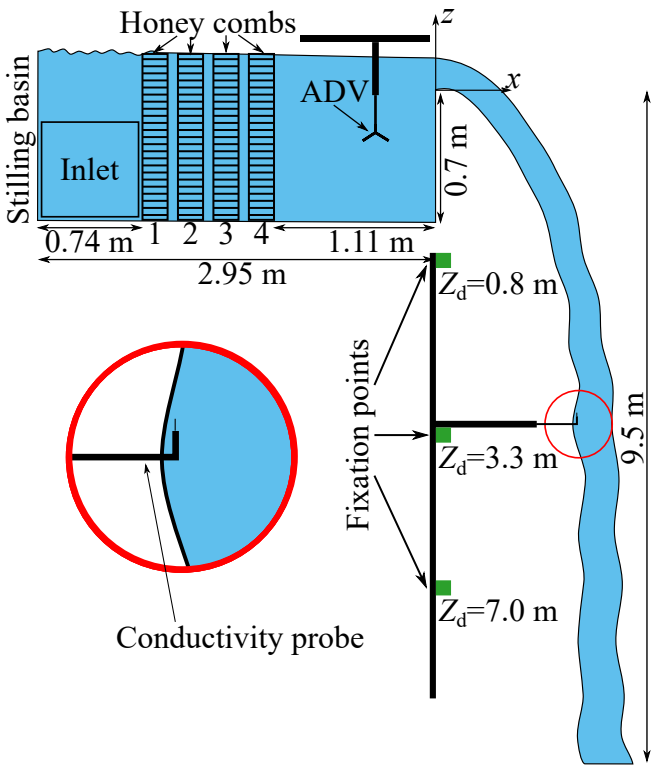

Fig. 5.1. Experimental model setup for investigating nappe widening of the EDF laboratory at Chatou (Fig. 1.2).

Fig. 5.1 shows the model setup at the laboratory of EDF which generates a prototype nappe. The experimental setup consists of a 2.95 m long and 1 m wide flume. The water is laterally fed into the flume via a square inlet and calmed down in a stilling basin. After this, the water flows through a setup of honey combs flow straighteners with different mesh sizes. 1,2: 6.4 mm and 3,4: 3.2 mm. All honey combs have the same width of 17.5 cm. The remaining flume has a length of 1.11 m. At the end of the flume there is a sharp-crested weir with a height of 0.7 m which generates a nappe with Z_d = 9.5 m. The nappe is fully ventilated due to the open design of the construction. In order to reduce the lateral spread of the nappe, the lateral walls protrude the weir by 0.5 m in x-direction. The investigations are carried out at a volume flow rate of 0.1515 m^3/s. The velocities u, v and w upstream of the weir are measured with a SonTek 16-MHz MicroADV probe. The

ADV measurements were performed by the EDF. The water air distribution of the nappe is measured with conductivity probes by the author.

5.2 Upstream Flow Conditions

Acoustic Doppler velocimeter (ADV) measurements collected by the EDF are used to investigate the upstream flow conditions.

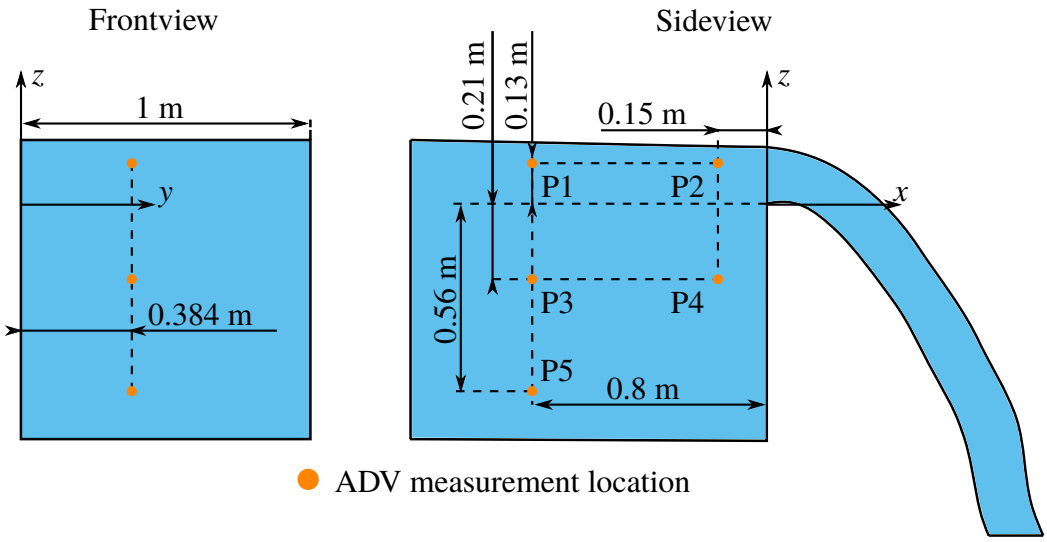

Fig. 5.2. Location of ADV measurements at the upstream flow situation.

Fig. 5.2 shows the locations of the ADV measurements. The measurements are carried out at 25 Hz over a measuring time of 90 s. For P2 the velocity signal is further investigated and the results are shown in Fig. 5.3.

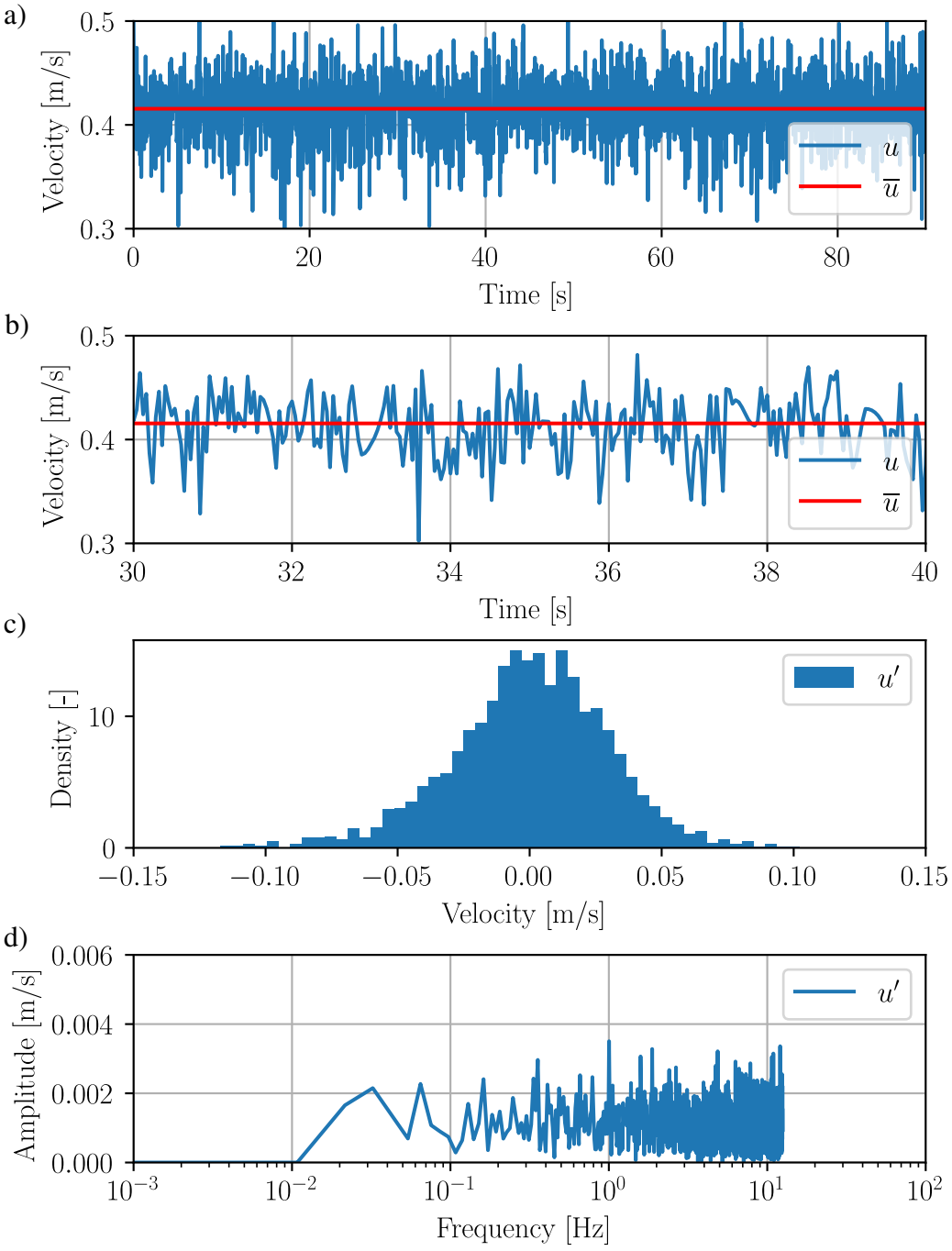

Fig. 5.3. Velocity data at P2 (Fig. 5.2). Velocity in x-direction u and average velocity in x-direction $\overline{u}$ (a), (b), distribution of velocity fluctuations u' (c) and a fast Fourier transform of the velocity u' (d).

Fig. 5.3a,b show the velocity in x-direction u and the average velocity in x-direction $\overline{u}$ of P2. A fast Fourier transform of the u velocity signal is given in Fig. 5.3d for quantifying the fluctuations of the velocity, showing frequencies ranging 0.02 Hz ≥ 12.5 Hz with similar high amplitudes.

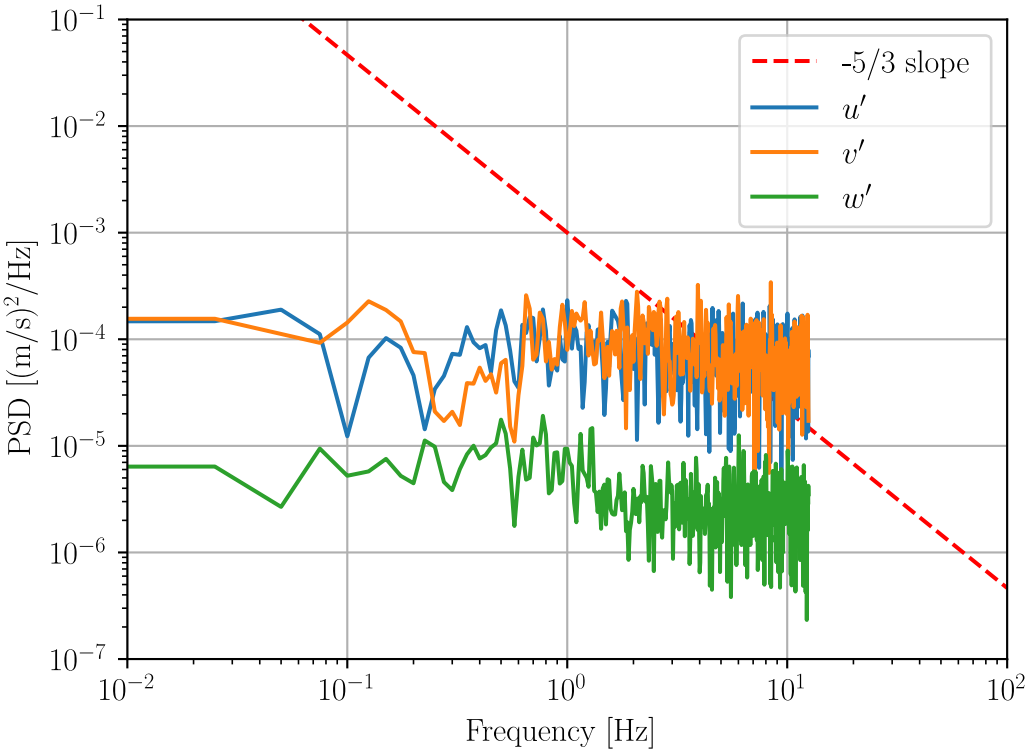

Fig. 5.4. Power spectrum density of the upstream flow situations for P2 (see Fig. 5.2).

The PSD given for P2 in Fig. 5.4 shows a constant power spectrum for u', v', and w' over the whole frequency range of 0.1 Hz ≤ f ≤ 12.5 Hz. For increasing frequency, the power spectra do not follow a $-5/3$ slope, as expected from Kolmogorov's concept for the inertial subrange of turbulence (Kolmogorov, 1991). This indicates that the detected fluctuations of the velocity signal do not have their main origin in turbulence.

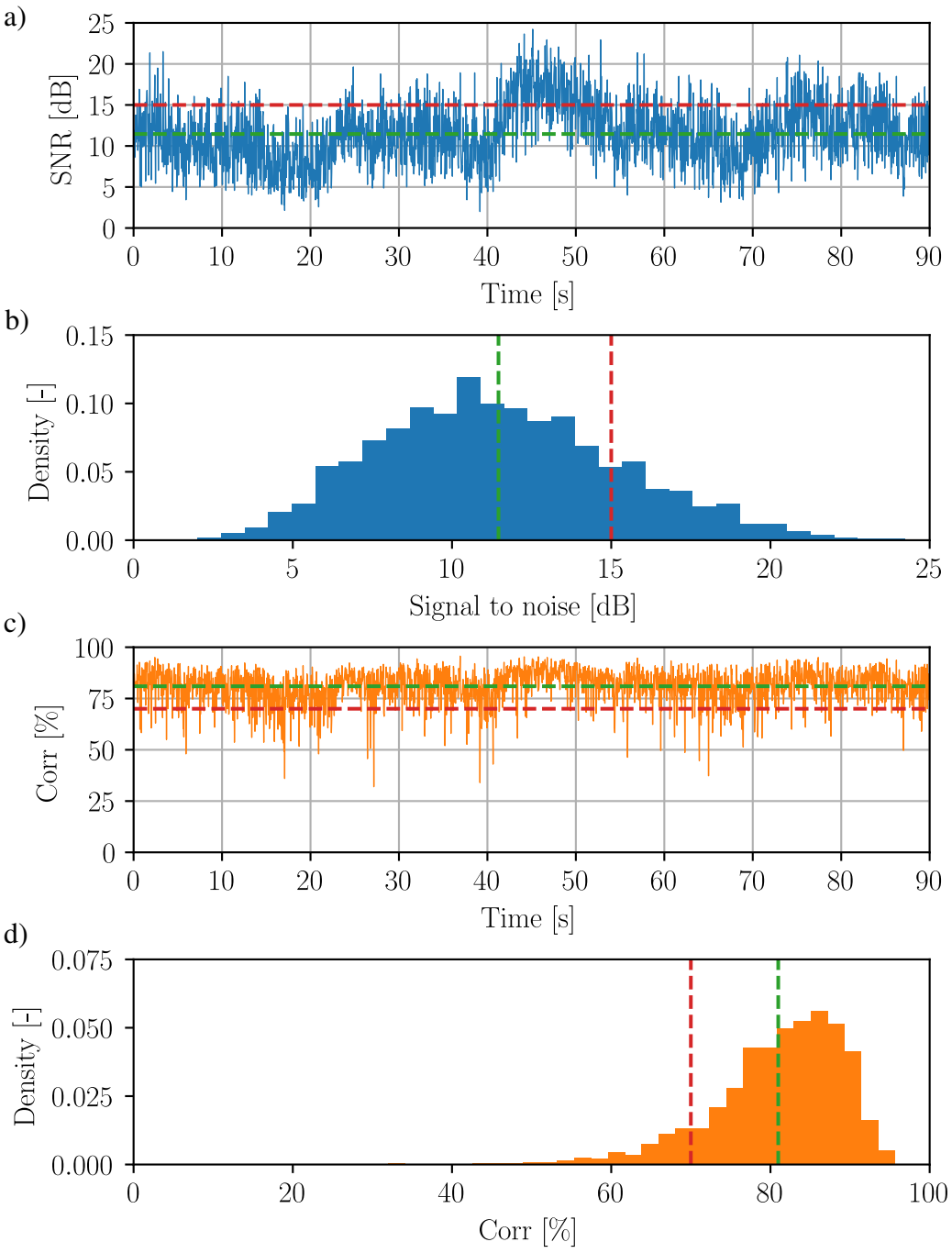

Fig. 5.5. Signal-to-noise ratio (SNR) and correlation (Corr) for P2. Recommendations for SNR and Corr for minimum values in turbulent flows by SonTek (2001) (red dashed lines). Time-averaged values of SNR and Corr (green dashed lines).

Signal-to-noise ratio (SNR) and correlation value (Corr) are quality criteria of ADV measurements, both given by the ADV probe and shown for P2 in Fig. 5.5a,b and Fig. 5.5c,d. The signal-to-noise ratio is in average 11 dB (green dashed line in Fig. 5.5a,b) and is most of the time (82 %) below the recommendation which is SNR > 15 dB for 25 Hz sample rate measurements (red dashed line) (SonTek, 2001). The mean correlation value (green dashed line in Fig. 5.5c,d) is 90 % of the measurement time above the recommended value of Corr > 70 % (red dashed line) (SonTek, 2001). Low signal-to-noise ratios SNR < 15 dB with low correlations Corr < 70 % can origin from insufficient seeding (Sokoray-Varga, 2022), preventing the high frequency part of the turbulent spectrum from being captured. Optimal particle densities for a natural mud are between ~ 1 g/l and ~ 15 g/l for a SonTek 16-MHz MicroADV probe, since correlation falls below 70 % for higher particle densities (Velasco and Huhta, 2010). The PSD of P2 lags the inertial and the dissipative range of turbulence (seen in Fig. 5.4), albeit the Corr value is above 70 % for 90 % of the measurement time. During the measurements, no additional seeding material was added and the water was observed to be quite clear. Velasco and Huhta (2010) show that at very low particle densities (0.1 g/l) the increase in correlation is slightly ahead of the increase in signal-to-noise ratio. Hence, it is estimated that the particle density of the here carried out measurements is << 1 g/l, which means that correlation cannot be used as a sufficient quality criterion.

Computed turbulence intensities will be overestimated due to the high noise level at high frequencies (see Fig. 5.4).

Table 5.1. Mean velocity from ADV measurements at P1-5 (see Fig. 5.2).

Probe	x [m]	y [m]	z [m]	$\overline{u}$ [m/s]	$\overline{v}$ [m/s]	$\overline{w}$ [m/s]	$\overline{U}$ [m/s]
P1	-0.8	0.384	0.13	0.23	0	0	0.23
P2	-0.15	0.384	0.13	0.42	0	0.05	0.42
P3	-0.8	0.384	-0.21	0.18	0	0	0.18
P4	-0.15	0.384	-0.21	0.16	0.03	0.12	0.20
P5	-0.8	0.384	-0.56	0.13	0	-0.01	0.13

Table 5.1 gives the mean velocities $\overline{u}$, $\overline{v}$, $\overline{w}$ and the resulting velocity $\overline{U} = \sqrt{\overline{u^2} + \overline{v^2} + \overline{w^2}}$ for P1-5. P4 shows the influence of the weir, which diverts the

flow towards the z-direction.

Turbulence intensity I_{exp} is computed by

$$I_{\text{exp}} = \frac{\sqrt{\frac{1}{3}(\overline{u'^2} + \overline{v'^2} + \overline{w'^2})}}{\sqrt{\overline{u^2} + \overline{v^2} + \overline{w^2}}} \tag{5.1}$$

and given in table 5.2.

Table 5.2. Turbulent intensity I_{exp} computed from upstream ADV measurements. See Fig. 5.2 for probe locations.

z [m]	x [m]	
	-0.8 m	-0.15 m
0.13 m	P1: I_{exp} = 7.9 %	P2: I_{exp} = 4.4 %
-0.21 m	P3: I_{exp} = 13.5 %	P4: I_{exp} = 11.4 %
-0.56 m	P5: I_{exp} = 16.1 %	

Turbulence intensity I_{exp} shows a high gradient in horizontal direction for z = 0.13 m (P1,2) which results from the acceleration of the flow at the weir. In vertical direction for $x = -0.8$ m there is an increase in turbulent intensity I_{exp} for decreasing z, contrary to an increase in velocity $\overline{U}$ for increasing z (shown in table 5.1).

An approximately constant noise of the measurement at lower mean velocities $\overline{U}$ could lead to higher computed turbulent intensities I_{exp}. The spatial averaged turbulence intensity, for simplicity reasons also called I_{exp}, at $x = -0.8$ m equals 12.5 %.

The measured turbulent intensities are generally very high regarding that the flow has already passed a stilling basin and three honey combs (see Fig. 5.1).

Fig. 5.6 shows the autocorrelation of the magnitude of temporally averaged velocity fluctuations $U' = \sqrt{\overline{u'^2} + \overline{v'^2} + \overline{w'^2}}$ for P1-5. The integral time scale is calculated according to the first zero crossing of the correlation function and the integral length scale is calculated with the mean velocity $\overline{U}$. P1-4 have integral time scales of 0.02 s $\leq T_{\text{i}} \leq$ 0.04 s which are at the limit of the measurement frequency with 25 Hz. The longest integral length scale is seen for P5 with T_{i_5} = 0.1 s. Integral length scales range from P3 = 7.01 mm to P5 = 12.77 mm. P1 is the only one

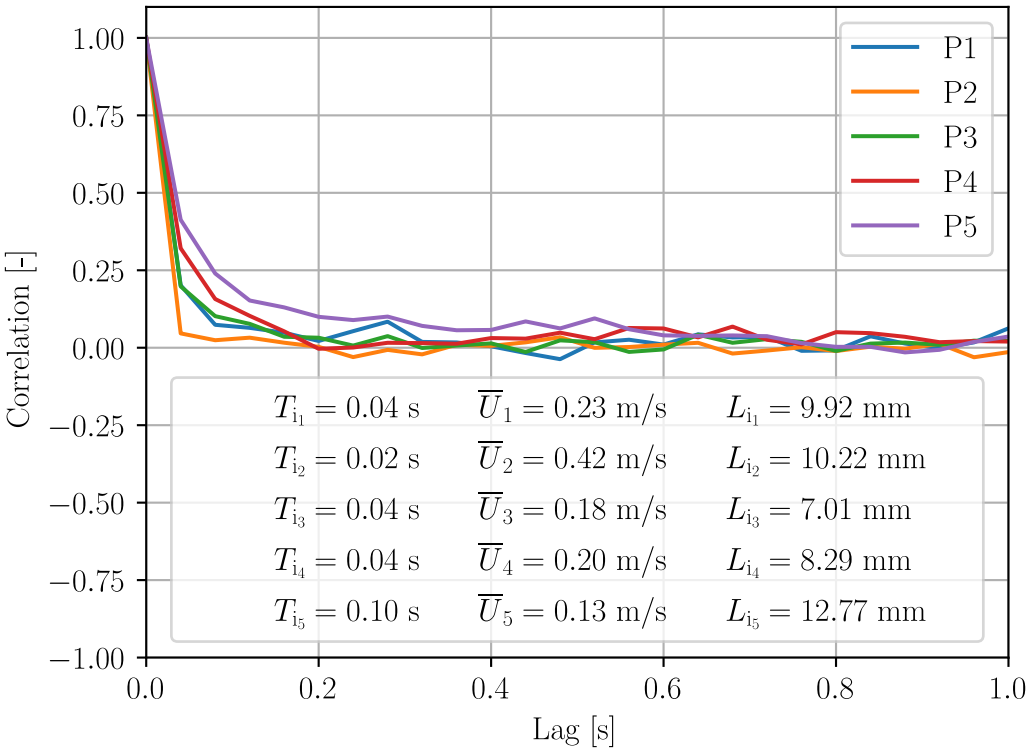

Fig. 5.6. Autocorrelation of the magnitude of temporally averaged velocity fluctuations U'. Integral time scales calculated according to first zero crossing of the correlation function. Integral length scales calculated with the mean velocity $\overline{U}$.

showing periodicity with small correlation values of 0.1 and a period length of 0.2 s.

The short integral time scales and the missing or really weak periodicity of the correlation functions reinforce the assumption that a large part of the turbulent structures were not recorded by the measurement and a major part of the signal is noise. The resulting strong overestimation of the turbulence intensity must be taken into account for further considerations. Following the passage through multiple rows of honeycomb flow straighteners, one would typically anticipate a turbulent intensity of approximately 5 % (Eiff 2023).

5.3 Conductivity Probe Design

A single-tip conductivity probe was designed for measuring the void fraction of a free-falling nappe at a drop depth up to 7 m. A measuring system that meets these requirements is not available for purchase and is typically made by the researchers themselves (Lamb and Killen, 1950; Chanson, 1989; Toombes and Chanson, 2007; Thorwarth, 2009; Muñoz-Cobo et al., 2017; Carrillo et al., 2020a,b, 2021). For fiber optical systems, such as those sold by the French company RBI and used by Boes (2000); Kramer (2004); Pfister (2007); Florez et al. (2016); Guyot et al. (2016), it is uncertain whether sediment containing high-velocity flows damage the polished surfaces of the probe tip. For this reason, no fiber optical measuring methods were used here. The decision to build a single-tip probe over a multi-tip probe was based on three factors. Firstly, it was expected that the probe tip would experience significant loads, so a thicker tip was chosen, which created uncertainty about whether trailing probe tips would be significantly affected. Secondly, the main interest of the conducted measurements was to gather information regarding the water-air distribution within the nappe. For this purpose, a single-tip probe is sufficient. And thirdly, since the probes were built at prototype level by the author with a limited budget, it was important to choose a design that was cost-effective and easy to construct.

The design of the probe and the instrumentation of the signal amplification are based on the system used by the Aachen University of Applied Sciences (FH Aachen) (e.g. Bung, 2011) (manufactured at IWW, RWTH Aachen).

The dimensions of the probe tip which was constructed at The Federal Waterways Engineering and Research Institute (BAW) are shown in Fig. 5.7. The probe tip was obtained through the company Science Products GmbH. The outer electrode of the tip has a diameter of 0.558 mm and is made of stainless steel. The inner electrode has a round-shaped tip with a diameter of 0.225 mm and is made of platinum-iridium, which have proven to be suitable to resist corrosion effects and are used by Chanson (1993, 1997); Carrillo et al. (2021), among others. The tip of the probe protrudes 30 mm from the outer tube, which then merges into the probe shaft (not shown) with a diameter of 20 mm. The probe is operated with a supply voltage which, depending on the resistance, leads to a change in the current. This

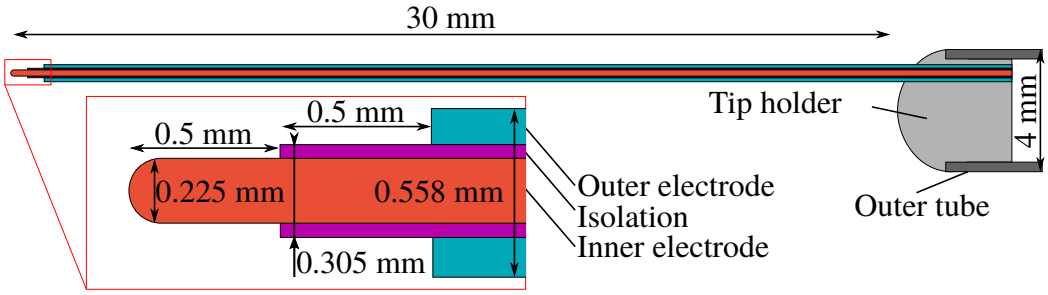

Fig. 5.7. The dimensions of the conductivity probe tip, constructed at The Federal Waterways Engineering and Research Institute (BAW), were utilized for the measurements presented here. Inner electrode made of platinum-iridium. Outer electrode made of stainless steel.

current can then be converted into a voltage via an additional resistor and recorded by an analog-to-digital converter (NI 9239). The signal of the probe is captured with a frequency of 50 kHz. This gives a resolution of 0.24 mm for an estimated flow velocity of 12 m/s. Previous investigations by Carrillo et al. (2020a,b, 2021) of a nappe with a fall height (from energy line to dissipation basin water surface) of 1.7 m where maximal velocities of $\sim$ 5.5 m/s are expected used a sampling rate of 20 kHz.

Fig. 5.8 shows the noise level of the probe while the tip is in air (a) and fully submerged inside the core of the nappe (b) at the laboratory of EDF at Z_d = 0.8 m (see Fig. 5.1). The upstream flow and the nappe at Z_d = 0.8 m were free of air bubbles (visually observed). The mean signal in air is 3.985 V with less than 0.005 V variation and in water 0.656 V with less than 0.02 V variation during 100 s measurement time. The noise level is higher in water due to electrochemical reactions which lead to the growth of gas bubbles (oxygen and hydrogen) at the tip of the probe in the water phase as the support voltage of the probe tip ($\sim$ 12 V) is above the decomposition voltage of water ($\sim$ 1.2 V). These bubbles influence the measurement signal when not removed by the flow.

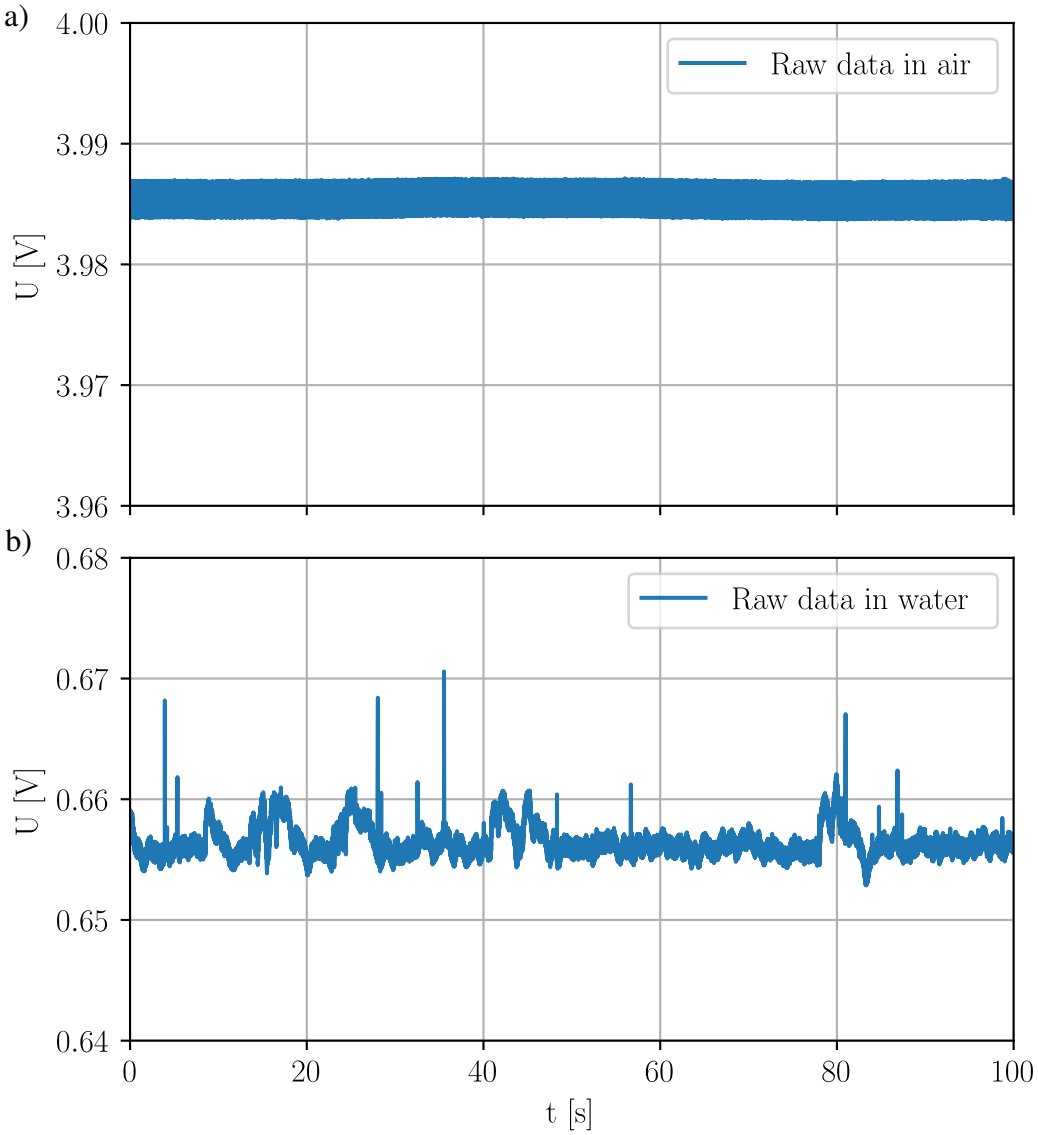

Fig. 5.8. Noise level of the conductivity probe within air (a) and in the core of the nappe at Z_d = 0.8 m (see Fig. 5.1).

5.4 Evaluation Method for Void Fraction Measurements

The measurement method is based on the high difference in electrical conductivity between water and air with air having the much lower electrical conductivity (Herringe, 1973). As long as one of the electrodes is isolated by air, the electrical

circuit is open. When both electrodes are connected by water, the circuit is closed and current can flow between the electrodes. This current can be measured and gives a voltage as the signal of the probe. In the isolated case this voltage corresponds to ~ 4 V and in the case that both electrodes are connected to water ~ 0.66 V.

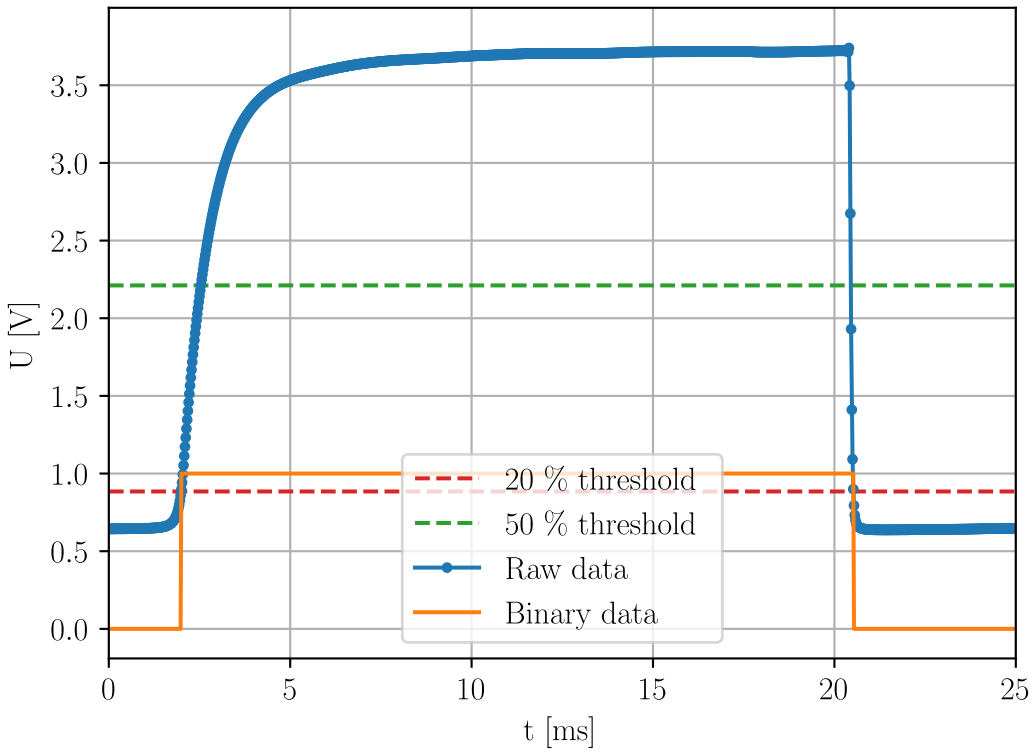

Fig. 5.9. Probe tip drying and wetting process of a phase change event (water-air-water). U is low for probe tip in water. 20 % (red) and 50 % (green) threshold values as possible values for translating raw data (blue dots) with linear interpolation in between to binary data (orange). Here, a 20 % threshold was used.

Fig. 5.9 shows the raw sample signal of the conductivity probe located at the water-air interface of the nappe at the EDF laboratory on a drop depth of Z_d = 3.3 m (blue line) for a full detected phase change cycle from water to air and back to water. The measuring points of the 50 kHz measurement (blue dots) are linearly interpolated. The captured event has a length of about 18 ms. The probe starts submerged in water at ~ 0.66 V. When the probe tip is no longer inside the water phase, the signal starts to increase, first exponentially and after about 9 ms

asymptotically. The signal reaches about 3.8 V before it drops. A drying process of the probe tip is suspected, which continuously increases the electrical resistance between the inner and the outer electrode (see Fig. 5.7). A voltage of 4 V (as seen in Fig. 5.8a) is not reached over the entire measurement period since the exposure time of the probe tip to the air phase is not long enough. Therefore, the maximum and minimum voltage during a measurement is used to calculate threshold values, as described by Wüthrich et al. (2022). 50 % of the voltage difference between water and air is reached after about 1 ms (green level) and 20 % of the voltage difference (orange level) is reached after about 0.5 ms.

The drying process of the probe tip is clearly slower than the wetting process, leading to uncertainty about the actual time of the probe tip in both phases. For distinguishing between water and air, a 50 % threshold method is widely used (e.g. Toombes and Chanson, 2007) (here 2.2 V) (green dotted line Fig. 5.9). Published raw data signals of conductivity probes (e.g. Thorwarth, 2009; Carrillo et al., 2020a) show high noise level which could explain the need for such a high threshold. However, since the noise signal of the here used probe tip is very small (20 mV) (compare Fig. 5.8), a 20 % threshold method (here 0.89 V) (red dotted line Fig. 5.9) is used for lowering the influence of the tip drying time without running into the risk of falling below the noise level (see Fig. 5.8b). The resulting binary data are given in Fig. 5.9 (orange line).

Fig. 5.10 shows the sample signal of the conductivity probe located at the water-air interface on a drop depth of Z_d = 3.3 m for a measurement time of 0.2 s.

The detected phase change events differ in length and shorter events have lower maximal voltage level (as described above). However, every detected event has a maximal voltage level that is significantly above the 50 % and 20 % level. For t = 0.075 s there is a situation at which the voltage does not decrease below the 20 % threshold value. Here the connection of the two electrodes through water was not long enough to allow the voltage to drop to the water-voltage-level (0.66 V) and pass the 20 % threshold. Therefore, no phase change is detected within the binary signal.

Resulting from the 20 % and the 50 % threshold values, the frequency density distribution of the detected air phase time is shown in Fig. 5.11 with overlapping bars colored brown, showing large variation of the detected air phase times for

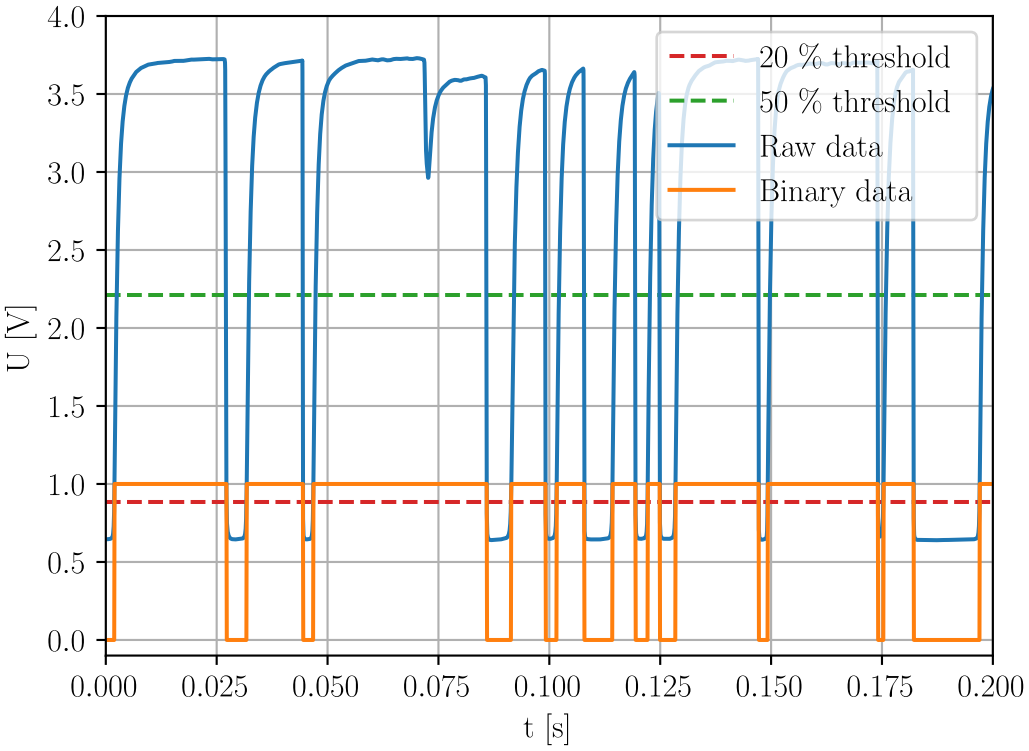

Fig. 5.10. Signal sample of the conductivity probe at Z_d = 3.3 m (blue). Voltage U is low for probe tip in water. 20 % (red) and 50 % (green) threshold values as possible values for translating raw data (blue) to binary data (orange). Here, a 20 % threshold was used.

both threshold values, ranging from 0.06 ms to 5 s. As expected, the detected air phase times shift to longer times for the lower threshold value (20 %), leading to a change in void fraction from 51 % to 55 % for the here investigated position at the water air interface.

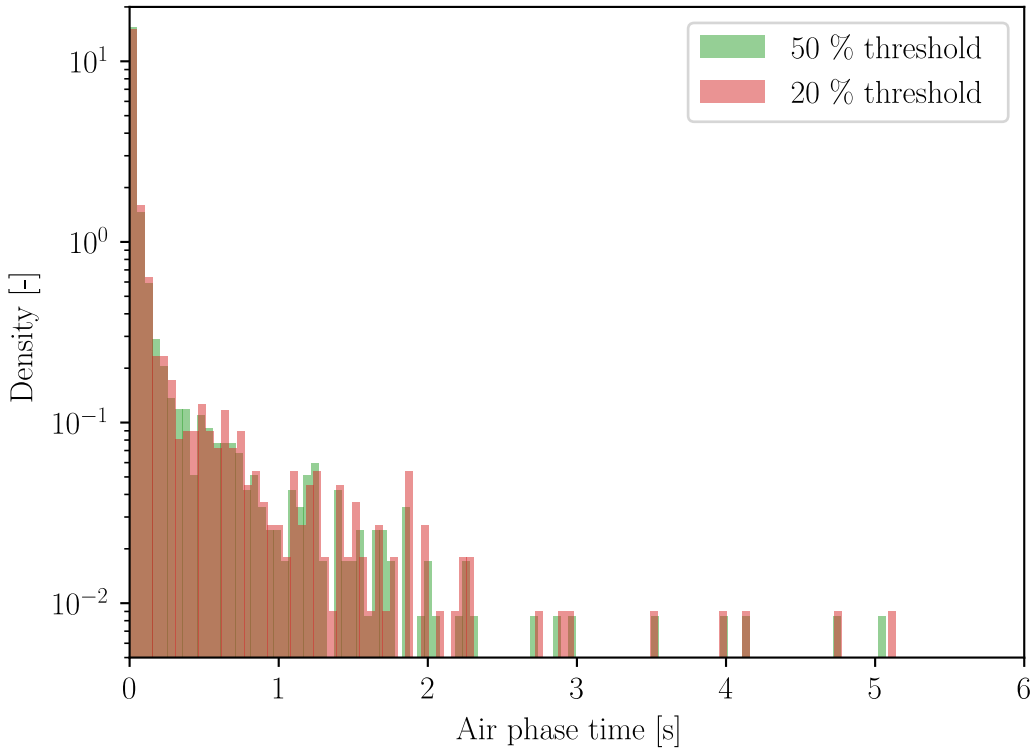

Fig. 5.11. Air phase time distribution for 50 % (green) (here 2.2 V) and for 20 % (red) (here 0.89 V) single threshold void fraction evaluation method at $Z_d = 3.3$ m. Overlapping bars are brown.

5.5 Void Fraction as a Function of Measurement Time Length

The measurement of void fraction is based on temporal averaging the binary signal which indicates weather the probe tip is in water or air. Other investigations of nappes showed that after 30 s a relative uncertainty of about ±1 % in the void fraction was reached for specific volume flow rates ranging 0.048 $m^2/s \leq q \leq$ 0.096 m^2/s with a fall height (from energy line to dissipation basin water surface) of 1.7 m (Carrillo et al., 2020a,b, 2021).

Figs. 5.12a,b,c show the void fraction as a function of the measurement time length for $Z_d = 0.8$ m ($x = 0.62$ m, $y = 0.47$ m), $Z_d = 3.3$ m ($x = 1.2$ m, $y = 0.47$ m) and $Z_d = 7$ m ($x = 1.8$ m, $y = 0.47$ m).

For $Z_d = 0.8$ m the void fraction is about 50 % for a measurement time length

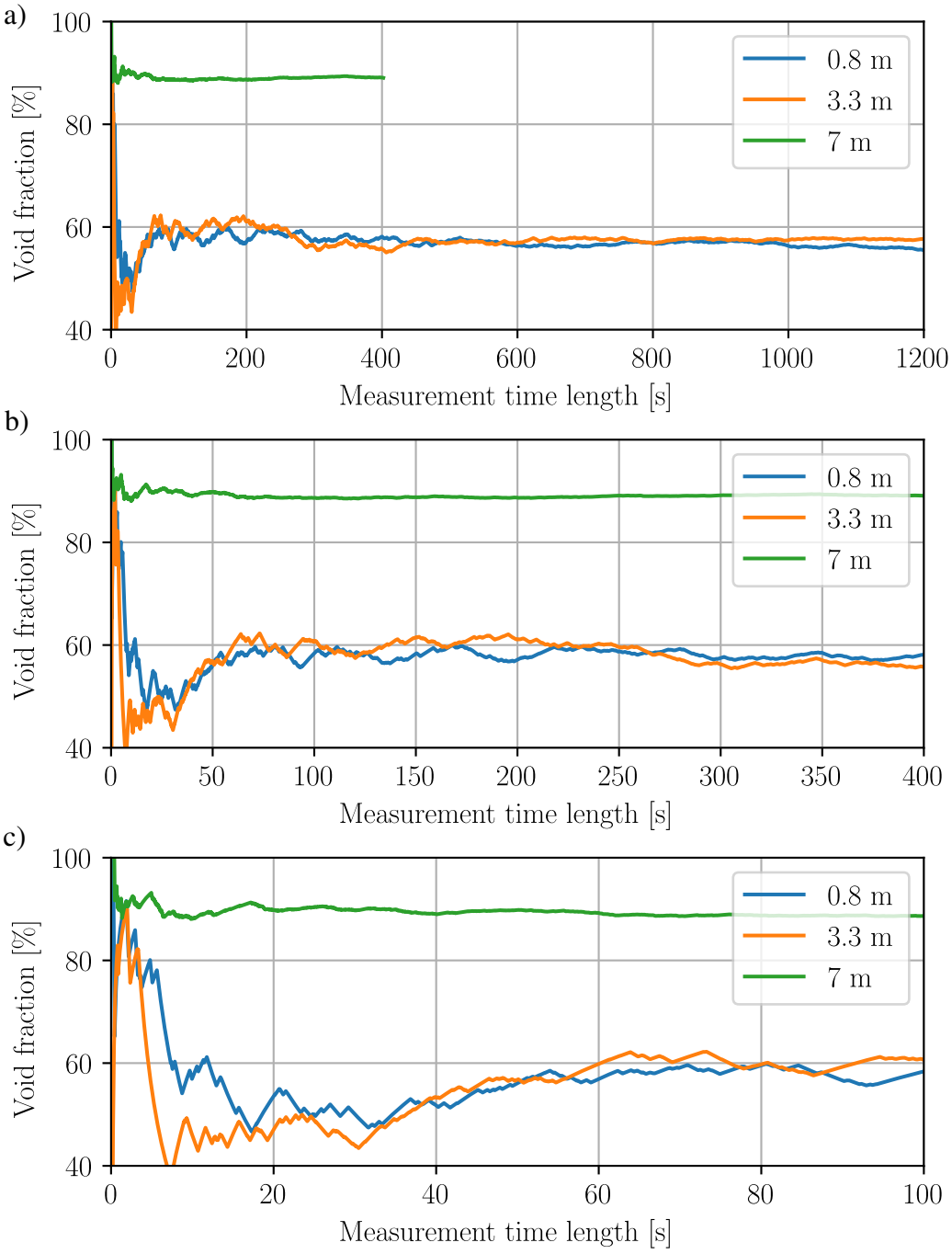

Fig. 5.12. Void fraction as a function of the measurement time length at three different Z_d.

of 30 s, then the void fraction increases up to ~ 60 % for a measurement time length of 100 s. For measurement time length between 100 s and 400 s the void fraction oscillates around 58 %. For measurement time length ≥ 400 s the void fraction approaches ~ 57 % and reaches convergence with less than 2 % difference to the void fraction for a measurement time length of 1200 s. The void fraction at Z_d = 3.3 m shows similar behavior and also reaches convergence for measurement time length ≥ 400 s. The convergence at Z_d = 7 m is much faster than for Z_d = 0.8 m and Z_d = 3.3 m, already reaching after 100 s of measurement time length less than 2 % difference to the void fraction after a measurement time length of 400 s.

With increasing drop depth Z_d the necessary measurement time to reach convergence decreases. An averaging time of 400 s was chosen for every measurement point of Z_d = 0.8 m and Z_d = 3.3 m, resulting for 55 measurement points in more than 6 h pure measurement time for the two nappe profiles. With that, the convergence is within 2 %. At Z_d = 7 m, 100 s averaging time was chosen as the convergence criterion is reached faster, resulting in 0.5 h measurement time for the deepest drop depth nappe profile.

Chapter 6

Experimental Results

The focus of the investigation was on collecting horizontal profiles at three drop depths up to 7 m of the time-averaged water-air distribution of the nappe measured with conductivity probes. The results of this analysis are presented in the first section of this chapter. The second section focuses on a long-term void fraction measurement of the nappe (10 hours) in combination with a volume flow rate measurement, aiding in the identification of the temporal behavior of the nappe. The third section examines the impact of volume flow fluctuations on the trajectory of the nappe, giving insights into the stability of nappe flow in variable flow conditions. The fourth and final section analyses the stability of the boundary layer at the water-air interface, which assists in identifying the factors that influence the stability of the nappe.

6.1 Introduction

6.2 Void Fraction Nappe Profiles

The behavior of a sharp-crested weir nappe was investigated in order to measure its development during the fall. The nappe that was studied had a drop depth of 9.5 m, a width of 1 m, and a volume flow rate of 0.1515 m^3/s which is setup at the laboratory of the EDF (Électricité de France). The aim of the study was to better understand the dynamics of the nappe as it falls, and to obtain detailed data on its horizontal void fraction profiles. To achieve this, conductivity probes were used to measure horizontal void fraction profiles of the nappe. The conductivity probes are highly sensitive instruments that can detect changes in conductivity in the fluid being measured. See section 5.3 for a detailed description of the conductivity probes which were used in this study. For measuring the nappe profiles, the tip of the conductivity probe was aligned with the nappe to reduce lateral forces on the protruding probe tip. The conductivity probe was fixed to a traverse system which allowed the adjustment of the probe in x-direction on three different drop depths Z_d. All measurements were performed with the same conductivity probe.

Fig. 6.1 shows the nappe profiles of the void fraction in x-direction (see Fig. 5.1) at Z_d = 0.8 m, 3.3 m and 7 m over the x-coordinate of the measurement location subtracted by the center of gravity $x_{CG_{exp}}$ of the nappe profile computed by

$$x_{CG_{exp}} = \frac{\sum_i (x_i(1 - C_i)l)}{\sum_i ((1 - C_i)l)} \tag{6.1}$$

with C_i the void fraction of the measurement points interpolated to an equidistant segment length l, since the experimental measurements are made on horizontal lines through the nappe in x-direction.

The nappe profiles differ in shape whereas the slope of the transition from high void faction areas (at the rim of the nappe) to low void fraction areas (in the center of the nappe) becomes flatter with increasing drop depth Z_d. Further, the bottom side of the nappe which faces the weir ($x - x_{CG_{exp}} < 0$) shows a higher slope for Z_d = 7 m.

Carrillo et al. (2020a,b, 2021) define the nappe boundary to be at 90 % void

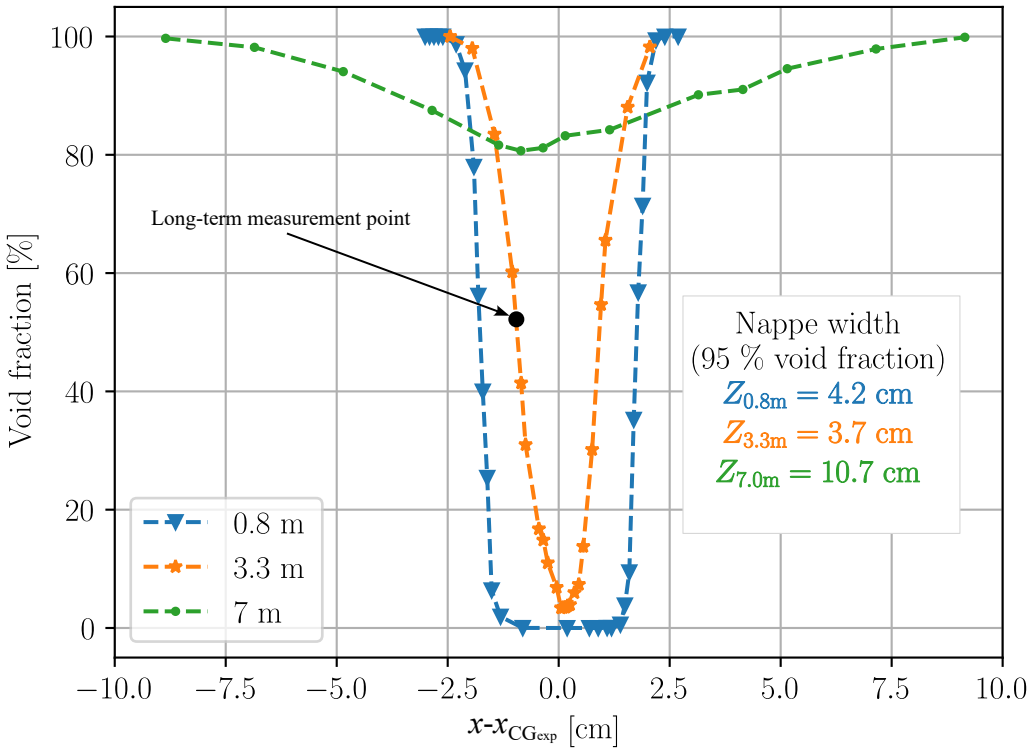

Fig. 6.1. Nappe profiles of investigated Z_d. Center of gravity calculated on the horizontal line through the nappe at each drop depth based on the measured void fraction distribution (Eq. 6.1).

fraction. However, the void fraction of the here investigated nappe continuous to increase with a similar gradient for void fractions < 95 %. Especially for Z_d = 7 m, the definition of the nappe boundary to be at 90 % void fraction is not useful, since this would neglected a large part of the outer rim of the nappe. Hence, the lateral widths of the nappe is evaluated here by defining the nappe boundary to be at 95 % void fraction where the void fraction gradient decreases. The resulting nappe widths are also given in Fig. 6.1.

Accordingly, at Z_d = 0.8 m the nappe has a lateral width of 4.2 cm with an area of zero void fraction in the center of the nappe, showing the core region of the nappe. For Z_d = 3.3 m, this core does not exist any longer. The lowest void fraction that can be found is 3.4 %. The lateral nappe width at Z_d = 3.3 m narrows down to 3.7 cm. At Z_d = 7 m, the lateral nappe width increases again to 10.7 cm. The minimum void fraction at Z_d = 7 m is 80.7 %. The strong diffusion of the

nappe matches the observations made on site and suggests that aerodynamic effects become significant at this drop depth in combination with the investigated specific volume flow rate of 0.1515 m^2/s.

6.3 Long-Term Void Fraction Measurement

A 10 hour long measurement of the volume flow rate and the void fraction at drop depth Z_d = 3.3 m at the water-air interface (on the bottom side of the nappe which is closer to the weir, see Fig. 6.1) is performed. The two measurements are synchronized by hand. At the time the long-term measurement was started, the model was already running for ~ 5 h.

For evaluating the void fraction a moving mean of 400 s (see section 5.5) is used. The volume flow rate is measured with 10 Hz and averaged with a 10 s moving mean to reduce noise.

By superimposing both measurements, as shown in Fig. 6.2a,b,c, a dependency becomes apparent which shows that an increase in volume flow rate leads to an increase in void fraction.

Fig. 6.3a shows that the volume flow rate changes by less than 1 % relative to the mean volume flow rate of 151.5 l/s during the measurement time of 10 h. The variation of the void fraction, which is shown in Fig. 6.3b, reveals changes of about 26 % in absolute terms during the measurement time. Furthermore, a main peak at 54 % void fraction and a second peak at 50 % void fraction can be seen. The frequency composition of the volume flow rate signal and the void fraction signal are shown in Fig. 6.3c by fast Fourier transforms (FFT), which reveal that both signals share a wide range of frequencies with four frequencies (period lengths) being particularly noticeable. A: $1.2 \cdot 10^{-4}$ Hz (2.3 h), B: $2.5 \cdot 10^{-4}$ Hz (1.1 h), C: $6 \cdot 10^{-4}$ Hz (27 min) and D: $1.2 \cdot 10^{-3}$ Hz (14 min) which are some of the harmonics of the fundamental frequency (A). This indicates that all frequencies have the same origin, which is assumed to be the water level of the model's deep tank system due to the long period duration of the oscillations. Water level fluctuations result in pump performance fluctuations and hence in fluctuations of the volume flow rate, since a static bypass system is used for controlling the volume flow rate.

An influence on the volume flow rate through a change in the void fraction is

excluded at this point. Instead, the cause of a changing nappe trajectory is examined in the following.

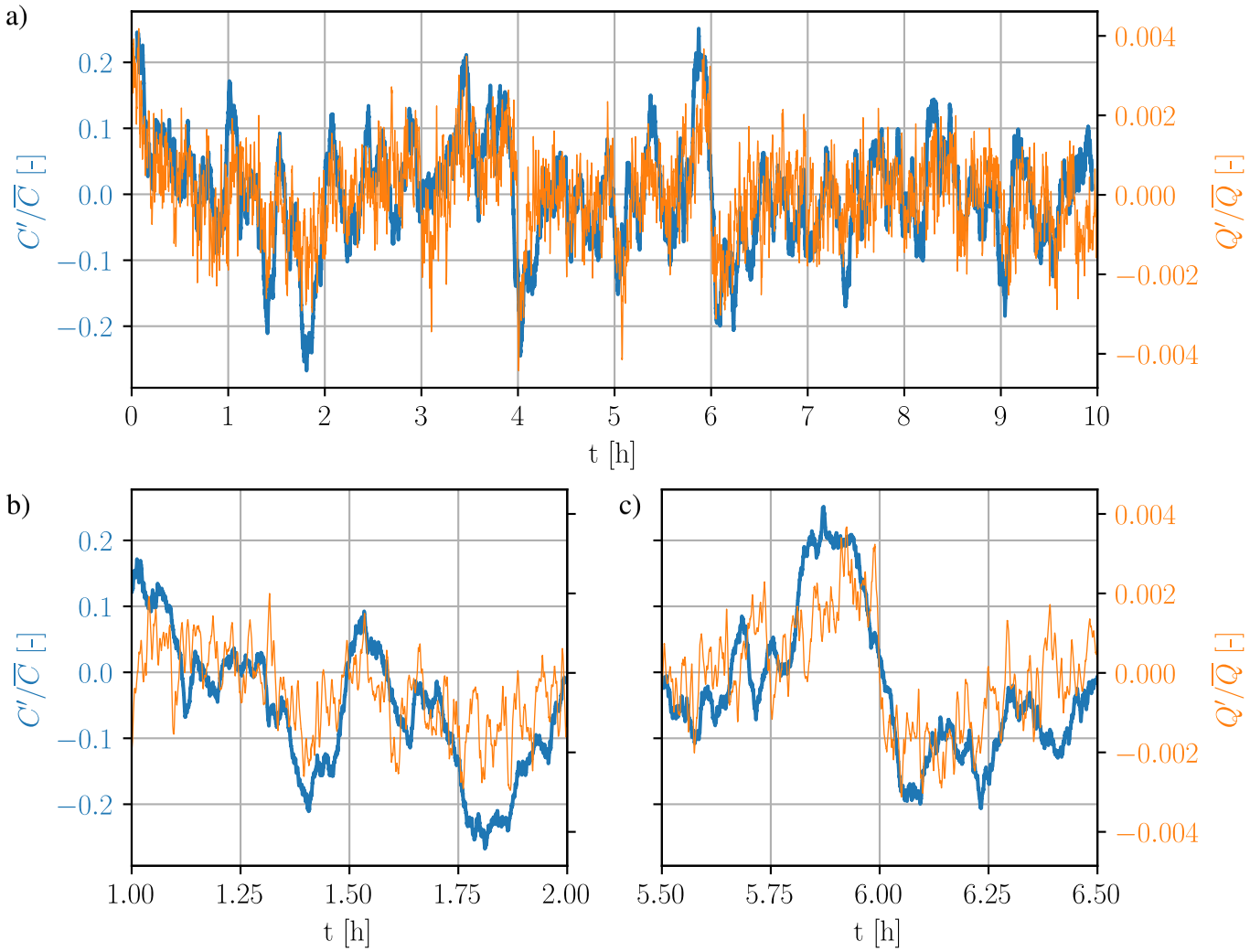

Fig. 6.2. 10 hour measurement of void fraction and volume flow rate (a). Zoom to time interval 1 h $\leq t \leq$ 2 h (b). Zoom to time interval 5.5 h $\leq t \leq$ 6.5 h (c).

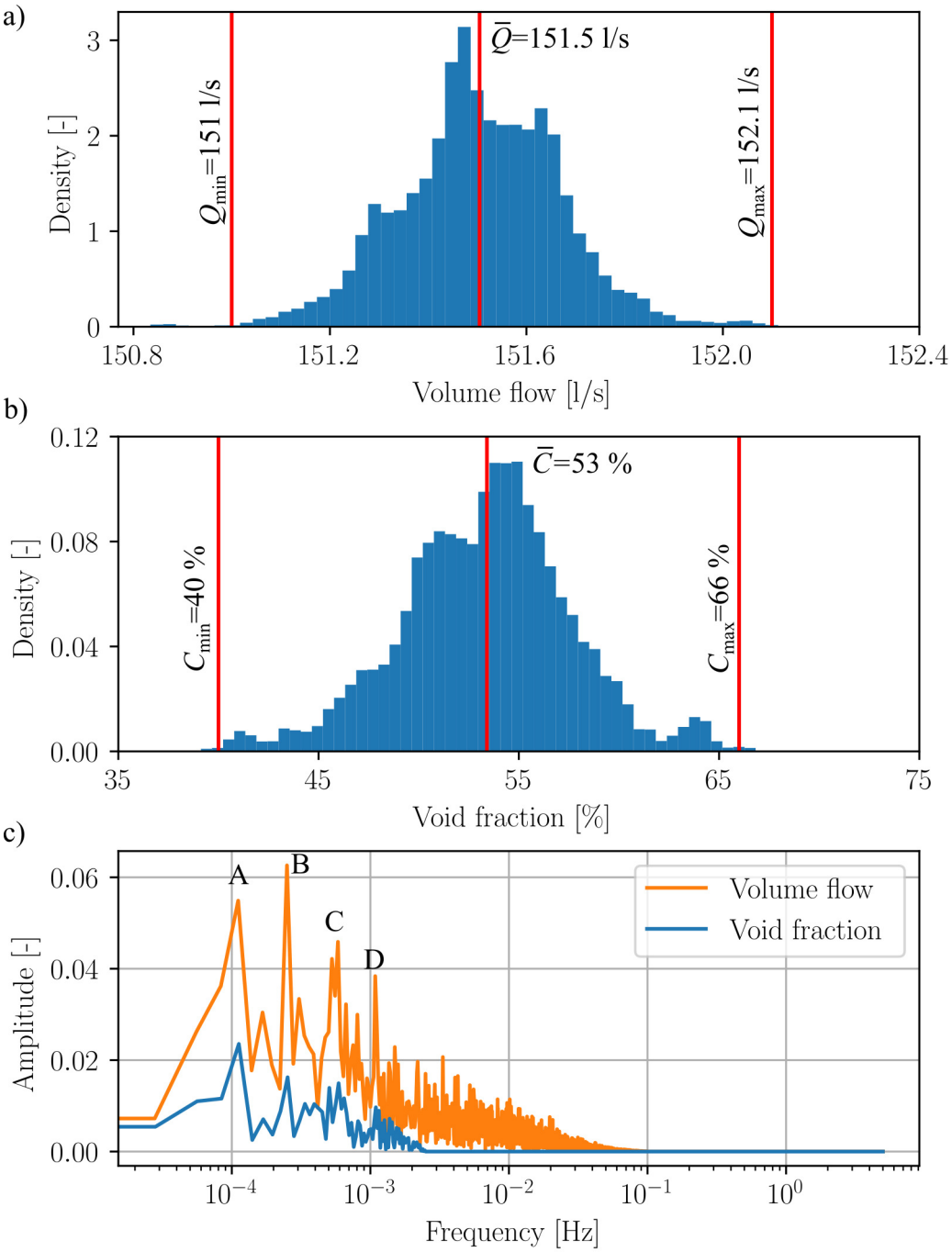

Fig. 6.3. Frequency density distribution of volume flow rate (a). Frequency density distribution of void fraction (b). Fast Fourier transform of volume flow rate and void fraction (c).

6.4 Influence of Volume Flow Fluctuation on Nappe Trajectory

All experimental investigations were performed for a volume flow rate of $\overline{Q}$ = 151.5 l/s, which is, however, subject to fluctuations (as seen in section 6.3) of ~ 0.7 %. This is usually acceptable for hydraulic models and is in the range of the accuracy of Magnetic-inductive flow meters (MID). However, the small fluctuations in volume flow rate result in a fluctuating head water level, which has an impact on the nappe trajectory. The position of the bottom side of the nappe trajectory can be calculated according to the empirical formulation of Scimemi (1937), also mentioned by Hager (1987):

$$\frac{Z_d}{H} = 0.5 \left(\frac{x_w}{H}\right)^{1.85} \tag{6.2}$$

with H the headwater level and x_w the horizontal distance between weir and lower nappe surface as defined by Fig. 6.4.

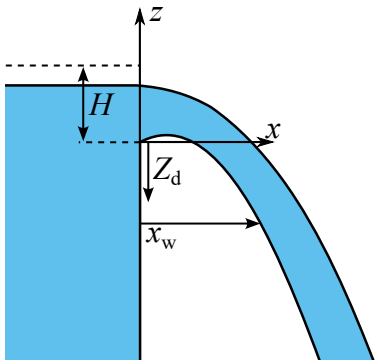

Fig. 6.4. Definition for calculation of weir to lower nappe trajectory distance by Eq. 6.2.

Since no head water level was measured, a theoretical headwater level is calculated according to

$$Q = \frac{2}{3}\mu\sqrt{2g}B\sqrt{H^3} \tag{6.3}$$

with Q the volume flow, μ the weir coefficient (here μ = 0.63) (Bollrich, 2019), g the gravitational constant, B the weir width and H the headwater level. Combining

Eq. 6.2 and Eq. 6.3 results in Table 6.1 which gives the horizontal distance of the bottom side of the nappe to the weir at Z_d = 3.3 m depending on the volume flow rate.

Table 6.1. Influence of volume flow rate fluctuations on lower nappe trajectory at Z_d = 3.3 m.

Volume flow rate [l/s]	H [m]	x_w [m]	Δx_w [mm]
Q_{min} = 151.0	0.1875	1.2851	-1.3
$\overline{Q}$ = 151.5	0.1879	1.2864	0
Q_{max} = 152.1	0.1884	1.288	1.6

The values for the volume flow rate are the same as the extreme values seen during the 10-hours measurement (Fig. 6.3a). The expected variation for weir-to-nappe distance by Eq. 6.2 for the changes in volume flow rate is 2.9 mm in total.

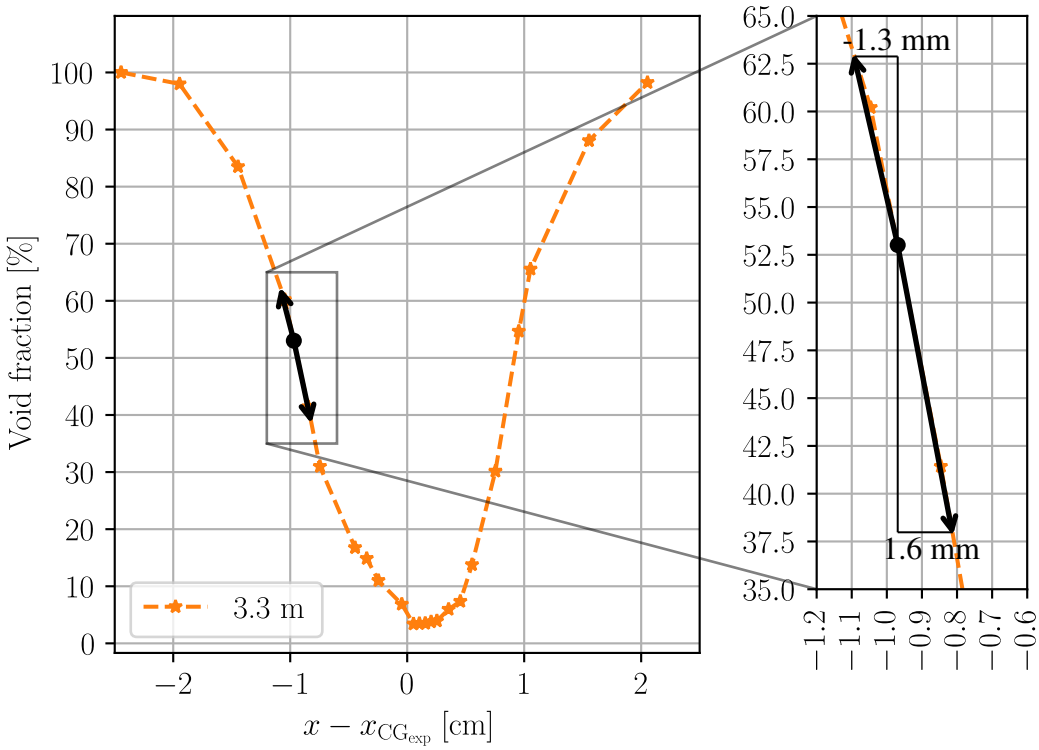

Fig. 6.5. Nappe profile for Z_d = 3.3 m. Arrows show possible displacement of the nappe due to the fluctuation of the volume flow (see Table 6.1).

The expected variation in the nappe-to-weir distance is included into the nappe

profile for Z_d = 3.3 m and shown in Fig. 6.5. The black arrows show a possible displacement of the nappe by -1.3 mm respectively 1.6 mm in x-direction due to the fluctuation of the volume flow rate by 1.1 l/s. The void fraction resulting from the expected change in the nappe position is between ~ 37.5 % and ~ 63.3 % and reflects the changes seen in the void fraction during the 10-hours measurement (see Fig. 6.3b). Therefore, the fluctuation of the volume flow rate as the major cause for the changes in the void fraction is a plausible reason.
The nappe displacements for the three volume flow rates at Z_d = 0.8 m, 3.3 m and 7 m are calculated by using Eq. 6.2 and shown in table 6.2.

Table 6.2. Nappe displacement by volume flow fluctuations. Nappe width (d) for 95 % void fraction (Fig. 6.1). Drop time starts when the nappe passes the weir crest.

Z_d [m]	Drop time [s]	d [mm]	Δx_w [mm]	$\Delta x_w/d$ [%]
0.8	0.4	42	1.4	3.3
3.3	0.8	37	2.9	7.8
7	1.2	107	4.3	4.0

The ratio of $\Delta x_w/d$ increases between Z_d = 0.8 m and Z_d = 3.3 m proportional to drop time and decreases between Z_d = 3.3 m and Z_d = 7 m.
For a nappe that narrows more and more simply because of gravity, the influence of the volume flow fluctuation on the nappe width would continue to increase proportional to drop time. Here, however, it can be seen that the influence of the volume flow fluctuation on the nappe width decreases for deeper drop depths, which shows that the nappe width at deeper drop depths is influenced by an additional effect.

6.5 Stability of the Boundary Layer at the Water-Air Interface

Fig. 6.6 shows the nappe diagonally from the front. At $Z_d \approx 3$ m the experimental nappe changes in its characteristic: horizontal waves start to form at the central area of the nappe with wave length of about 5 cm (Fig. 6.6b). These waves become more intense with deeper drop depths Z_d.

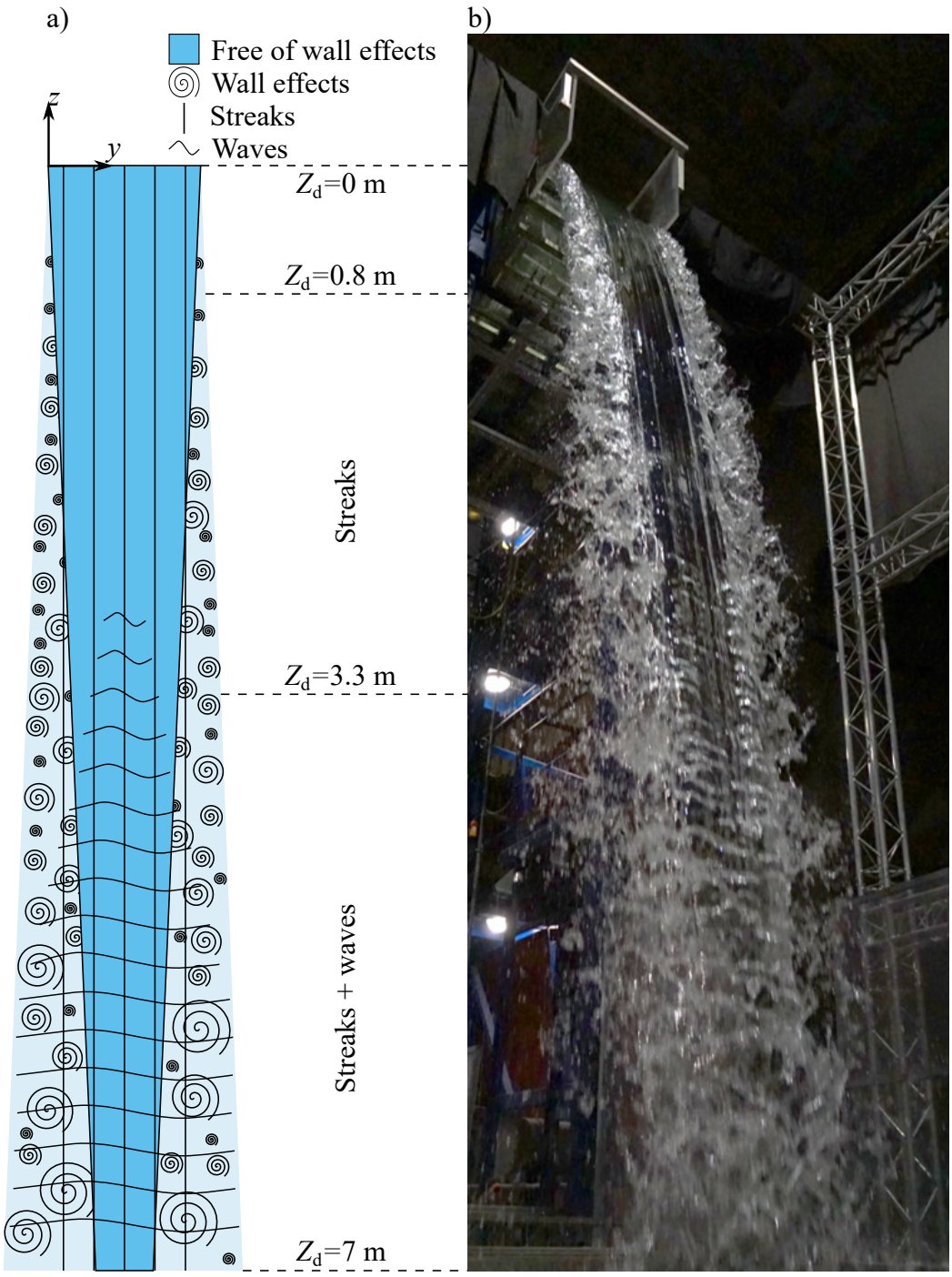

Fig. 6.6. Experimental investigated nappe with a volume flow rate of 151.5 l/s. Image taken with a exposure time of 3.125 ms.

The stability of the water-air interface is independent of the density gradient between the phases, since the flow situation of the nappe is not stratified (discussed in section 2.4). Therefore, small disturbances at the interface are only dampened by viscosity and surface tension. Whether the flow situation at the interface is stable mainly depends on the velocity profile, which was shown for a high resolution numerical simulation (cell edge length 0.0868 mm) in Fig. 3.4. However, the Volume-of-Fluid method (VOF) reaches its limits in the physical representation of the interface area as it creates a continuous transition in density and viscosity between water and air. A jump in density and viscosity at the water-air interface is physically correct which results in the velocity profile shown in section 2.9 with a corner point in the velocity profile at the interface. At this point, the velocity cannot be differentiated and hence the velocity profile has no inflection point. Therefore, a Kelvin-Helmholz instability at the water-air interface, is out of the question, as an inflection point in the velocity profile is a necessary criterion (Drazin and Reid, 2004). However, the boundary layer at the water-air interface can become unstable due to viscosity, described by the Orr-Sommerfeld equation.

For the following considerations it is assumed that the water-air interface of the nappe is like a flat plate where the drop depth Z_d equals the cord length x. Assuming a constant nappe velocity of $u = 7$ m/s for a cord length of 2.5 m, the Reynolds number in the air phase based on the cord length equals $Re_{x,\mathrm{a}} = 1 \cdot 10^6$ and for a velocity of $u = 3$ m/s for a cord length of 0.5 m the Reynolds number in the water phase based on the cord length equals $Re_{x,\mathrm{w}} = 1.5 \cdot 10^6$. Both are above the critical Reynolds number $Re_{x,\mathrm{crit}} = 91000$ for laminar boundary layer flows without inflection point (White, 1991).

The boundary layer thickness for laminar flow is calculated by (Pope, 2000)

$$\delta \approx \frac{5x}{\sqrt{Re_x}} \tag{6.4}$$

and gives for the air phase at $Z_\mathrm{d} = 2.5$ m a boundary layer thickness of $\delta_\mathrm{a} \approx 12.5$ mm with $Re_{\delta^*,\mathrm{a}} = 5800$ based on displacement thickness. For the water phase the boundary layer thickness at $Z_\mathrm{d} = 0.5$ m is $\delta_\mathrm{w} \approx 2$ mm with $Re_{\delta^*,\mathrm{w}} = 6000$. Both Reynolds numbers are above $Re_{\delta^*,\mathrm{crit}} \approx 520$ given by White (1991) for laminar boundary layer flows without inflection point. According to this, small

disturbances can be amplified in both phases.

The smallest unstable wavelength is $\lambda_{min} \approx 6\delta$ (White, 1991) which gives $\lambda_{min,a} \approx$ 7.5 cm and $\lambda_{min,w} \approx$ 1.2 cm which are of the order of the seen wave length in Fig. 6.6b.

Therefore, shear instabilities at the nappe surface might be a major reason for the formation of the seen surface waves and for the seen strong nappe widening for 3 m $< Z_d <$ 7 m (Fig. 6.1).

Chapter 7

Comparison of Numerical and Experimental Results

Experimental and numerical investigations are compared concerning the upstream flow situation, showing 10 times longer integral length scales for the numerical investigation. These can be traced back to the different upstream channel setups. The comparison of the nappe development of the numerical and the experimental investigations shows a similar trend for drop depths up to 3.3 m. This is also supported by visual comparison of the derived nappe surfaces from numerical investigations with photos taken from the experimental nappe, showing streaks that run from the weir crest down to the end of the nappe of similar size and length. For deeper drop depths, the experimental nappe widening is significantly stronger compared to the numerical development. This suggests that the continuous narrowing of the nappe core in combination with high velocities increases the influence of aerodynamic resistance at the water air interface, which is not captured by the numerical model. The aerodynamic resistance of the nappe results in the formation of surface waves which significantly promote the nappe widening.

7.1 Upstream Flow Situation

The upstream flow situations of the experimental model setup (Fig. 5.1) and the numerical model setup (Fig. 3.7) diverge considering the different challenges the model setups have to face. While the main aim of the experimental upstream channel setup was to equalize the laterally entering volume flow and reduce the induced turbulence intensity with a stilling basin and a set of honey combs flow straighteners (see Fig. 5.1), the numerical upstream channel setup is designed to force the development of river-like turbulence structures by applying an inlet boundary condition (see section 3.4.5). Albeit both upstream channels have the same width of 1 m, the wall effects (in y-direction) were reduced for the numerical model by applying a slip boundary condition with the idea to model an infinitely extended weir. Both model setups have similar weir height and volume flow rates. Due to the different model setups, there are differences in the integral length scales with length scales of $\sim$ 10 cm for the numerical investigations (see section 3.4.5) and length scales of $\sim$ 1 cm for the experimental investigations (see section 5.2) determined by the geometry of the honey combs flow straighteners.

The differences in integral length sales can also be seen in the fast Fourier transforms (FFT) of the upstream flow situations shown in Fig. 7.1 for P2 ($x = -0.15$ m, $y = 0.384$ m, $z = 0.13$ m) of the experimental investigation and P3 ($x = 0$ m, $y = 0.5$ m, $z = 0.08$ m) of the numerical investigation. The fast Fourier transforms show a wide range of high frequencies with high amplitudes for the experimental upstream flow situation. Fig. 7.2 shows the power spectrum density of the velocity fluctuations u', v' and w' for P3 of the numerical investigation and P2 for the experimental investigation. It indicates that the turbulent kinetic energy of the experimental upstream flow situation is higher for $f > 1$ Hz compared to the numerical upstream flow situation. This is partly as expected because the flow origins from honey combs which shift the power spectrum density towards small structures with higher frequencies, but it has already been discussed in section 7.1 that the lack of seeding during the ADV measurements led to a low signal-to-noise ratio. Therefore, the signal is significantly influenced by noise which has similar appearance as high frequency turbulence in the power spectrum density. However, a constant course of the energy spectrum over f indicates that the high level of

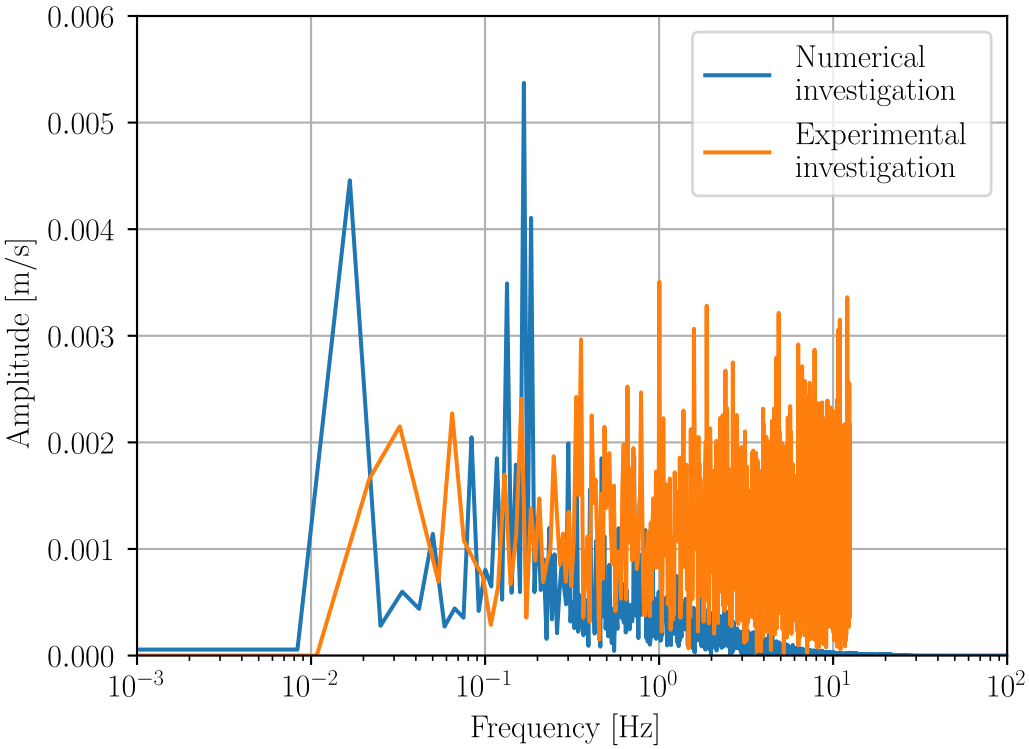

Fig. 7.1. Comparison of the fast Fourier transforms of the upstream flow situations of the experimental investigations (section 5.2) for P2 (see Fig. 5.2) and the numerical investigation (section 3.4.5) for P3 (see Fig. 3.12).

turbulent kinetic energy rather origins from noise than turbulence. For turbulence an inertial range with a slope similar to -5/3 would be expected.

The upstream flow situation of the numerical investigation is periodic in time (see Figs. 3.15, 3.16, 3.17), originating from the cyclic inlet boundary condition with period length of $\sim$ 6 s. A periodicity is not seen for the ADV measurement data, but was visually observed on site by changing nappe detachment with a period length of 1-2 s, showing streaks over the whole nappe length of 7 m (see Fig. 6.6).

The numerical investigations show the formation of long vortex structures close to the weir in flow direction with integral time scales of 0.6 s resulting in integral length scales of 0.7 m at the weir (Fig. 3.16) which are visualized by the Q-criterion in Fig. 4.7a, resulting in the deformation of the nappe surface.

The similarity in time scales of the observed vortex structures suggests that the origin of these structures is independent from the further upstream model setup

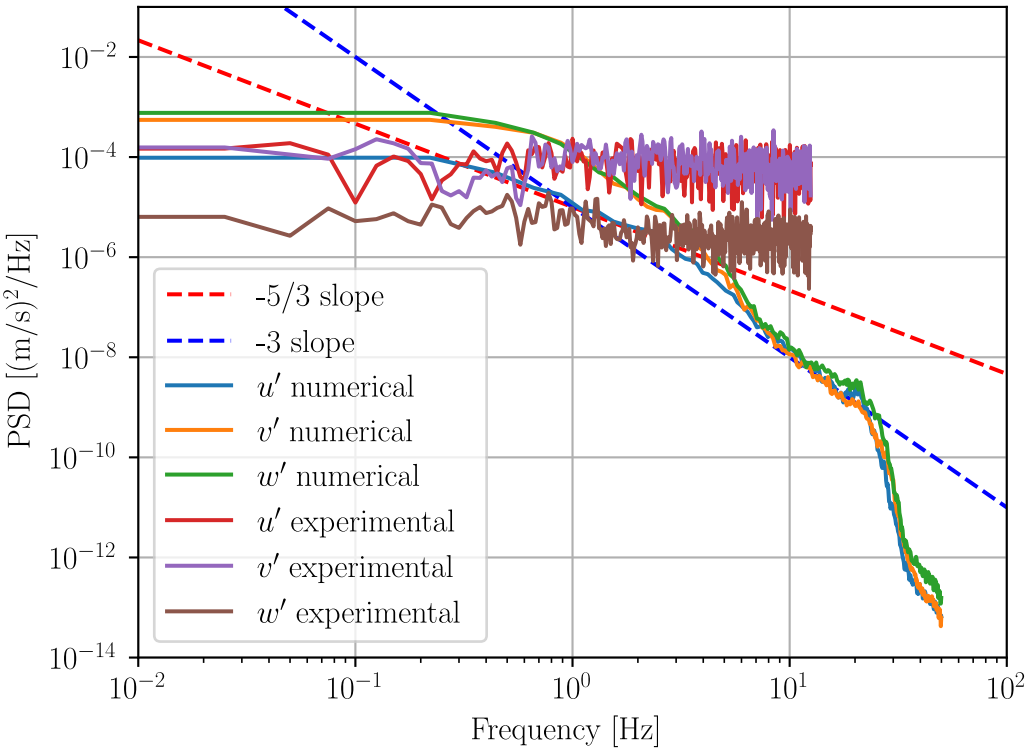

Fig. 7.2. Comparison of the power spectrum density of the upstream flow situations of the experimental investigations (section 5.2) for P2 (see Fig. 5.2) and the numerical investigation (section 3.4.5) for P3 (see Fig. 3.12).

which differs significantly between numerical and the experimental investigations.

7.2 Nappe Development

Nappe development was evaluated on the base of the standard deviation which was calculated for the numerical investigations with Eq. 3.26 and is calculated for the experimental investigations according to

$$\sigma_{\mathrm{exp}} = \sqrt{\frac{\sum_i((1-C_i)l(x_i - x_{\mathrm{CG_{exp}}})^2)}{\sum_i((1-C_i)l)}} \tag{7.1}$$

where

$$x_{\mathrm{CG_{exp}}} = \frac{\sum_i(x_i(1-C_i)l)}{\sum_i((1-C_i)l)} \tag{7.2}$$

is the x-coordinate of the time-averaged center of gravity, C_i the void fractions of the measurement points of Fig. 6.1. The variance is normalized by the total lateral width of the nappe (on the horizontal line) to account for the continuously evolving free-falling nappe.

For comparing the experimental nappe development with the numerical nappe development, the upstream turbulence intensity is evaluated for both at the same distance to the weir ($x = -0.8$ m). The experimental upstream flow situation has a turbulence intensity of $I_{\mathrm{exp}} = 12.5$ % (averaged over the three measurement points P1,3,5, see section 5.2). For the numerical upstream flow situation, the directly captured part of the turbulence intensity I_{d} (Eq. 3.24) is evaluated as an average over the yz-plane. The cutoff length of the LES simulations is $\Delta = V^{1/3} = 6.25$ mm for the upstream flow situation which gives $10 \leq I_{\mathrm{i}}/\Delta \leq 16$ for the integral length scale of v' in y-direction (Figs. 3.18-3.20).

Fig. 7.3 compares the nappe development of the numerical investigations with the nappe development of the experimental investigation (three points indicated by ×). Case 6 comes closest to the experimental upstream conditions with a directly captured turbulence intensity of $I_{\mathrm{d}} = 12.1$ % 0.8 m upstream of the weir, albeit this is not reflected by the development of the experimental investigated nappe at $Z_{\mathrm{d}} = 0.8$ m and $Z_{\mathrm{d}} = 3.3$ m. Here the experimental standard deviation is similar to the lowest numerically investigated nappe with $I_{\mathrm{d}} = 3.5$ %. The progression of the standard deviation of the experimental investigated nappe shows a similar course

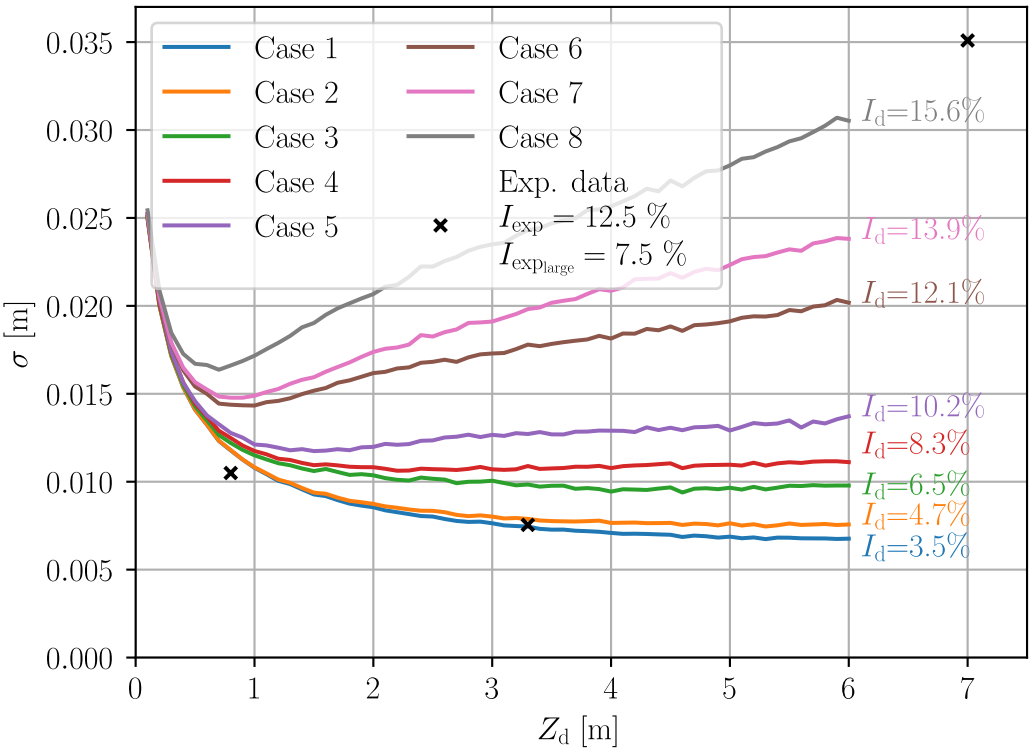

Fig. 7.3. Comparison of experimental and numerical results. Directly captured turbulence intensity I_d (Eq. 3.24) of numerical investigations evaluated 0.8 m upstream of the weir. Experimental turbulence intensity I_{exp} measured 0.8 m upstream of the weir by an ADV probe (see section 5.2) and turbulence intensity $I_{exp_{large}}$ from ADV measurements filtered with low-pass Butterworth filter of 6th order, cutoff frequency = 1 Hz.

as the low-turbulence nappes (Cases 1-3 with I_d = 3.5 % – 6.5 %), monotonic decreasing with drop depth Z_d. As seen in section 5.2 and discussed in section 7.1, the experimental upstream flow situation shows high frequencies with high amplitudes, suggesting that the turbulent kinetic energy resides in small-scale turbulence structures determined by the geometry of the honey combs flow straighteners but most likely origins from noise since no seeding material was added during the ADV measurements, resulting in an overestimation of the turbulent kinetic energy for high frequencies. For Z_d = 7 m, the experimentally determined standard deviation strongly increases and does not follow the expected trend which would be monotonic decreasing (as seen for σ for $Z_d \leq 3.3$ m). Due to the strong widening,

the extrapolation of Case 8 comes closest to the experimental data at this drop depth.

Fig. 7.2) shows that the power spectrum of the numerical flow situation decreases for $f > 1$ Hz while the power spectrum of the experimental flow situation stays on a constant level for increasing f. For reproducing this drop in turbulent kinetic energy for $f > 1$ Hz for the experimental data, the signal is filtered by a low-pass Butterworth filter (Butterworth, 1930) of 6th order with a cutoff frequency of 1 Hz. The filter response as a function of the frequency is shown in Fig. 7.4.

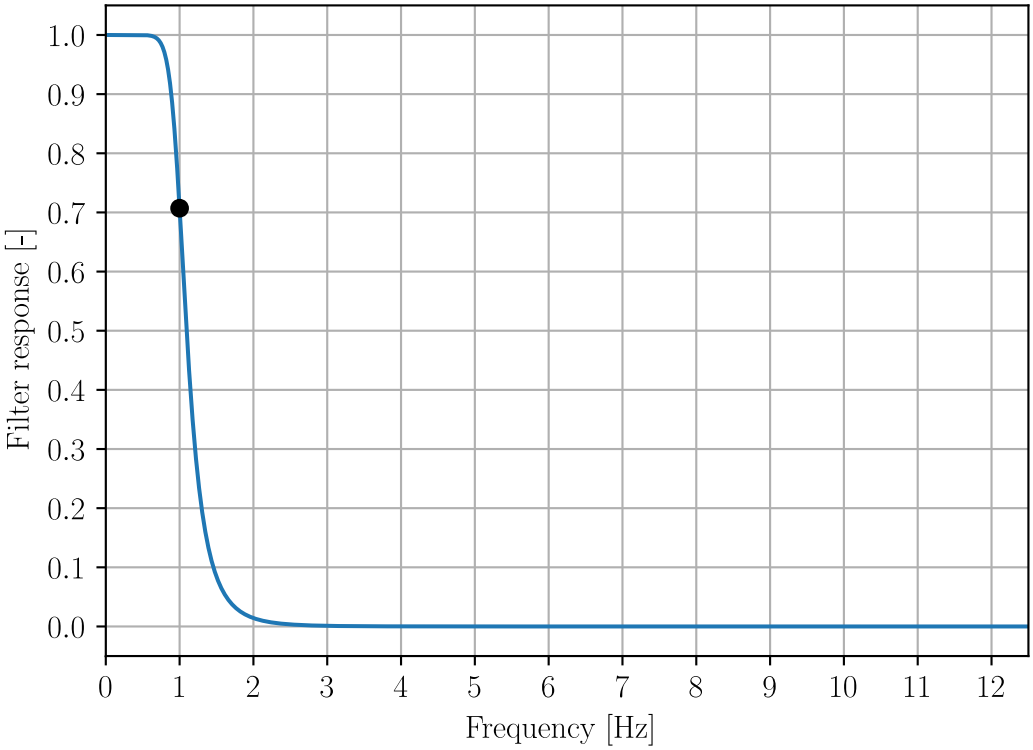

Fig. 7.4. Butterworth filter response for 6th order.

The filter gives a response of 70 % at 1 Hz. The response decreases for higher frequencies and reaches ~ 0 % for $f > 2.5$ Hz. The filter function has nearly no effect for $f < 0.75$ Hz.

The Butterworth filter is applied to the velocity signal of P1,3,5 (see Fig. 5.2). The raw signals and the filtered signals are shown in Fig. 7.5a,b,c. The filtered signals of P1,3,5 have reduced fluctuation amplitudes and frequencies compared to the

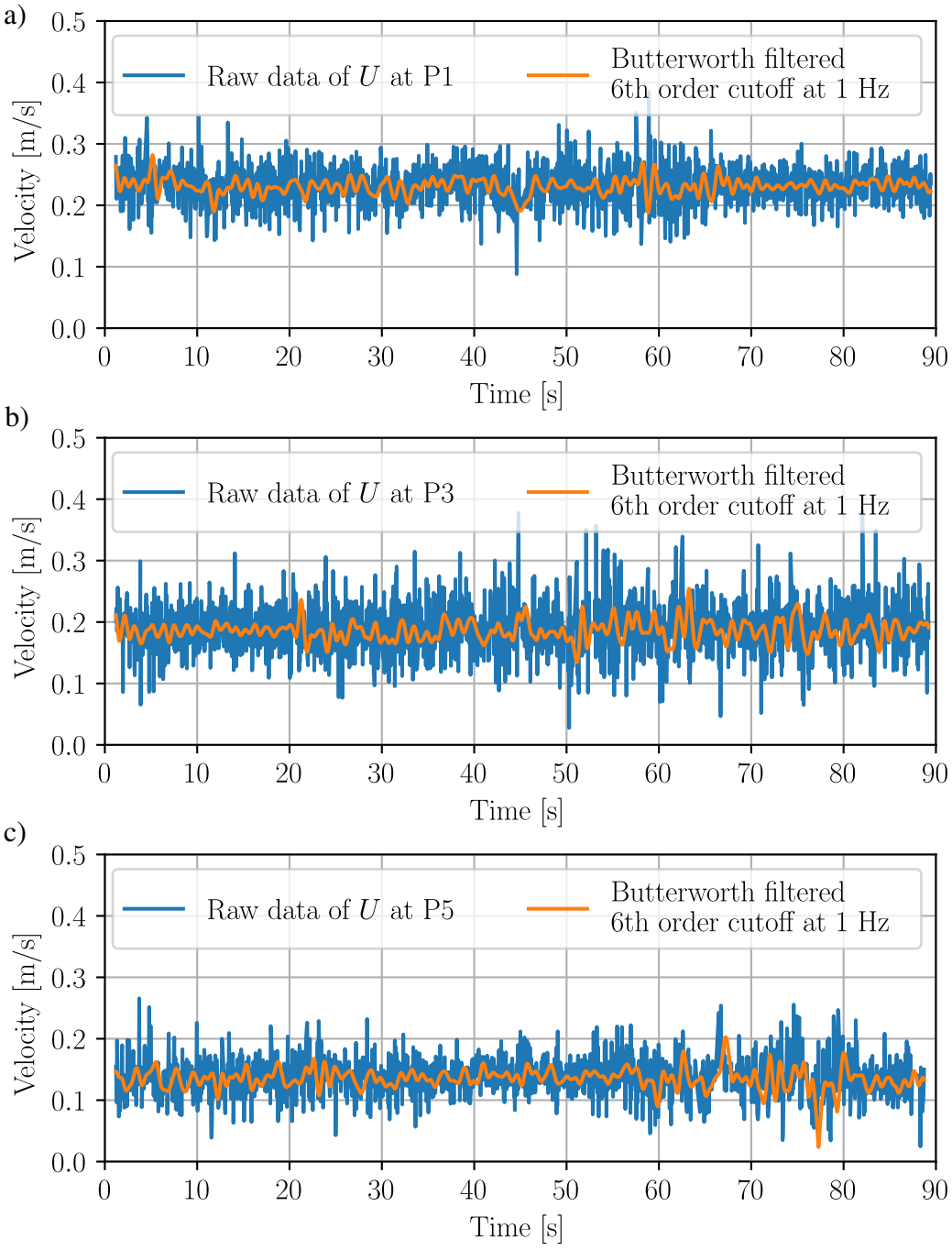

Fig. 7.5. Raw signal of U (blue) and Butterworth filtered signal of U (orange) at P1 (a), P3 (b) and P5 (c). Butterworth filter 6^{th} with cutoff frequency at 1 Hz.

raw signals.

For comparing the filtered velocity signal of the experimental upstream flow situation with the numerical upstream flow situation, the power spectrum density of the filtered signal at P2 is calculated and shown in Fig. 7.6.

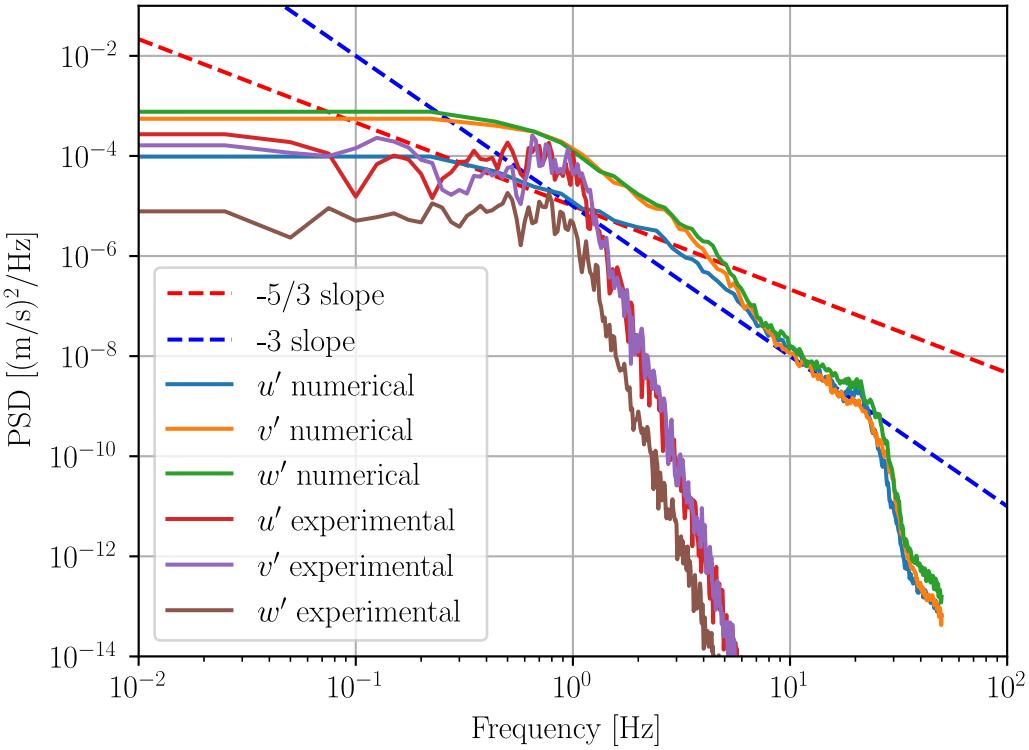

Fig. 7.6. Comparison of the power spectrum density of the filtered signal of the upstream flow situations of the experimental investigations (section 5.2) for P2 (see Fig. 5.2) and the numerical investigation (section 3.4.5) for P3 (see Fig. 3.12).

The filter function leads to a decrease in the power spectra for u', v' and w' for $f > 1$ Hz with a slope significantly steeper than the -5/3 slope indicating the inertial range and the -3 slope indicating the dissipation range.

Fig. 7.7 shows the autocorrelation of the filtered signal U' for P1-5. The integral time length T_{i_i} of the filtered signals are about 10 times longer than the integral time length of the unfiltered signals (shown in Fig. 5.6). The filtered signals show periodicity with period length of about 1 s. The averaged velocities $\overline{U}$ are not effected by the filter function.

The increase in integral length scale and a slightly increase in periodicity show that

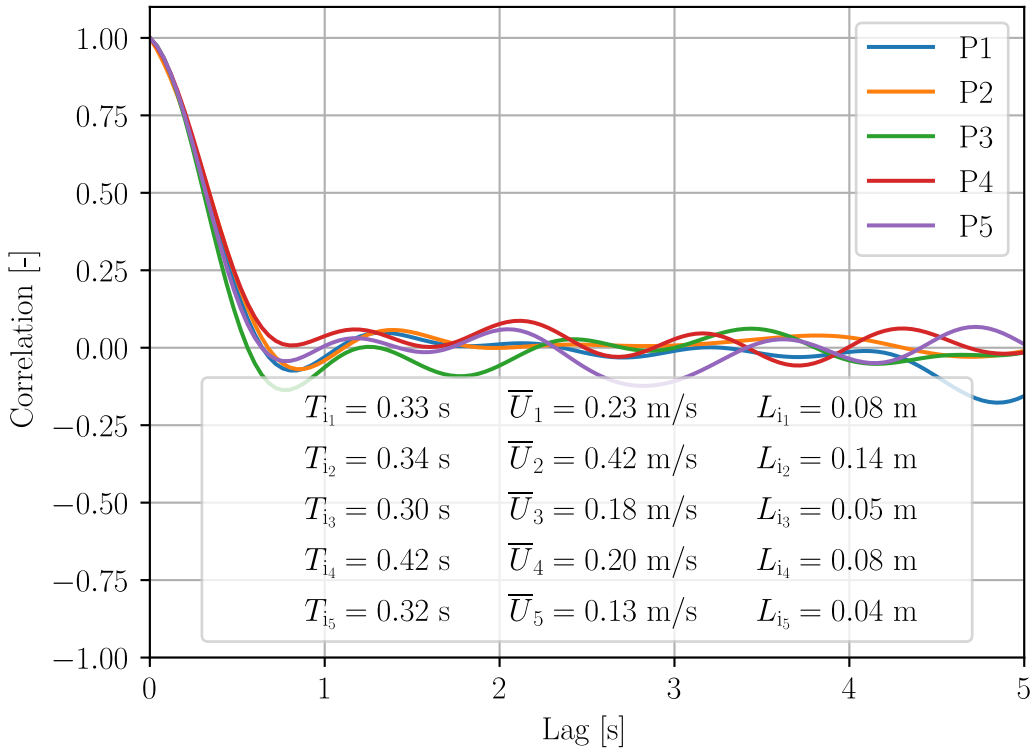

Fig. 7.7. Autocorrelation of the velocity fluctuation U' of the filtered signal. Integral time scales calculated according to first zero crossing of the correlation function. Integral length scales calculated with the mean velocity U.

the filtered signals are less effected by random noise compared to the unfiltered signals (Fig.5.6).

The filtered signal of U is used to calculate large-scale-based turbulence intensity 0.8 m upstream of the weir by

$$I_{\mathrm{exp_{large}}} = \left\langle \frac{\sqrt{\frac{1}{3}(\overline{u'^2} + \overline{v'^2} + \overline{w'^2})}}{\sqrt{\overline{u^2} + \overline{v^2} + \overline{w^2}}} \right\rangle_{\mathrm{(i=1,2,3)}} \tag{7.3}$$

results in $I_{\mathrm{exp_{large}}} = 7.5$ % averaged over P1,3,5. The thus significantly lower turbulence intensity makes the experimental nappe development comparable with the numerical nappe development of Case 4 (Fig. 7.3). Still, a discrepancy exists between the experimental nappe development and Case 4 for $Z_{\mathrm{d}} = 0.8$ m and $Z_{\mathrm{d}} = 3.3$ m which cannot be explained with the difference in the volume flow rate

(numerical investigations: 160 l/s, experimental investigations: 151.5 l/s), albeit larger volume flow rates lead to a higher standard deviation (see section 4.4). An increase of 5 % in volume flow rate results in about 3 % increase in standard deviation (see Fig. 4.9). This would shift the experimental standard deviation for $Z_d = 0.8$ m and $Z_d = 3.3$ m to the level of Case 2 (see Fig. 7.3).

Beside the turbulence-driven nappe widening, the nappe experiences aerodynamic-driven nappe widening which starts to appear at $Z_d = 3$ m for the experimental investigations (section 6.5). The Reynolds number at $Z_d = 3$ m in the air phase is based on the cord length x of the nappe. For $u = 7.5$ m/s the nappe velocity at $Z_d = 3$ m and $x \approx 3$ m this results in $Re_x = 1.5 \cdot 10^5$. By assuming that the nappe surface acts like a wall for the air phase, the dimensionless distance of the mesh to the nappe surface in the air phase is calculated by

$$y^+ = \frac{yu^*}{\nu} \tag{7.4}$$

with ν the kinematic viscosity of air and u^* the friction velocity calculated by

$$u^* = \sqrt{\frac{\tau_w}{\rho}} \tag{7.5}$$

with τ_w the shear stress

$$\tau_w = \frac{1}{2} C_f \rho u^2 \tag{7.6}$$

where C_f the skin friction coefficient for a turbulent boundary layer on a flat plate (White, 1991) is

$$C_f \approx \frac{0.058}{Re_x^{0.2}}. \tag{7.7}$$

Applying Eqs. 7.4-7.7 results for $y^+ = 1$ in $y \approx 0.03$ mm which gives the distance between the nappe surface and the first cell center. The used mesh has a cell edge length of 3.125 mm which gives a dimensionless distance to the nappe of $y^+ \approx 56$. The first cell center is thus in the inertial sublayer where the influence of viscosity is low. Therefore, the mesh is not fine enough to compute the boundary layer instability in the air phase. This suggests, that the numerical model underestimates the nappe development for drop depths of $Z_d > 3$ m for low head water level

(here $\sim$ 0.18 m) which allow aerodynamic effects to become decisive for nappe development.

Chapter 8

Conclusion and Outlook

The hazard risk for fish passing an overflown weir in downstream direction is currently evaluated in Germany via the drop height and the tailwater level (DWA, 2005; LUBW, 2016). These two parameters have proven to be insufficient in the past, as the evaluation based on them does not do justice to the hydraulic complexity of the nappe and the tailwater flow (Thorenz et al., 2018) as air entrainment and turbulence at the tailwater is determined by the impact situation of the nappe (Baylar and Bagatur, 2006). It is therefore desirable to evaluate the flow situation of the nappe and in the tailwater side of overflown weirs with numerical flow simulations.

Based on observations on a prototype nappe, the hypothesis was made that upstream induced turbulence affects the characteristic of the nappe. This hypothesis was tested within this work with numerical and experimental investigations.

The development of a sharp-crested weir nappe due to upstream induced turbulence was investigated with numerical flow simulations based on the Volume-of-Fluid method (VOF). For directly computing large turbulence structures a Large Eddy Simulation (LES) model with a dynamic k equation subgrid model was used. The results of the LES simulations were compared with results from unsteady Reynolds-averaged Navier Stokes equations (URANS) models since previous numerical investigations of nappes which were based on URANS models concluded that differences in upstream turbulence have no influence on the nappe characteristics (Castillo et al., 2014). The investigations varied in turbulence intensity between

4.9 % and 17.2 % 1 m upstream of the weir and volume flow rates of 0.16 m^3/s to 0.64 m^3/s. The nappe development was evaluated visually and by the standard deviation of the time-averaged water distribution on horizontal slices of the nappe. Both evaluation methods were used for numerical and experimental investigations.

The results show that upstream turbulence intensity and in particular the large-scale turbulent structures drive the nappe development as they deform the surface of the nappe and influence the local trajectory of the nappe. For turbulent intensities of $I \geq 11.9$ % the nape undulations were strong enough to counteract the nappe thinning due to gravitational acceleration after a minima in nappe width occurred in the range 0.7 m $\lesssim Z_d \lesssim$ 1.5 m. The comparison of LES and URANS simulations which was performed in this thesis showed that the turbulence structure-driven nappe development was highly underestimated by URANS models for turbulence-rich flow situations with drop depths $Z_d \gtrsim 0.5$ m albeit the same mesh size, time step size and solver settings were used as for the LES simulations. Despite the same spatial and temporal resolution, only the largest turbulent structures are directly computed by URANS models and influence the advection equation of the VOF function. The remaining turbulent kinetic energy is transformed into subgrid turbulent kinetic energy. However, an extension of the VOF transport equation by a turbulent flux term for modeling the influence of subgrid turbulent kinetic energy on mass transport does not improve the representability of the turbulence structure-driven nappe development for URANS simulations. This emphasizes the importance of directly captured large scale turbulence structures by LES simulations for analysing the development of the nappe.

A numerical investigation of different volume flow rates, but similar turbulence intensities, showed that for higher volume flow rates the nappe widening was retarded to deeper drop depths. After the gravitational narrowing of the nappe had been overcome by the influence of turbulence, the nappe widening turned out to be more intense for higher volume flow rates. This suggested that for higher volume flow rates with higher spill heights, larger (in vertical direction) turbulence structures passed the weir crest. As a result, nappe widening became more and more independent from volume flow rate concerning the initial lateral nappe width with increasing drop depth.

The experimental investigations were carried out on a nappe of prototype scale

with a drop depth of Z_d = 9.5 m, a width of 1 m and a volume flow rate of 0.1515 m^3/s. The upstream turbulence intensity was evaluated by acoustic Doppler velocimeter (ADV) measurements. Nappe profiles at three drop depths Z_d = 0.8 m, 3.3 m, 7 m were measured with conductivity probes. These showed that the nappe fist narrowed up to Z_d = 3.3 m and then widened again. The core of the nappe with only consists of water, which still existed at Z_d = 0.8 m vanished at Z_d = 3.3 m. Visual observations showed no air bubbles inside the nappe, but the nappe fluctuations were observed to be larger than half the lateral nappe width. For drop depths deeper than 3 m, horizontal waves on the nappe surface were observed which have their origin in shear instabilities at the water-air interface.

The comparison of the experimental and the numerical upstream flow situation showed 10 times longer integral length scales for the numerical investigations which were traced back to different upstream upstream channel setups. The comparison of the nappe development showed a similar trend for drop depths up to 3.3 m. This was also supported by visual comparison of the derived nappe surface from the numerical investigations and photos taken from the experimental nappe. Both showed streaks that ran from the weir crest down to the end of the nappe of similar size and length. For deeper drop depths, the experimental nappe widening was significantly stronger than the numerical nappe widening which showed that shear instabilities at the water-air interface were decisive for nappe widening at deeper drop depth. For the investigated head water level, the begin of the shear instability was seen at a drop depth of about 3 m by showing waves at the water-air interface with wave length of about 5 cm which were not seen in the numerical model. The numerical mesh with a cell edge length of 3.125 mm at the interface was not suitable to directly compute the shear instability at the interface as at drop depths deeper than 3 m the first cell center was in the inertial sublayer of the air boundary layer ($y^+ > 50$).

A long term measurement of 10 h at the experimental setup showed strong dependency of the void fraction measurements on small model-related long-term volume flow rate fluctuations of less than 1 %. These fluctuations with period lengths of several minutes to hours distorted the nappe profile measurements by about 8 % at a drop depth of 3.3 m which was explained by the direct connection between volume flow fluctuations and nappe trajectory fluctuations. At a drop depth of 7 m,

the influence of volume flow fluctuations on the nappe width decreased to 4 % as nappe widening due to shear instabilities increased.

In general, it can be concluded that nappe widening effects due to upstream turbulence should be taken into account when designing fish descent corridors at overflown weirs with drop depth of $Z_d > 0.5$ m to ensure a realistic impact situation of the nappe and the fish at the tailwater. For drop depths of $Z_d > 3.3$ m, the numerical models tend to underestimate nappe widening due to shear instabilities at the water-air interface. However, the nappe surface area is nearly independent from volume flow rate, resulting in a decreasing influence of shear instabilities on nappe widening as volume flow rate increases.

Nappes of experimental models are influenced by long-term volume flow fluctuations which tend to overestimate the width of the nappe. Future investigations should therefore aim to evaluate nappe widening independently of these fluctuations.

Since the main risks for descending fish arise from collisions at the tailwater, the flow situation here is of particular importance. Entrained air bubbles in the tailwater change the submersion depth of fish that are buoyancy neutral to pure water, turbulence might cause disorientation of the fish and might result in a reduction in their maneuverability, increasing collision risk and risk of predation (Odeh et al., 2002). Hence, the influence of nappe widening on the immersion depth of impacting nappes and fish and on flow conditions downstream of the weir need to be considered in future investigations.

The influence of volume flow fluctuations on downstream fish migration is determined by the frequency of the fluctuations. When the fluctuation frequency is low, the tailwater has enough time to fully recover between the periods and the effected impact area which is influenced by the nappe shifts but is equal in size. At higher frequencies, however, the affected impact area is effectively increased and the momentum of the impacting nappe is distributed to the tailwater below the swept water surface. This influences air entrainment upon impact and the immersion process of the nappe (Baylar and Bagatur, 2006). Volume flow fluctuations at weirs are common e.g. due to wind-induced waves at the upstream flow situation. Hence, further investigations should examine the critical volume flow rate fluctuation frequency and the influence of upstream surface waves on the

nappe.

Weir crests at rivers are not perfectly sharp-edged, as the geometry is interrupted by vegetation or on purpose by nappe breakers which locally influence the nappe trajectory. These trajectory variations should be more stable over time compared to upstream turbulence effects. Nevertheless they should change the impact situation of the nappe at the tailwater. Therefore, the influence of local changes in the weir crest geometry on the nappe and the tailwater should be examined.

In order to enable the evaluation of fish downstream migration by numerical models, it is necessary to develop a flow solver that is able to transport fish-like particles for tracing the stresses on the fish during the weir passage. With the knowledge of fish species-specific stress limits, it would then be possible to assess the risk of injury to the fish during the passage.

With a view to future investigations, more and more computing power will be available, which means that even more computing resources can be used to compute the nappe development. However, URANS models are still an important workhorse in project work. Hence the question raises how to model the influence of subgrid turbulence on the Volume-of-Fluid function. The same applies to the widening due to shear instabilities at the water-air interface which are even underestimated by LES simulations due to limitations in mesh resolution in the area of the nappe and in simulation time.

Bibliography

Afzalimehr, H. and Bagheri, S. (2009). Discharge coefficient of sharp-crested weirs using potential flow. *Journal of Hydraulic Research*, 47(6):820–823.

Anderson, A. A. and Tullis, B. P. (2018). Finite crest length weir nappe oscillation. *Journal of Hydraulic Engineering*, 144(6):04018020.

Annemüller, H. (1958). *Luftaufnahme durch fließendes Wasser*, volume 146. Theodor-Rehbock-Flussbaulaboratorium, Techn. Hochsch.

Bagheri, S. and Heidarpour, M. (2010). Overflow characteristics of circular-crested weirs. *Journal of Hydraulic Research*, 48(4):515–520.

Baylar, A. and Bagatur, T. (2006). Experimental studies on air entrainment and oxygen content downstream of sharp–crested weirs. *Water and environment Journal*, 20(4):210–216.

Bell, M. C. and DeLacy, A. C. (1972). A compendium on the survival of fish passing through spillways and conduits.

Belzner, F., Merkel, J., Gebhardt, M., and Thorenz, C. (2017). Piano key and labyrinth weirs at german waterways: Recent and future research of the BAW. In Erpicum, S., Laugier, F., Ho Ta Khanh, M., and Pfister, M., editors, *Labyrinth and Piano Key Weirs III–PKW 2017*, pages 167–174. CRC Press.

Bercovitz, Y., Barrey, W., Lebert, F., and Buvat, C. (2018). Envelope trajectory of water jet issuing from a thin weir obtained by photogrammetry. In Bung, D. B., Tullis, B. P., Erpicum, S., and Crookston, B. M., editors, *7th International Symposium on Hydraulic Structures*.

Bercovitz, Y., Lebert, F., Jodeau, M., Buvat, C., Violeau, D., Pelaprat, L., and Hajczak, A. (2016). Ls-piv procedure applied to a plunging water jet issuing from an overflow nappe. In Erpicum, S., Dewals, B., Archambeau, P., and Pirotton, M., editors, *Proceedings of the 4th IAHR Europe Congress. Sustainable Hydraulics in the Era of Global Change*, pages 166–173, London. Taylor & Francis Group.

Blazin, H. (1890). Expériences nouvelles sur l'ecoulement en déversoir. *Annales des Ponts es Chaussées*, 60(1):9–82.

Boes, R. M. (2000). *Zweiphasenströmung und Energieumsetzung an Grosskaskaden*. ETH Zurich.

Boes, R. M. (2020). Scale effects in modelling two-phase stepped spillway flow. In Minor, H.-E. and Hager, W. H., editors, *Hydraulics of stepped spillways*, pages 53–60. [CRC Press].

Bollaert, E. (2002). The influence of plunge pool air entrainment on the presence of free air in rock joints. In Schleiss, A. and Bollaert, E., editors, *Rock scour due to falling high-velocity jets*, pages 137–149. Balkema, Lisse.

Bollaert, E. (2004). A comprehensive model to evaluate scour formation in plunge pools. *The International Journal on Hydropower & Dams*, pages 94–101.

Bollaert, E., Falvey, H. T., and Schleiss, A. (2002). Assessment of turbulent jet impingement on rocky riverbeds: The particular properties of a near-prototype physical model study. In Bousmar, D. and Zech, Y., editors, *River flow 2002*, pages 395–403. Balkema, Lisse.

Bollaert, E. and Schleiss, A. (2002). *Transient water pressures in joints and formation of rock scour due to high-velocity jet impact*. EPFL-LCH, Lausanne.

Bollaert, E. and Schleiss, A. (2005). Physically based model for evaluation of rock scour due to high-velocity jet impact. *Journal of Hydraulic Engineering*, 131(3):153–165.

Bollrich, G. (2019). *Technische Hydromechanik*. Beuth Verlag GmbH, Berlin and Wien and Zürich.

Bombardelli, F. (2020). Seeing is believing: using hybrid turbulence closures to uncover the features of flows past hydraulic structures. In IAHR, editor, *8th International Symposium on Hydraulic Structures*. The University of Queensland.

Boris, J. P. and Book, D. L. (1973). Flux-corrected transport. I. SHASTA, a fluid transport algorithm that works. *Journal of Computational Physics*, 11(1):38–69.

Brackbill, J. U., Kothe, D. B., and Zemach, C. (1992). A continuum method for modeling surface tension. *Journal of Computational Physics*, 100(2):335–354.

Brennan, D. (2001). The numerical simulation of two phase flows in settling tanks. *Dissertation, London*.

Brenner, O., Piroozmand, P., and Jenny, P. (2022). Efficient assimilation of sparse data into rans-based turbulent flow simulations using a discrete adjoint method. *Journal of Computational Physics*, 471:111667.

Bung, D. B. (2011). Developing flow in skimming flow regime on embankment stepped spillways. *Journal of Hydraulic Research*, 49(5):639–648.

Bung, D. B. (2012). Sensitivity of phase detection techniques in aerated chute flows to hydraulic design parameters. In Lehrstuhl u. Versuchsanst. für Wasserbau u. Wasserwirtschaft d. TU München, editor, *2nd European IAHR congress*, [München]. [Lehrstuhl u. Versuchsanst. für Wasserbau u. Wasserwirtschaft d. TU München].

Butterworth, S. (1930). On the theory of filter amplifiers. *Wireless Engineer*, 7(6):536–541.

Cameron, S. M., Nikora, V. I., and Stewart, M. T. (2017). Very-large-scale motions in rough-bed open-channel flow. *Journal of Fluid Mechanics*, 814:416–429.

Carrillo, J. M., Ortega, P. R., Castillo, L. G., and García, J. T. (2020a). Air entrainment in rectangular free falling jets. In IAHR, editor, *8th International Symposium on Hydraulic Structures*. The University of Queensland.

Carrillo, J. M., Ortega, P. R., Castillo, L. G., and García, J. T. (2020b). Experimental characterization of air entrainment in rectangular free falling jets. *Water*, 12(6).

Carrillo, J. M., Ortega, P. R., Castillo, L. G., and García, J. T. (2021). Air–water properties in rectangular free-falling jets. *Water*, 13(11):1593.

Cartellier, A. (1990). Optical probes for local void fraction measurements: Characterization of performance. *Review of Scientific Instruments*, 61(2):874–886.

Carvalho, R., Venturini, O. J., Tanahashi, E. I., Neves, F., and França, F. A. (2009). Application of the ultrasonic technique and high-speed filming for the study of the structure of air–water bubbly flows. *Experimental Thermal and Fluid Science*, 33(7):1065–1086.

Castillo, L. G. and Carrillo, J. M., editors (2012). *Hydrodynamics characterization in plunge pools. Simulation with CFD methodology and validation with experimental measurements*.

Castillo, L. G. and Carrillo, J. M., editors (2013). *Analysis of the scale ratio in nappe flow case by means of CFD numerical simulation*, volume 8.

Castillo, L. G. and Carrillo, J. M. (2017a). Comparison of methods to estimate the scour downstream of a ski jump. *International Journal of Multiphase Flow*, 92:171–180.

Castillo, L. G. and Carrillo, J. M. (2017b). Pressure and velocity distributions in plunge pools.

Castillo, L. G., Carrillo, J. M., and Blázquez, A. (2015). Plunge pool dynamic pressures: A temporal analysis in the nappe flow case. *Journal of Hydraulic Research*, 53(1):101–118.

Castillo, L. G., Carrillo, J. M., and Sordo-Ward, Á. (2014). Simulation of overflow nappe impingement jets. *Journal of Hydroinformatics*, 16(4):922–940.

Castro-Orgaz, O. (2008). Curvilinear flow over round-crested weirs. *Journal of Hydraulic Engineering*, 46(4):543–547.

Castro-Orgaz, O., Giráldez, J. V., and Ayuso, J. L. (2008). Critical flow over circular crested weirs. *Journal of Hydraulic Engineering*, 134(11):1661–1664.

Chakraborty, S., Keller, E., Talley, J., Srivastav, A., Ray, A., and Kim, S. (2009). Void fraction measurement in two-phase flow processes via symbolic dynamic filtering of ultrasonic signals. *Measurement Science and Technology*, 20(2):023001.

Chanson, H. (1989). Study of air entrainment and aeration devices. *Journal of Hydraulic Research*, 27(3):301–319.

Chanson, H. (1993). Velocity measurements within high velocity air-water jets. *Journal of Hydraulic Research*, 31(3):365–382.

Chanson, H. (1994). Hydraulics of nappe flow regime above stepped chutes and spillways. *TRANSACTIONS-INSTITUTION OF ENGINEERS AUSTRALIA CIVIL ENGINEERING CE*, 36:69.

Chanson, H. (1995). Predicting oxygen content downstream of weirs, spillways and waterways. *Proceedings of the Institution of Civil Engineers-Water Maritime and Energy*, 112(1):20–30.

Chanson, H. (1996). *Air bubble entrainment in free-surface turbulent shear flows*. Academic Press, San Diego.

Chanson, H. (1997). Air bubble entrainment in open channels: Flow structure and bubble size distributions. *International Journal of Multiphase Flow*, 23(1):193–203.

Chanson, H. (2009). Turbulent air–water flows in hydraulic structures: dynamic similarity and scale effects: Dynamic similarity and scale effects. *Environmental fluid mechanics*, 9(2):125–142.

Chanson, H. (2021). The Free Overfall. https://www.iahrmedialibrary.net/the-library/geophysical-hydraulics/fluvial-hydraulics/the-free-overfall/1156. [Online; accessed 23rd June 2024].

Chanson, H. and Montes, J. S. (1997). Overflow characteristics of cylindrical weirs. *Research Report No. CE154; Department of Civil Engineering, University of Queensland: Brisbane, QLD, Australia, 1997.*

Cox, R. A. and Nishikawa, T. (1991). A new total variation diminishing scheme for the solution of advective-dominant solute transport. *Water Resources Research*, 27(10):2645–2654.

Crookston, B. M., Anderson, A. A., Shearin-Feimster, L., and Tullis, B. P. (2014). Mitigation investigation of flow-induced vibrations at a rehabilitated spillway. In The University of Queensland, editor, *5th International Symposium on Hydraulic Structures*, pages 1–8. The University of Queensland.

Drazin, P. G. and Reid, W. H. (2004). *Hydrodynamic stability*. Cambridge monographs on mechanics and applied mathematics. Cambridge Univ. Press, 2 edition.

DWA (2005). *Fischschutz- und Fischabstiegsanlagen: Bemessung, Gestaltung, Funktionskontrolle*. ATV-DVWK-Regelwerk Merkblatt. DWA, Hennef.

Egorov, Y., Boucker, M., Martin, A., Pigny, S., Scheuerer, M., and Willemsen, S. (2004). Validation of cfd codes with pts-relevant test cases. *5th Euratom Framework Programme ECORA project*, pages 91–116.

Ehrenberger, R. (1926). *Wasserbewegung in steilen Rinnen (Schußtennen): Mit besonderer Berücksichtigung der Selbstbelüftung*. Hydrogr. Zentralbureau.

Ervine, D. A. and Ahmed, A. A. (1982). A scaling relationship for a two-dimensional vertical dropshaft. In BHRA Fluid Engineering, editor, *Papers presented at the International Conference on the Hydraulic Modelling of Civil Engineering Structures*. Bhra Fluid Engineering, Cranfield, Bedford, England.

Ervine, D. A. and Falvey, H. T. (1987). Behaviour of turbulent water jets in the athmosphere and in plunge pools. *Proceedings of the Institution of Civil engineers*, 83(1):295–314.

Ervine, D. A., Falvey, H. T., and Withers, W. (1997). Pressure fluctuations on plunge pool floors. *Journal of Hydraulic Research*, 35(2):257–279.

Ervine, D. A., McKeogh, E. J., and Elsawy, E. M. (1980). Effect of turbulence intensity on the rate of air entrainment by plunging water jets. *Proceedings of the Institution of Civil engineers*, 69(2):425–445.

Falvey, H. T. and Ervine, D. A. (1988). Aeration in jets and high velocity flows. In Burgi, P. H., editor, *Int. Symp. on Model-Prototype Correlation of Hydr. Structures // Model-prototype correlation of hydraulic structures*. ASCE, New York, NY.

Fan, W. and Anglart, H. (2019). Progress in phenomenological modeling of turbulence damping around a two-phase interface. *Fluids*, 4(3):136.

Felder, S. and Chanson, H. (2013). Aeration, flow instabilities, and residual energy on pooled stepped spillways of embankment dams. *Journal of irrigation and drainage engineering*, 139(10):880–887.

Florez, F., Prenner, R., and Krouzecky, N. (2016). Measurements of air concentration and velocities in a free falling water jet. *Transactions of FAMENA*, 40(1):57–68.

Fulgosi, M., Lakehal, D., Banerjee, S., and de Angelis, V. (2003). Direct numerical simulation of turbulence in a sheared air–water flow with a deformable interface. *Journal of Fluid Mechanics*, 482:319–345.

Ghobadian, R., F., C. A., Farmanifard, M., and Ahmadi, A. (2013). Effect of crest roughness on flow characteristics over circular weirs. *Civil Engineering Infrastructures Journal*, 46(2):199–207.

Goldstein, H., Poole, C. P., and Safko, J. (2002). *Classical Mechanics*. Pearson Education.

Greenshields, C. J. and Weller, H. G. (2022). *Note on computational fluid dynamics: General principles*. CFD Direct https://cfd.direct, Royaume-Uni.

Guha, A., Barron, R. M., and Balachandar, R. (2010). Numerical simulation of high-speed turbulent water jets in air. *Journal of Hydraulic Research*, 48(1):119–124.

Guyot, G., Rodriguez, M., Pfister, M., Matas, J., and Cartellier, A. (2016). Experimental study of large scale plunging jets. In Crookston, B. M. and Tullis, B. P., editors, *6th IAHR International Symposium on Hydraulic Structures // Full proceedings: hydraulic structures and water system management*. Utah State University, Logan.

Hager, W. H. (1985). Critical flow condition in open channel hydraulics. *Acta Mechanica*, 54(3):157–179.

Hager, W. H. (1987). Continuous crest profile for standard spillway. *Journal of Hydraulic Engineering*, 113(11):1453–1457.

Hager, W. H. (1995). Überfallstrahlen. *Schweizer Ingenieur und Architekt*, 113(19):442–447.

Harten, A. (1983). High resolution schemes for hyperbolic conservation laws. *Journal of Computational Physics*, 49(3):357–393.

Harvie, D. J. E., Davidson, M. R., and Rudman, M. (2006). An analysis of parasitic current generation in volume of fluid simulations. *Applied Mathematical Modelling*, 30(10):1056–1066.

Heidarpour, M. and Chamani, M. R. (2006). Velocity distribution over cylindrical weirs. *Journal of Hydraulic Research*, 44(5):708–711.

Heidarpour, M., Habili, J. M., and Haghiabi, A. H. (2008). Application of potential flow to circular-crested weir. *Journal of Hydraulic Research*, 46(5):699–702.

Heller, V. (2011). Scale effects in physical hydraulic engineering models. *Journal of Hydraulic Research*, 49(3):293–306.

Herringe, R. A. (1973). *A study of the structure of gas-liquid mixture flows*. University of NSW.

Hirt, C. W. (2003). Modeling entrainment of air at turbulent free surfaces. *Flow Science, Inc*, pages 1–10.

Hirt, C. W. and Nichols, B. D. (1981). Volume of fluid (vof) method for the dynamics of free boundaries. *Journal of Computational Physics*, 39(1):201–225.

Horeni, P. (1956). Disintegration of a free jet of water in air. *Byzkumny ustav vodohospodarsky prace a studie, Sesit*, 93.

Hoyt, J. W. and Taylor, J. J. (1975). Mechanism of air entrainment in a high-speed water jet. In *Symposium on two-phase flow and cavitation in power generation systems gas in liquid flows*, pages 329–335. Grenoble.

Hoyt, J. W. and Taylor, J. J. (1977a). Turbulence structure in a water jet discharging in air. *The Physics of Fluids*, 20(10):S253.

Hoyt, J. W. and Taylor, J. J. (1977b). Waves on water jets. *Journal of Fluid Mechanics*, 83(1):119–127.

Jeong, J. and Hussain, F. (1995). On the identification of a vortex. *Journal of Fluid Mechanics*, 285:69–94.

Killen, J. M. and Anderson, A. G. (1969). A study of the air-water interface in air-entrained flow in open channels. In *13th Congress of the International Association for Hydraulic Research*. International Association for Hydraulik Research.

Kim, W.-W. and Menon, S. (1995). A new dynamic one-equation subgrid-scale model for large eddy simulations. In *33rd Aerospace Sciences Meeting and Exhibit*. American Institute of Aeronautics and Astronautics.

Kitsikoudis, V., Lodomez, M., Dewals, B., Archambeau, P., Pirotton, M., and Erpicum, S. (2021). Occurrence and characteristic frequencies of nappe oscillations at free-overfall structures. *Journal of Hydraulic Engineering*.

Kobus, H. (1985). *An introduction to air-water flows in hydraulics*, volume 61 of *Mitteilungen / Institut für Wasserbau, Universität Stuttgart*. Inst. für Wasserbau Univ, Stuttgart.

Kolmogorov, A. N. (1991). The local structure of turbulence in incompressible viscous fluid for very large reynolds numbers. *Proceedings of the Royal Society of London. Series A - Mathematical and Physical Sciences*, 434(1890):9–13.

Kramer, K. (2004). *Development of aerated chute flow*. ETH Zurich.

Lakshmana Rao, N. S., Kobus, H., and Barczewski, B., editors (1975). *Characteristics of self-aerated free-surface flows*, volume 10 of *Water and waste water current research and practice*. Schmidt, Berlin.

Lamb, O. P. and Killen, J. M. (1950). An electrical method for measuring air concentration in flowing air-water mixtures. *St. Anthony Falls Hydraulic Laboratory*.

Leu, M.-C., Meng, P., Geskin, E. S., and Tismeneskiy, L. (1998). Mathematical modeling and experimental verification of stationary waterjet cleaning process. *Journal of Manufacturing Science and Engineering*, 120(3):571–579.

Lodomez, M. (2016). Nappe vibration mitigation techniques for free-overfall structures. In Crookston, B. M. and Tullis, B. P., editors, *6th IAHR International Symposium on Hydraulic Structures // Full proceedings: hydraulic structures and water system management*, pages 359–366. Utah State University, Logan.

Lodomez, M., Crookston, B. M., Tullis, B. P., and Erpicum, S. (2019). Mitigation techniques for nappe oscillations on free-overfall structures. *Journal of Hydraulic Engineering*, 145(2).

Lodomez, M., Pirotton, M., Dewals, B., Archambeau, P., and Erpicum, S. (2018). Nappe oscillations on free-overfall structures: Experimental analysis: Experimental analysis. *Journal of Hydraulic Engineering*, 144(3):04018001.

Lopes, P. M. B. (2017). *Free-surface flow interface and air-entrainment modelling in hydraulic structures*. PhD thesis, Universidade de Coimbra.

LUBW (2016). *Handreichung Fischschutz und Fischabstieg an Wasserkraftanlagen: Fachliche Grundlagen*. LUBW Landesanstalt für Umwelt, Messungen und Naturschutz Baden-Württemberg, Karlsruhe.

Ma, G., Shi, F., and Kirby, J. T. (2011a). A polydisperse two-fluid model for surf zone bubble simulation. *Journal of Geophysical Research*, 116(C5).

Ma, J., Oberai, A. A., Drew, D. A., Lahey, R. T., and Hyman, M. C. (2011b). A comprehensive sub-grid air entrainment model for rans modeling of free-surface bubbly flows. *The Journal of Computational Multiphase Flows*, 3(1):41–56.

Ma, J., Oberai, A. A., Hyman, M. C., Drew, D. A., and Lahey, R. T. (2011c). Two-fluid modeling of bubbly flows around surface ships using a phenomenological subgrid air entrainment model. *Computers & Fluids*, 52:50–57.

Ma, Y.-P., Chung, N.-M., Pei, B.-S., Lin, W.-K., and Hsu, Y.-Y. (1991). Two simplified methods to determine void fractions for two-phase flow. *Nuclear Technology*, 94(1):124–133.

Matysiak, A. (2007). Euler-lagrange verfahren zur simulation tropfenbeladener strömung in einem verdichtergitter. *Doctoral dissertation, Universitätsbibliothek der HSU/UniBwH*.

Maulik, R., Sharma, H., Patel, S., Lusch, B., and Jennings, E. (2021). A turbulent eddy-viscosity surrogate modeling framework for reynolds-averaged navier-stokes simulations. *Computers & Fluids*, 227:104777.

Menter, F. R. and Esch, T. (2002). Elements of industrial heat transfer predictions. In Steffen Jr, V., editor, *16th Brazilian Congress of Mechanical Engineering: Symposium on Vibration and Acoustics*. Hindawi Publishing Corporation.

Menter, F. R., Kuntz, M., and Langtry, R. (2003). Ten years of industrial experience with the sst turbulence model. In Hanjalić, K., Nagano, Y., and Tummers, M. J., editors, *Turbulence, heat and mass transfer 4*, volume 4, pages 625–632. Begell House, New York, NY.

Mokos, A., Violeau, D., Sarret, F., De Leffe, M., and Bercovitz, Y. (2022). Sph modelling of the water nappe gravity fall over a dam. *Journal of Hydraulic Research*, 60(4):606–618.

Moraga, F. J., Carrica, P. M., Drew, D. A., and Lahey, R. T. (2008). A sub-grid air entrainment model for breaking bow waves and naval surface ships. *Computers & Fluids*, 37(3):281–298.

Muñoz-Cobo, J. L., Chiva, S., Méndez, S., Monrós, G., Escrivá, A., and Cuadros, J. L. (2017). Development of conductivity sensors for multi-phase flow local measurements at the polytechnic university of valencia (upv) and university jaume i of castellon (uji). *Sensors*, 17(5).

Muralha, A., Melo, J. F., and Ramos, H. M. (2020). Assessment of cfd solvers and turbulent models for water free jets in spillways. *Fluids*, 5(3).

Nakagawa, H., Nezu, I., and Ueda, H. (1975). Turbulence of open channel flow over smooth and rough beds. In Japan Society of Civil Engineers, editor, *Proceedings of the Japan Society of Civil Engineers*, volume 1975, pages 155–168. Japan Society of Civil Engineers.

Odeh, M., Noreika, J. F., Haro, A., Maynard, A., Castro-Santos, T., and Cada, G. F. (2002). Evaluation of the effects of turbulence on the behavior of migratory fish. *Final Report to the Bonneville Power Administration, Contract*, 22.

Odeh, M. and Orvis, C. (1998). Downstream fish passage design considerations and developments at hydroelectric projects in the northeast usa. In Jungwirth, M., Schmutz, S., and Weiss, S., editors, *Fish Migration and Fish Bypasses*, pages 267–280. Fishing News Books, Oxford, UK.

Okuda, K. (1982). Internal flow structure of short wind waves: Part i. on the internal vorticity structure. *Journal of the Oceanographical Society of Japan*, 38:28–42.

Osher, S. and Sethian, J. A. (1988). Fronts propagating with curvature-dependent speed: Algorithms based on hamilton-jacobi formulations. *Journal of computational physics*, 79(1):12–49.

Pfister, M. (2007). *Schussrinnenbelüfter: Lufttransport ausgelöst durch interne Abflussstruktur*. PhD thesis, ETH Zurich.

Pfister, M. and Chanson, H. (2012). Scale effects in physical hydraulic engineering models by valentin heller, journal of hydraulic research, vol. 49, no. 3 (2011), pp. 293–306. *Journal of Hydraulic Research*, 50(2):244–246.

Pfister, M. and Chanson, H. (2014). Two-phase air-water flows: Scale effects in physical modeling. *Journal of Hydrodynamics*, 26(2):291–298.

Pfister, M. and Hager, W. H. (2010). Chute aerators. i: Air transport characteristics. *Journal of Hydraulic Engineering*, pages 352–359.

Pope, S. B. (2000). *Turbulent flows*. Cambridge Univ. Press, Cambridge.

Rajaratnam, N. and Muralidhar, D. (1971). Pressure and velocity distribution for sharp-crested weirs. *Journal of Hydraulic Research*, 9(2):241–248.

Ramamurthy, A. S. and Vo, N. D. (1993). Characteristics of circular-crested weir. *Journal of hydraulic engineering*, 119(9):1055–1062.

Rhie, C. M. and Chow, W. L. (1983). Numerical study of the turbulent flow past an airfoil with trailing edge separation. *AIAA journal*, 21(11):1525–1532.

Rodi, W. (2017). Turbulence modeling and simulation in hydraulics: A historical review. *Journal of Hydraulic Engineering*, 143(5).

Rusche, H. (2002). *Computational fluid dynamics of dispersed two-phase flows at high phase fractions*. Imperial College London (University of London), London.

Saric, W. S. (1994). Görtler vortices. *Annual Review of Fluid Mechanics*, 26(1):379–409.

Schulze, L. (2018). *Development of an application-oriented approach for two-phase modelling in hydraulic engineering: Dissertation*, volume Heft 61 of *Dresdner wasserbauliche Mitteilungen*. Dresden.

Scimemi, E. (1937). Il profilo delle dighe sfioranti. *L'energia Elettrica*, 14:937–940.

Sene, K. J. (1988). Air entrainment by plunging jets. *Chemical Engineering Science*, 43(10):2615–2623.

Shaikh, N. and Siddiqui, K. (2008). Airside velocity measurements over the wind-sheared water surface using particle image velocimetry. *Ocean dynamics*, 58:65–79.

Shirinzad, A., Kumahor, S., Sagharichi, A., and Tachie, M. F. (2023). Experimental investigation of turbulent flow over a sharp-crested circular cylindrical segment. *Physical Review Fluids*, 8(7).

Sokoray-Varga, B. (2022). *Inspection, post-processing and error filtering of captured velocity time series*. Karlsruhe.

Song, X., Yu, Z., Liu, C., and Cheng, G. (2022). Calibration of rans model constant based on data assimilation and accurate simulation of separated flow. *AIP Advances*, 12(9):095324.

SonTek (2001). Sontek/ysi advfield/hydra acoustic doppler velocimeter (field) technical documentation.

Taylor, G. I. (1938). The spectrum of turbulence. *Proceedings of the Royal Society of London. Series A - Mathematical and Physical Sciences*, 164(919):476–490.

Thorenz, C., Gebhardt, M., and Weichert, R. (2018). Numerical study on the hydraulic conditions for species migrating downstream over a weir. In Bung, D. B. and Tullis, B., editors, *7th International Symposium on Hydraulic Structures*. Utah State University, Logan, Utah.

Thorenz, C. and Grefenstein, A. (2022). Numerical modeling of air bubble transport behind a model scale weir. In IAHR, editor, *Proceedings of the 39th IAHR World Congress*. IAHR document library.

Thorwarth, J. (2009). *Hydraulisches Verhalten von Treppengerinnen mit eingetieften Stufen: Selbstinduzierte Abflussinstationaritäten und Energiedissipation*, volume 156 of *Mitteilungen des Lehrstuhls und Instituts für Wasserbau und Wasserwirtschaft der Rheinisch-Westfälischen Technischen Hochschule Aachen*. Shaker, Aachen.

Toombes, L. and Chanson, H. (2007). Free-surface aeration and momentum exchange at a bottom outlet. *Journal of Hydraulic Research*, 45(1):100–110.

Tsang, C. (1987). *Hydraulic and aeration performance of labyrinth weirs*. University of London.

Valero, D. and García-Bartual, R. (2016). Calibration of an air entrainment model for cfd spillway applications. In Gourbesville, P., editor, *Advances in Hydroinformatics*, Springer Water Ser, pages 571–582. Springer Singapore Pte. Limited, Singapore.

van Leer, B. (1974). Towards the ultimate conservative difference scheme. ii. monotonicity and conservation combined in a second-order scheme. *Journal of Computational Physics*, 14(4):361–370.

Velasco, D. W. and Huhta, C. A. (2010). Experimental verification of acoustic doppler velocimeter (adv) performance in fine-grained, high sediment concentration fluids. *App Note SonTek/YSI*, pages 1–19.

Volkart, P. (1980). The mechanism of air bubble entrainment in self-aerated flow. *International Journal of Multiphase Flow*, 6(5):411–423.

Watanabe, Y., Saeki, H., and Hosking, R. J. (2005). Three-dimensional vortex structures under breaking waves. *Journal of Fluid Mechanics*, 545:291–328.

White, F. M. (1991). *Viscous fluid flow*. McGraw-Hill series in mechanical engineering. McGraw-Hill, Boston, Mass., 2. ed. edition.

Wilhelms, S. C. (1997). *Self-aerated Spillway Flow*. University of Minnesota.

Wüthrich, D., Shi, R., and Chanson, H. (2022). Ensemble-statistical approach in the measurement of air-water flow properties in highly unsteady breaking bores. *Review of Scientific Instruments*, 93(5):054502.

Xavier Meriade Duarte, R. (2014). *Influence of Air Entrainment on Rock Scour Development and Block Stability in Plunge Pools*. Lausanne, EPFL.

Yan, K. and Che, D. (2018). A coupled model for simulation of the gas–liquid two-phase flow with complex flow patterns. *International Journal of Multiphase Flow*, 36(4):333–348.